INFORMATION TO USERS

This manuscript has been reproduced from the microfilm master. UMI films the text directly from the original or copy submitted. Thus, some thesis and dissertation copies are in typewriter face, while others may be from any type of computer printer.

The quality of this reproduction is dependent upon the quality of the copy submitted. Broken or indistinct print, colored or poor quality illustrations and photographs, print bleedthrough, substandard margins, and improper alignment can adversely affect reproduction.

In the unlikely event that the author did not send UMI a complete manuscript and there are missing pages, these will be noted. Also, if unauthorized copyright material had to be removed, a note will indicate the deletion.

Oversize materials (e.g., maps, drawings, charts) are reproduced by sectioning the original, beginning at the upper left-hand corner and continuing from left to right in equal sections with small overlaps. Each original is also photographed in one exposure and is included in reduced form at the back of the book.

Photographs included in the original manuscript have been reproduced xerographically in this copy. Higher quality 6" x 9" black and white photographic prints are available for any photographs or illustrations appearing in this copy for an additional charge. Contact UMI directly to order.

UMI

A Bell & Howell Information Company
300 North Zeeb Road, Ann Arbor MI 48106-1346 USA
313/761-4700 800/521-0600

UNIVERSITY OF ALBERTA

INTERFACIAL REACTIONS IN THIN FILM AND BULK IRON/SILICON DIFFUSION COUPLES

By

YUHONG ZHANG

A thesis submitted to the Faculty of Graduate Studies and Research in partial fulfillment of the requirements for the degree of MASTER OF SCIENCE

In

MATERIALS ENGINEERING

DEPARTMENT OF CHEMICAL AND MATERIALS ENGINEERING

EDMONTON, ALBERTA

FALL 1997

National Library of Canada

Bibliothèque nationale du Canada

Acquisitions and Bibliographic Services

Acquisitions et services bibliographiques

395 Wellington Street
Ottawa ON K1A 0N4
Canada

395, rue Wellington
Ottawa ON K1A 0N4
Canada

Your file Votre référence

Our file Notre référence

The author has granted a non-exclusive licence allowing the National Library of Canada to reproduce, loan, distribute or sell copies of this thesis in microform, paper or electronic formats.

L'auteur a accordé une licence non exclusive permettant à la Bibliothèque nationale du Canada de reproduire, prêter, distribuer ou vendre des copies de cette thèse sous la forme de microfiche/film, de reproduction sur papier ou sur format électronique.

The author retains ownership of the copyright in this thesis. Neither the thesis nor substantial extracts from it may be printed or otherwise reproduced without the author's permission.

L'auteur conserve la propriété du droit d'auteur qui protège cette thèse. Ni la thèse ni des extraits substantiels de celle-ci ne doivent être imprimés ou autrement reproduits sans son autorisation.

0-612-22696-4

Canadä

UNIVERSITY OF ALBERTA

RELEASE FORM

NAME OF AUTHOR: **YUHONG ZHANG**

TITLE OF THESIS: **Interfacial Reactions in Thin Film and Bulk Iron/Silicon Diffusion Couples**

DEGREE: **Master of Science**

YEAR THIS DEGREE GRANTED: **1997**

Permission is hereby granted to the University of Alberta Library to reproduce single copies of this thesis and to lend or sell such copies for private, scholarly or scientific research purposes only.

The author reserves all other publication and other rights in association with the copyright in the thesis, and except as hereiunbefore provided neither the thesis nor any substantial portion thereof may be printed or otherwise reproduced in any material form whatever without the author's prior written permission.

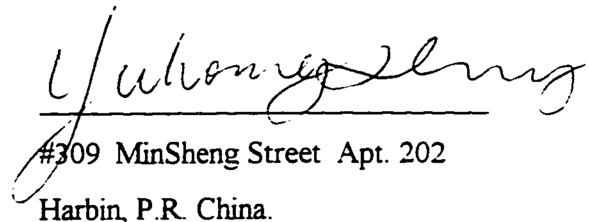

#309 MinSheng Street Apt. 202
Harbin, P.R. China.

DATE: July. 17. 1997

UNIVERSITY OF ALBERTA

FACULTY OF GRADUATE STUDIES AND RESEARCH

The undersigned certify that they have read, and recommend to the Faculty of Graduate Studies and Research for acceptance, a thesis entitled **INTERFACIAL REACTIONS IN THIN FILM AND BULK IRON/SILICON DIFFUSION COUPLES** submitted by **YUHONG ZHANG** in partial fulfillment of the requirements for the degree of **MASTER OF SCIENCE** in **MATERIALS ENGINEERING.**

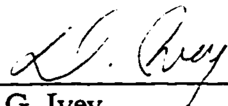

Dr. D. G. Ivey
Supervisor

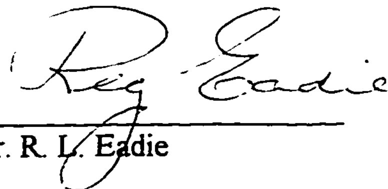

Dr. R. L. Eadie

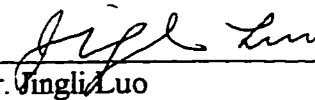

Dr. Jingli Luo

Dr. S. Dew

DATE: July 10/97

ABSTRACT

Iron silicide formation, by thermal reaction of Fe-Si thin film and bulk diffusion couples, has been systematically studied. The bulk diffusion couple work involved the construction and annealing of diffusion couples made from pieces of pure Fe and single crystal Si. Annealing was done at 600, 637, 666 and 700°C for times ranging from 7 to 1653 hours. Iron silicides in bulk couples were characterized by scanning electron microscopy (SEM) with energy dispersive spectroscopy (EDS). Studies were focused on the couples annealed at 700°C, especially on Fe_3Si layers. Only stoichiometric Fe_3Si existed in the bulk diffusion couples. The results were explained in terms of thermodynamics and kinetics. The Fe silicide growth sequence was observed in bulk diffusion couples. Fe_3Si formed first, followed by FeSi and then $FeSi_2$. Fe was determined as the major diffuser in Fe_3Si. Silicide growth was diffusion controlled.

In thin film diffusion couple work, silicides were characterized by transmission electron microscopy (TEM) with EDS. An oxide layer and off-stoichiometric Fe_3Si were found in as-deposited samples. Off-stoichiomtric Fe_3Si formed below 100°C. Upon annealing, off-stoichiometric Fe_3Si transformed to stoichiometric Fe_3Si. Initial iron silicide formation was explained by a kinetic model. A semiquantitative reaction process plot for the Fe-Si diffusion system was calculated. FeSi growth at 500°C and β-$FeSi_2$ growth at 700°C were diffusion controlled.

In order to better understand Fe_3Si formation and growth, four alloys were made with compositions of 11at%, 15at%, 22at% and 25 at% Si. Electron diffraction was used to distinguish between off-stoichiometric Fe_3Si and stoichiometric Fe_3Si. Diffusion couples were fabricated with Si and stoichiometric Fe_3Si. Off-stochiometric Fe_3Si formed in the diffusion zone, but Fe diffused much more slowly in off-stoichiometric Fe_3Si than in stochiometric Fe_3Si.

ACKNOWLEDGMENTS

I am deeply grateful to Dr. Douglas G. Ivey for his supervision, guidance, and encouragement extended throughout the course for this study.

I am greatly appreciative to the Alberta Microelectronic Center (AMC) for Fe deposition. I am also grateful to the Natural Sciences and Engineering Research Council of Canada for financial assistance.

I would like to acknowledge Dr. R.F. Egerton, Dr. M.H. Chen who provided access to TEMs. I would like to thank Ms. Tina Baker and Mr. Shiraz Merali and Mr. Bob Konzuk for their help in obtained supplies.

Table of Contents

Chapter 1. Introduction 1

Chapter 2. Literature Survey 4

2.1 Structure and Properties of Iron Silicides 4

2.1.1. Fe_3Si 4

2.1.2. ε-FeSi 4

2.1.3. FeSi (CsCl) 5

2.1.4. α- $FeSi_2$ 5

2.1.5. β-$FeSi_2$ 5

2.1.6. γ-$FeSi_2$ 5

2.2. The Order-Disorder Phase Transformation 6

2.3. The Magnetic Moments of the Two Types of Fe Atoms in Fe_3Si and Site Preference of Transition Metal Solutions in Fe_3Si 11

2.3.1. The Dependence of Fe Moments on Fe Neighbours 11

2.3.2. Selective Site Substitution of Transition Metal Impurities in The Fe_3Si Matrix 12

2.4. Fe Diffusion Behavior in α-Fe-Si Alloys 13

2.4.1. Atomistic Determination of Diffusion Mechanism in the Fe_3Si Lattice 13

2.4.2. Fe Diffusion in α-Fe-Si Alloys 13

2.4.3. Binding States in Fe_3Si 13

2.5. Thin Film Fe Silicide Formation 14

2.5.1. Current Technique For Growing Silicide Epilayers 14

2.5.1.1. Metallic Silicides and Semiconducting Silicide Epilayers 15

2.5.1.2. Specific Properties of β-$FeSi_2$ 15

2.5.1.3. Current Techniques for silicide Hereroepitaxy 16

2.5.2. Epitaxial Phase Transitions in the Fe/Si System 17

2.5.2.1. Interfacial Reactions of Fe Thin Films on Si substrates 17

2.5.2.1.1. Fe/Si Room Temperature Interface Reactions...17
2.5.2.1.2. Fe/Si Interface Annealing Behavior............18
2.5.2.2. β-$FeSi_2$ Heteroepitaxy on Si............19
2.5.2.2.1. Heteroepitaxy on Si (100)............19
2.5.2.2.2. Heteroepitaxy on Si (111)............19
2.5.2.2.3. Strained Metastable Cubic $FeSi_2$ Heteroepitaxy on Si (111)............19
2.5.3. Growth Kinetics of Iron Silicides Fabricated by SPE............20
2.5.4. The Effect of Oxygen on the Formation of Iron Silicides............20
2.6. A Comparison Between Bulk and Thin Film Phase Formation............21

Chapter 3. Bulk Diffusion Couples............37
3.1. Experimental Methods............37
3.1.1. Fabrication of Fe/Si Alloys............37
3.1.2. Fabrication of Bulk Diffusion Couples............37
3.1.3. Annealing............38
3.1.4. Sample Preparation............38
3.1.4.1. TEM Sample Preparation............38
3.1.4.2. SEM Sample Preparation............39
3.1.4.2.1. Bulk Couples............39
3.1.4.2.2. Fe-Si Alloy............39
3.2. Characterization............40
3.2.1. Alloy Phase Identification............40
3.2.2. Bulk Diffusion Couple Characterization............41
3.3. Results and Discussion............41
3.3.1. Fe/Si Alloy Composition Analysis, Microstructure and Lattice Parameter Calculation............41
3.3.1.1. Fe/Si Alloy Composition Analysis............41
3.3.1.2. Fe_3Si Electron Diffraction............42
3.3.1.3. Fe_3Si Lattice Parameter and Fe/Si Alloy Microstructures 42

3.3.2. Fe/Si Bulk Diffusion Couples........42
3.3.2.1. Phases and Compositions........43
3.3.2.2. Fe_3Si in Fe/Si Couples........43
3.3.2.3. Growth Kinetics of Fe_3Si, β-$FeSi_2$ and FeSi........44
3.3.2.4. Major Diffuser in Fe_3Si and FeSi........44
3.3.2.5. Fe/Fe-Si alloy Diffusion Couples........45
3.3.2.6. Fe_3Si Formation in Bulk Diffusion Couples........45
3.3.2.6.1. Fe_3Si Free Energy........45
3.3.2.6.2. Atomic Diffusion Mechanism in Fe_3Si Lattice...46
3.3.2.7. Silicide Growth at 700°C in Bulk Diffusion Couples........47
3.4. Conclusions........48

Chapter 4. Thin Film Diffusion Couples........79
4.1. Experimental Methods........79
4.1.1. Deposition of Iron........79
4.1.2. Annealing........79
4.1.3. TEM Sample Preparation........79
4.1.4. Characterization........81
4.2. Results and Discussion........81
4.2.1. Interfacial Oxide and Interfacial Reactions at Room Temperature..81
4.2.2. Annealing Reactions at Low Temperatures........82
4.2.3. Growth Process of β-$FeSi_2$ at High Temperatures........83
4.3. Formation Sequence of Iron Silicides........84
4.3.1. The Assumptions........85
4.3.2. Explanation for the Iron Silicides Formation Sequence........85
4.4. Conclusions........86

Chapter 5. Comparison of Thin Film and Bulk Couple Results........107

Chapter 6. Conclusions and Recommendations 109

References 110

List of Tables

Table 2-1 Fe_3Si neighbor configurations ... 26
Table 2-2 Binding energy computations ... 26
Table 2-3 Structural data for semiconducting silicides ... 27
Table 2-4 Experimental and theoretical energy gaps for semiconducting silicides at room temperature ... 28
Table 3-1 Compositions of alloys ... 49
Table 3-2 Atom positions for stoichiometric Fe_3Si ... 49
Table 3-3 Atoms positions in order off stoichiometric Fe_3Si ... 50
Table 3-4 Atoms positions in random off stoichiometric Fe_3Si ... 51
Table 3-5 Structure Factor of Fe_3Si ... 52
Table 3-6 Allowed reflections for Fe_3Si based on Structure Factor calculations ... 52
Table 3-7 D-spacing of alloys and Fe_3Si ... 53
Table 3-8 Bulk diffusion couples produced ... 53
Table 3-9 Phases observed in bulk diffusion couples ... 54
Table 3-10 Order parameter and free energy with respect to composition ... 55
Table 4-1 Annealing conditions studied with TEM at low temperatures ... 88
Table 4-2 Annealing conditions studied with TEM at high temperatures ... 88

List of Figures

Figure 2-1 Fe-Si Phase Diagram 29

Figure 2-2 Stoichiometric Fe_3Si DO_3 structure 30

Figure 2-3 Off-stoichiometric Fe_3Si B2 structure 31

Figure 2-4 Fe [A,C] and Fe [B] d DOS functions 32

Figure 2-5 Fe-Si (1.87-19.2at% Si). ^{59}Fe diffusion coefficients vs. reciprocal temperature for various Si concentrations (in at%) 33

Figure 2-6 Schematic diagram of concentration profile of A atoms in the simultaneous growth of two layer compounds $A_\beta B$ and $A_\gamma B$ between A and B 34

Figure 2-7 Schematic summary of Gösele and Tu's analysis of growth kinetics 35

Figure 2-8 Schematic reation process plot for silicide formation in thin metal film-Si diffusion couples 36

Figure 3-1 Diagram of steel claming plate for bulk diffusion couples 55

Figure 3-2 SEM micrographs of Alloy B and Alloy C 56

Figure 3-3a XRD spectrum of alloy A 57

Figure 3-3b XRD spectrum of alloy B 58

Figure 3-3c XRD spectrum of alloy C 59

Figure 3-4 Fe_3Si lattice parameter vs. Fe concentration 60

Figure 3-5a TEM micrograph of a plan view and SAD pattern from alloy A 61

Figure 3-5b TEM micrograph of a plan view and SAD pattern from alloy B 62

Figure 3-5c TEM micrograph of a plan view and SAD pattern from alloy C 63

Figure 3-6 SEM backscattered electron image of interface of an Fe/Si diffusion couple 64

Figure 3-7a SEM backscattered electron image of an Fe-Si couple, annealed at 700°C for the shortest time studied (7 hrs) 65

Figure 3-7b A composition profile corresponding to the image in Fig.3-6a 66

Figure 3-8a SEM backscattered electron image of an Fe-Si couple, annealed at 700°C for 1007 hrs 67

Figure 3-8b A composition profile corresponding to the image in Fig.3-7a.............68
Figure 3-9 A composition profile for high magnification image of the Fe_3Si/Fe interface in an Fe/Si couple.............69
Figure 3-10 The thickness of Fe_3Si layer in bulk couples is plotted as a function of annealing time.............70
Figure 3-11 The first stage of FeSi growth observed in the bulk couple annealed at 700°C for 23 hrs.............71
Figure 3-12 Thickness vs. time plot for FeSi in bulk couples.............72
Figure 3-13 The thickness of β–$FeSi_2$ layer in bulk couples is plotted as a function of annealing time.............73
Figure 3-14 Si concentration in α-Fe of a diffusion couple annealed at 700°C for 23 hrs.............74
Figure 3-15a SEM image of an Fe/alloy D diffusion couple annealed at 700°C for 120 hrs.............75
Figure 3-15b A composition profile corresponding to the image in Fig.3-15a.............76
Figure 3-16 Free energy of Fe_3Si vs. Si concentration at 700°C.............77
Figure 3-16 Schematic silicide sequence growth in bulk diffusion couples at 700°C.............78
Figure 4-1 Construction of cross-sectional TEM samples.............89
Figure 4-2a As-deposition Fe film on Si (111) shown in cross-section.............90
Figure 4-2b As-deposited Fe film on Si (111) shown in in plan view.............90
Figure 4-2c SAD pattern corresponding to Fig.4-2b.............90
Figure 4-3a Oxide layer and Fe_3Si layer in as-deposition Fe film on Si (111) shown in plan view.............91
Figure 4-3b SAD pattern corresponding to Fig.4-3a.............91
Figure 4-3c EDX spectrum from oxide layer.............91
Figure 4-4a TEM micrograph of a cross section from thin film sample annealed at 300°C for 3hrs.............92
Figure 4-4b SAD pattern from Fe and Fe_3Si layers at the thin film sample annealed at 300°C for 3 hrs.............92

Figure 4-4c SAD pattern from Fe_3Si and FeSi layers at the thin film sample annealed at 300°C for 3 hrs 92

Figure 4-5 SAD pattern from Fe_3Si and FeSi layers at the thin film sample annealed at 400°C for 1 hr 93

Figure 4-6 TEM micrograph of a cross section from the thin film sample annealed at 500°C for 10 sec 94

Figure 4-6a TEM micrograph of a cross section from the thin film sample annealed at 500°C for 3 min 95

Figure 4-7b TEM micrograph of a plan view from FeSi and Fe_3Si layers in the sample annealed at 500°C for 3 min 96

Figure 4-7c SAD pattern corresponding to Fig.4-6b 96

Figure 4-8 TEM micrograph of a cross section from the thin film sample annealed at 500°C for 2.5 hrs 97

Figure 4-9 Thickness of FeSi as a function of time in thin films at 500°C 98

Figure 4-10 TEM micrograph of a cross section from the thin film sample annealed at 600°C for 15 min 99

Figure 4-11 TEM micrograph of a cross section from the thin film sample annealed at 600°C for 2hrs 100

Figure 4-12 TEM micrograph of a plan view from the thin film sample annnealed at 600°C for 75 min 101

Figure 4-13 β-$FeSi_2$ in the thin film sample annealed at 700°C for 2 min 102

Figure 4-14 β-$FeSi_2$ thickness in the thin films as a function of time at 700°C 103

Figure 4-15 Schematic model for Fe-Si silicide formation 104

Figure 4-16 Semiquantitative reaction process plots for Fe-Si thin films 105

Figure 4-17 Summery silicide formation in Fe-Si thin films 106

ABBREVIATIONS

SEM	Scanning electron microscopy
EDS	Energy dispersive spectroscopy
TEM	Transmission electron microscopy
RT	Room temperature
UPS	Ultraviolet photoelectron spectroscopy
XPS	X-ray photoelectron spectroscopy
REEED	Real time reflection high-energy electron diffraction
AES	Auger electron spectroscopy
EELS	Electron energy loss spectroscopy
RBS	Rutherford backscattering spectroscopy
XRD	X-ray diffraction
LEEDS	Low-energy electron diffraction spectroscopy
CEMS	Conversion electron Mossbauer specctroscopy
BWG	Bragg-William-Grosky model

Chapter 1 Introduction

Silicon based microprocessors associated with optoelectronic devices play an important role in information technology, which is recognized as one of the most important scientific disciplines currently and in the future. There is great interest in the controlled formation of expitaxial silicides on silicon because of their potential application in the production of silicon integrated circuits [1] and also as a subject for fundamental research. $FeSi_2$, as one of the most promising silicides, has attracted much attention in the recent past. $FeSi_2$ exists as two phases, the tetragonal metallic α-$FeSi_2$, stable above about 950°C, and the low temperature orthorhombic semiconducting β-$FeSi_2$ phase [2]. Semiconducting β-$FeSi_2$ is of particular technological interest, because optical [3,4] and electron spectroscopic measurements [5] have indicated the existence of a direct bandgap of about 0.85 eV. Thus semiconducting β-$FeSi_2$ may be a suitable material for infrared optoelectronic devices fabricated on silicon. Applications of β-$FeSi_2$ in microelectronics are also conceivable, e.g., as a narrow bandgap base layer of a heterobipolar transistor.

A number of thin film studies have been done on the Fe-Si system. Most research has focused on β- $FeSi_2$. In an attempt to improve the surface morphology and crystalline quality of β- $FeSi_2$ grown epitaxially on Si, the interest has shifted to characterizing the Fe/Si interface and the first silicide formed during annealing. In addition to basic issues, according to Fe/Si interfacial reactions, the quantity of silicon consumed can be determined and the electrical properties can be predicted [6].

Other silicides, Fe_3Si and FeSi, which are thermodynamically stable at low temperatures ($\leq$ 800°C), also can be obtained during annealing of Fe/Si thin films. Fe_3Si, according to the phase diagram, has a wide range of stoichiometry, i.e., 10-25 at% Si. Fe_3Si has a cubic structure consisting of 4 interpenetrating fcc sublattices [7].

Stoichiometric Fe_3Si ($Fe_{75}Si_{25}$) has a DO_3 structure. For Si compositions between 10 and 25at%, off-stoichiometric Fe_3Si has two structures, α_1 and α_2. α_1 has a DO_3-related structure [8]; α_2 has a B2 structure.

FeSi shows a homogeneity region extending from about 49.0-50.8 at% Si at 1150°C [7]. The crystal structure is a cubic, B20-type. Recently FeSi with a CsCl-type structure was discovered by Känel [9]. This metallic phase only forms during annealing of very thin Fe films. It can transform to $FeSi_2$ with no change in symmetry by continuous annealing [10].

Results reported up to now in the literature for the early stages of reaction at Fe/Si interface at room temperature (RT) are somewhat contradictory. Results obtained from a photoemission study indicated that FeSi formation first occurred during deposition of 0.4 nm of Fe [11]. A β-$FeSi_2$ - like phase, which formed first at very low coverages (0.1-0.3nm) was identified in [6,13] using ultraviolet photoelectron spectroscopy (UPS), x-ray photoelectron spectroscopy (XPS) and real time reflection high-energy electron diffraction (RHEED). Fe_3Si formed first upon deposition of Fe above 1ML thickness, as reported by [14, 15] using XPS.

Fe/Si interface annealing behavior has been investigated by several researchers [17-26]. The common result is that β-$FeSi_2$ formed above 600°C and FeSi, Fe_3Si formed below 500°C. A major controversy centres on the first phase to form at the Fe/Si interface. FeSi was the first phase followed by Fe_3Si in a number of studies [16-19, 22-25]; these include TEM [16], Auger electron spectroscopy (AES) and electron energy loss spectroscopy (EELS) [17,18], Rutherford backscattering spectroscopy (RBS) and x-ray diffraction (XRD) [20,25] and XPS [24] work. Fe_3Si occurred first in [15, 19, 23, 26], based on RBS and XRD [15], AES [19, 23], low-energy electron diffraction spectroscopy (LEEDS) [19], XPS [23], UPS [23] and conversion electron Mossbauer spectroscopy (CEMS) work. Growth kinetics of iron silicides, particularly Fe_3Si, has not been clear. Very little has been done.

The purpose of the present work is to investigate initial reactions at the Fe/Si interface. Both thin films and bulk couples are studied for comparison purposes. TEM, SEM, EDS and XRD are utilized as the primary characterization tools for phase analysis. Relatively thick Fe layers (~ 165 nm) are utilized for the thin film work in order to prevent the sequential growth often observed in thin film silicide reactions.

This thesis is organized in six chapters. A comprehensive literature review is provided in Chapter 2, which consists of bulk diffusion couple and thin film parts. A brief summary of the structure and properties of iron silicides, the order-disorder phase transformation and Fe diffusion behavior in the Fe_3Si lattice are discussed in the bulk couple part. A comprehensive survey of published experimental results on Fe/Si thin film interface behavior is presented in the thin film part. Chapter 3 describes the experimental procedures used for fabricating Fe/Si system bulk couples, and the techniques used for phase characterization in the bulk couples. The results and conclusions of the bulk couple work are also discussed in this chapter. Chapter 4 describes the experimental methods and results for the thin film work. A comparison of the thin film and bulk couple work is discussed in Chapter 5. Conclusions and Recommendations are in given Chapter 6.

Chapter 2. Literature Review

2.1. *Structure and Properties of Iron Silicides*

2.1.1. *Fe_3Si*

Fe_3Si, according to the phase diagram (Fig.2-1 [7]), has a wide range of stoichiometry, i.e., 10-25at%Si. Fe_3Si has a cubic superstructure consisting of 4 interpenetrating fcc sublattices, labeled A, B, C and D, with origins at the points (0, 0, 0), (1/4, 1/4, 1/4), (1/2, 1/2, 1/2) and (3/4, 3/4, 3/4), arranged regularly along the body diagonal (Fig.2-2 [27]). Each A atom is at the center of a cube with 4B and 4D atoms at corners in a tetrahedral arrangement. Similarly, each B atom is at the center of a cube with 4A and 4C atoms at corners in cubic arrangements.

In stoichiometric Fe_3Si, Fe atoms occupy the A, C and B sites. Thus, the Fe atoms on equivalent (both structurally and magnetically) A and C sites have tetrahedral point symmetry with 4Fe [B] and 4Si [D] atoms as nearest neighbors, as in elemental bcc Fe [8].

For Si compositions between 10 and 25at%, off-stoichiometric Fe_3Si has two structures, α_1 and α_2. α_1 has a DO_3-related structure. Fe [A,C] sites can have either 5 Fe and 3 Si atoms as nearest neighbors or 6 Fe and 2 Si atoms as nearest neighbors [28]. α_2 has a B2 structure, which is shown in Fig.2-3 [29].

Alloys of the DO_3 type are of interest for 2 reasons [30]. Firstly, the DO_3 structure is a superstructure of the B2 (CsCl)-type lattice, which is essentially a superstructure of the A2 (bcc)-type lattice. For this reason, DO_3 alloys are a good example for studying the influence of superstructure formation on properties.

Secondly, Fe-Si alloys with a bcc structure, including the superstructures, are of technical importance as soft magnetic materials. There exist detailed measurements of magnetic, electrical, and other properties as a function of composition and ordering state. These dependencies are continuous in a striking manner so that they may be described by analytical terms [30].

2.1.2. *ε-FeSi*

The monosilicide, ε-FeSi, is commonly referred to as simply FeSi. FeSi melts congruently at 1410°C and shows a homogeneity region extending from about 49.0 - 50.8

at% Si at 1150°C [7]. The crystal structure of ε-FeSi is cubic, B20-type. The Pearson symbol is cP8 and the space group is $P2_13$ [31].

2.1.3. FeSi (CsCl)

FeSi with a CsCl-type structure was discovered recently by Kãnel [9]. This metallic phase only forms during annealing of very thin Fe films. It can transform to $FeSi_2$ with no change in symmetry by continuous annealing [10].

2.1.4. α-FeSi₂

α-$FeSi_2$ is a stable phase above 937°C. It is metallic with a tetragonal structure. The composition deviates from the stoichiometric composition through the formation of up to 13% Fe vacancies [7].

2.1.5. β-FeSi₂

β-$FeSi_2$ has an orthorhombic structure with lattice parameters of a = 0.986nm, b = 0.779 nm and c = 0.783nm and is stable below 950°C [10]. β-$FeSi_2$ is stoichiometric and at higher temperatures transforms to the metallic α-$FeSi_2$ phase.

Orthorhombic $FeSi_2$ has a deformed CaF_2 structure. The CaF_2 structure is similar to the diamond cubic Si structure. The lattice mismatch between β-$FeSi_2$ and Si is small, so that the growth of epitaxial layers on Si is possible.

β-$FeSi_2$ is semiconducting. Forbidden energy-gap values for β-$FeSi_2$ have been measured and were found to be between 0.7 and 1.0 eV [2, 4, 32-38]. Experimental optical absorption measurements [32-37] indicate the existence of a direct band gap. Recently, optical transmittance measurements of polycrystalline $FeSi_2$ in the range of 0.8-1.0 eV at low temperatures (≤80K) indicated the existence of an indirect gap a few tens of meV lower than the direct transition [40]. According to reference [40], the contribution of defect levels prevents the determination of the indirect gap value at higher temperatures. Bost and Mahan [33] have recently corrected their previously published band gap values. They have proposed that β-$FeSi_2$ exhibits two direct transitions, one at 1.01eV and the other one, corresponding to the forbidden energy gap, at 0.89 eV. These values are near the absorption minimum of silica optical fibers. This coupled with its band gap, makes β-$FeSi_2$ promising for optoelectronic devices integrated in the silicon process.

2.1.6. γ-FeSi₂

Metastable and metallic γ-$FeSi_2$ was indexed several years ago [41, 42]. This phase can be grown on a Si (111) substrate by deposition of very thin Fe films (several

monlayers thick. The strain induced by the substrate stabilizes this cubic structure up to a critical temperature, which is dependent on the film thickness [41]. The lattice symmetry of γ-$FeSi_2$ is fcc and its crystal structure is very close to the fluorite one [43].

The high density of states at the Fermi level makes metallic γ-$FeSi_2$ metastable and the total energy can be minimized by distortion to semiconducting β-$FeSi_2$ [44].

2.2. The Order-Disorder Phase Transformation

Recent elastic neutron-scattering experiments [45, 46] have led to a revision of the iron-rich part of the iron-silicon phase diagram shown in Fig.2-1, which is based on Kubaschewski's [1] survey of the literature on extrapolations by Buchener [47]. There are four regions: single-phase α, single phase α_2, two phase $\alpha_1 + \alpha_2$, and single-phase α_1. The crystal structures are: α-A2, α_1-DO_3 and α_2-B2; all three are variations on the bcc structure. A2 is the standard disordered or short-range ordered bcc structure, whereas DO_3 and B2 are long-range ordered. A unified description of all three structures is obtained by the introduction of a large cubic elementary cell with a lattice constant a. For c equal to 0.095, a is 0.5708nm at ambient temperature [48]. (c is the atomic fraction of Si). a is close to twice the lattice constant of pure α-Fe. This large cell is considered to consist of four penetrating standard fcc elementary cells, which will be called A, B, C, and D. The occupation of these four sublattices by Si atoms is as follows [49]:

disordered A2: Si atoms occupy sites on all four sublattices with the same probability.

fully ordered B2: for $c \leq 0.15$, Si atoms occupy only sites on the B and D sublattices.

fully ordered DO_3: for $c \leq 0.25$, Si atoms occupy only sites on the D sublattice.

The A2/B2 and B2/DO_3 transitions take place in the bcc solid solution. The atomic configurations in bcc Fe-Si solid solutions are mainly determined by the strong affinity which exists between neighboring Fe and Si atoms [50, 51]. Inden [52] extended the Bragg-Williams-Gorsky model (BWG) and gave the most stable atomic configuration in a binary bcc solid solution with respect to temperature and alloy composition, taking into account nearest (n.n.) and next nearest neighbor (n.n.n.) interactions. The main simplification of the model is to describe the atomic distributions as being random inside certain suitable sublattices. The choice of three sublattices follows from the kind of interaction between the atoms. Since in the Fe-Si system, n.n- and n.n.n-interactions have

to be considered, the bcc lattice (with lattice constant a) is divided into four fcc lattices (a = $2a_o$). The atoms inside (A + B) are nearest neighbour with respect to the atoms inside (C + D) and vice versa. The atoms inside A or C are second nearest neighbors with respect to atoms inside B or D, respectively, and vice versa (see Fig.2-2).

Any atomic configuration can be described with the aid of three suitable and independent parameters [9]. These parameters, x, y, z, are defined by the occupation probabilities p_{Fe}^{L} of Fe in the four sublattices L = A, B, C and D [52]:

$$x = \frac{1}{4}(p_{Fe}^{A} + p_{Fe}^{B} - p_{Fe}^{D} - p_{Fe}^{D})$$
$$y = \frac{1}{2}(p_{Fe}^{C} - p_{Fe}^{D})$$
$$z = \frac{1}{2}(p_{Fe}^{A} - p_{Fe}^{B}) \qquad (2\text{-}1)$$

An equal distribution of the atoms onto the four sublattices (structure A2) is described by x = y = z = 0. The state x ≠ 0, y = z = 0 indicates a preferential Fe-occupation in A and B (x > 0) or in C and D (x < 0) sites. Consequently, the Si-atoms preferentially occupy the sublattices C and D or A and B, respectively. Since inside each sublattice the distribution of atoms is treated as random, it follows that the number of Fe-Si neighbors in n.n. configurations is increased (structure B2) compared with the configuration A2. From an equivalent consideration, it follows that y ≠ 0 or z ≠ 0 describes a surplus of Fe-Si neighbors in n.n.n sites (structure DO_3) compared with the configuration B2.

The above considerations can be formulated more quantitatively by calculating the numbers of different atom pairs in n.n. and n.n.n. sites from the number N of lattice sites and the atom fraction C_{Fe} and C_{Si} of Fe and Si, respectively [52].

$$(Fe,Si)_{n.n} = 4N(C_{Fe}C_{Si} + x^2)$$
$$(Si,Fe)_{n.n} = 4N(C_{Fe}C_{Si} + x^2)$$
$$(Fe,Fe)_{n.n} = 4N(C_{Fe}^2 - x^2) \qquad (2\text{-}2)$$
$$(Si,Si)_{n.n} = 4N(C_{Si}^2 - x^2)$$

and

$$(Fe,Si)_{n.n.n} = 3N(C_{Fe}C_{Si} - x^2 + \frac{1}{2}(y^2 + z^2))$$

$$(Si,Fe)_{n.n.n.} = 3N(C_{Fe}C_{Si} - x^2 + \frac{1}{2}(y^2 + z^2))$$

$$(Fe,Fe)_{n.n.n.} = 3N(C_{Fe}^2 + x^2 - \frac{1}{2}(y^2 + z^2)) \tag{2-3}$$

$$(Si,Si)_{n.n.n.} = 3N(C_{Si}^2 + x^2 - \frac{1}{2}(y^2 + z^2))$$

It is sufficient to consider the ordering reactions for x, y, z ≥ 0. The limits for these depend upon the composition of the alloy:

$$\begin{aligned} &0 \le x \le C_{Si}, \quad \text{for } 0 \le C_{Si} \le 0.5 \\ &0 \le y \le \min(C_{Fe} - x, C_{Si} + x) \\ &0 \le z \le \min(C_{Fe} + x, C_{Si} - x) \end{aligned} \tag{2-4}$$

The largest value of these parameters corresponds to the highest degree of order.

Considering chemical interaction, the configurational free energy F_k can be expressed as [52]:

$$F_k = U_k - TS_k \tag{2-5}$$

The internal energy is given as:

$$U_k = U_k^o + \frac{N}{2}\{(8W - 6w)x^2 + 3w(y^2 + z^2)\} + NC_{Fe}C_{Si}(4W + 3w) \tag{2-6}$$

where:

$$U_k^o = N\{4(C_{Fe}C_{FeFe} + C_{Si}V_{SiSi}) + 3(C_{Fe}v_{FeFe} + C_{Si}v_{SiSi})\} \tag{2-7}$$

The entropy is as follows:

$$\begin{aligned} S_k = -k\frac{N}{4}\{&(C_{Fe} + x + z)\ln(C_{Fe} + x + z) + (C_{Si} - x - z)\ln(C_{Si} - x - z) + \\ &(C_{Fe} + x - z)\ln(C_{Fe} + x - z) + (C_{Si} - x + z)\ln(C_{Si} - x + z) + \\ &(C_{Fe} - x + y)\ln(C_{Fe} - x + y) + (C_{Si} + x - y)\ln(C_{Si} + x - y) + \\ &(C_{Fe} - x - y)\ln(C_{Fe} - x - y) + (C_{Si} + x + y)\ln(C_{Si} + x + y) \end{aligned} \tag{2-8}$$

The parameters W and w are the interchange energies of the process 2 FeSi ⇔ FeFe + SiSi for n.n. and n.n.n., and V and v are bond energies for n.n. and n.n.n., respectively. The energies are deduced from the nearest and second nearest neighbor bond

energies [54], namely $W = -2V_{FeSi} + V_{FeFe} + V_{SiSi}$ and $w = -2v_{FeSi} + v_{FeFe} + v_{SiSi}$. Positive values for W, w correspond to greater affinity between unlike than between like atoms.

Necessary equilibrium conditions require that:

$$\frac{\partial F_k}{\partial x} = kT\ln\{\frac{(C_{Fe}+x+z)(C_{Fe}+x-z)(C_{Si}+x-y)(C_{Si}+x+y)}{(C_{Fe}-x+y)(C_{Fe}-x-y)(C_{Si}-x+z)(C_{Si}-x-z)}\} - 8(4W-3w)x = 0$$

$$\frac{\partial F_k}{\partial y} = kT\ln\{\frac{(C_{Fe}-x+y)(C_{Si}+x+y)}{(C_{Fe}-x-y)(C_{Si}+x-y)}\} - 12wy = 0$$

$$\frac{\partial F_k}{\partial z} = kT\ln\{\frac{(C_{Fe}+x+z+)(C_{Si}-x+z)}{(C_{Fe}+x-z)(C_{Si}-x-z)}\} - 12wz = 0 \qquad (2\text{-}9)$$

Sufficient equilibrium conditions require the following for all principal minors of the functional matrix:

$\frac{\partial^2 F_k}{\partial \varepsilon \partial \tau}$ are positive, where ε, τ = x, y, z are positive. (2-10)

The critical temperatures T_x and T_y depend upon the interchange energies and the alloy composition. Specifically [52]:

a) At high temperatures, $x_{min} = y_{min} = z_{min} = 0$, which corresponds to the A2-configuration.

b) For the case where $W > 1.5w \geq 0$, which is fulfilled in Fe-Si solid solutions, there exists a critical temperature.

$$T_x = \frac{(8W-6w)}{K} \cdot C_{Fe} \cdot C_{Si} \qquad (2\text{-}11)$$

Below this temperature, $x_{min} \neq 0$; $y_{min} = z_{min} = 0$, which means that the ordering reaction in n.n. sites is predicted. This leads to B2-configurations.

c) At still lower temperatures there exists a second critical temperature.

$$T_y = \frac{6W}{k}\{C_{Fe} - x_{min}(T_y)\} \cdot \{C_{Si} + x_{min}(T_y)\} \qquad (2\text{-}12)$$

Below this temperature the minimum in F_k is at $x_{min} \neq 0$; $y_{min} = z_{min} = 0$, which means that ordering reactions in n.n.n. sites are also predicted. This leads to DO_3-type configurations. The solutions, $x_{min} \neq 0$; and $x_{min} = y_{min} = z_{min} = 0$, predict B2- and A2-configurations at $T_y < T < T_x$ and $T > T_x$ respectively.

d) Under the condition $W > 1.5w \geq 0$, it follows from the model that there exists no further critical temperature T_z below T_y. This means that no n.n.n. ordering reactions between the sublattices A and B are predicted under the above condition.

In addition to the chemical interactions in Fe_3Si, Inden [55] considered magnetic interactions in the same (BWG) approximation to correct the free energy. The approximation accounts for their mutual influences: e.g., the critical temperatures may depend on both kinds of interchange energies and on the degree of long-range order. The magnetic interactions are treated in a similar way to chemical interactions by pair-wise defined energy parameters. These parameters are taken to be zero for Si-Si and Fe-Si pairs, since Si atoms do not bear a magnetic moment (spin). The iron atoms are treated only as having either spin up or down independent of the atomic environment and without regard to the actual value of the iron moments. There are only the two different nearest neighbor bond energies, $V_{Fe\downarrow Fe\downarrow}$ and $V_{Fe\uparrow Fe\downarrow}$ for Fe-Fe pairs with parallel and antiparallel spins, respectively; further magnetic Fe-Fe bonding in next nearest neighbor positions is neglected [56, 57, 58, 59].

The occupation probabilities of an iron atom with spin up or down in one of four sublattices L = A, B, C and D is then

$$p^L_{Fe\uparrow} = p^L_{Fe} \cdot q \text{ or } p^L_{Fe\downarrow} = p^L_{Fe} \cdot (1-q) \qquad (2\text{-}13)$$

respectively. $p^L_{Fe} = p^L_{Fe\uparrow} + p^L_{Fe\downarrow}$ is similar to p^L_{Si}, i.e., the probability of having the component Fe (like Si) in sublattice L, whereas q is the probability of the iron atom having its spin up. This probability is assumed to be independent of the particular sublattice. The paramagnetic state is then given by q = (1-q) = 0.5; hence q varies as $0.5 \leq q \leq 1$. The number of different atom pairs in the nearest neighbor (n.n.) and in the next nearest neighbors (n.n.n.) sites are given by

$$(X,Y)_{n.n} = a_{xy}N\{(p^A_x + p^B_x)(p^C_y + p^D_y) + (p^C_x + p^D_y)(p^A_y + p^B_y)\}$$

$$(X,Y)_{n.n.n} = a_{xy}\frac{3N}{2}\{p^A_x p^B_y + p^B_x p^A_y + p^C_x p^D_y + p^D_x p^C_y\} \qquad (2\text{-}14)$$

N is the number of all lattice sites, $a_{XY} = 1$ for $X \neq Y$, $a_{XY} = 0.5$ for $X = Y$ and $X, Y = Si, Fe\uparrow, Fe\downarrow$. These pair-numbers are expressed with respect to the magnetic order parameter q in Eq. (2-13) and with respect to the chemical order parameters x, y, z (Eq. (2-1)).

$$p^L_{Si} = 1 - p^L_{Fe}(L = A,B,C,D)$$

$C_{Fe} = (1 - C_{Si})$ is the atomic concentration of Fe. (2-15)

The internal energy can be written as:

$$U_k = U_k^o - N\{4[W + J(2q-1)^2]x^2 - 3wx^2 + \frac{3}{2}w(y^2 + z^2)\}$$
$$-NC_{Fe}C_{Si}\{4[W + J(2q-1)^2] + 3w\} + 4NC_{Fe}J(2q-1)^2 \quad (2\text{-}16)$$

with

$$U_k^o = N\{4(C_{Fe}V_{FeFe} + C_{Si}V_{SiSi}) + 3(C_{Fe}v_{FeFe} + C_{Si}v_{SiSi})\} \quad (2\text{-}7)$$

J is the magnetic parameter and it can be deduced from the Fe-Fe bond energy [55].

The entropy can be written as:

$$S_k = S_k^c + S_k^q \quad (2\text{-}17)$$

The chemical part is given as:

$$S_k^c = -k\frac{N}{4}\sum\{p_{Fe}^L \ln p_{Fe}^L + p_{Si}^L \ln p_k^L\} \quad (2\text{-}18)$$

and the magnetic part of the configurational entropy is:

$$S_k^q = -kNC_{Fe}\{q \ln q + (1-q)\ln(1-q)\} \quad (2\text{-}19)$$

k is the Boltzman constant.

The configurational free energy $F_k = U_k - TS_k$ is therefore obtained from Eq. (2-16) (2-17) (2-18) (2-19) as a function of temperature T, composition C_{Fe}, chemical order parameters x, y, z, the magnetic order parameter q and the energy parameters W, w, J, V and v. The most stable configuration in an undecomposed solid solution at fixed C_{Fe} and T is defined by a set of data for the order parameters x, y, z and q. This set has to be calculated from F_k by the standard procedures using the necessary and the sufficient equilibrium conditions [60].

2.3. *The Magnetic Moments of the Two Types of Fe Atoms in Fe_3Si and Site Preference of Transition Metal Solutions in Fe_3Si*

2.3.1. *The Dependence of Fe Moments on Fe Neighbors*

The specific neighbor configurations for Fe_3Si are summarized in Table 2-1 [61].

The Fe atoms are located in two different sites, which are A, C and B (see Fig.2-2), which are chemically and magnetically inequivalent. Fe [A,C] sites have an

environment of tetrahedral symmetry with 4 Fe and 4 Si nearest neighbors. Fe [B] has an environment of cubic symmetry with 8 Fe nearest neighbors. Polarized-neutron experiments [62, 63], as well as saturation magnetization measurements [64], have established that the magnetic moments of the two types of Fe atoms are very different.

The B-site moment in Fe_3Si (mFe[B] $\approx$ (2.2-2.4)μ_B, where μ_B is the Bohr magneton) is close to the moment of elemental bcc Fe, while the moment on the A and C sites (mFe[A,C] $\approx$ (1.1 -1.35)μ_B), is significantly smaller.

It should be pointed out that $Fe_{3+y}Si_{1-y}$ forms a continuous range of solid solutions with a bcc structure between c = 0 and 0.25 [7]. For low concentrations, Si substitution has little effect on the magnetic moment of neighboring Fe atoms, the average magnetization being close to that of a simple solution. Between 10 and 25at% Si, the ordered DO_3 type superlattice forms, in which Si shows a preference for sites with no Si in the first two neighboring shells, and specific first n.n. configurations become essential for the magnetic behavior of the Fe atoms.

2.3.2. Selective Site Substitution of Transition Metal Impurities In The Fe_3Si Matrix

A unique property of the Fe_3Si matrix is that transition metal impurities selectively substitute for Fe in one of the two inequivalent sites, as shown in NMR studies [65] and confirmed by neutron diffraction [66] and Mössbauer results [67]. The site occupied depends on the position of the impurities in the Periodic Table. The elements to the left of Fe, for example Mn and V, show strong preference for the Fe [B] sites, while those to the right of Fe, such as Co and Ni, select the [A,C] sites [68].

Kurdnovsky [27] provided insight into the site preference for substitutional transition-metal impurities in Fe_3Si using the sublattice density-of-states (DOS) function. The Fe [A,C] and Fe [B] d DOS functions are shown in Fig.(2-4) [27]. The Fe [A,C] sites have three main peaks. When an iron atom is replaced by a transition element with fewer d electrons than Fe, it is energetically more favorable to fill the low-lying DOS peak of the "bcc" d DOS than to fill states in the low-lying and the middle peaks of the Fe [A,C] DOS. Consequently, such impurities will prefer to enter the B sites. On the other hand, a transition metal with more s electrons than Fe prefers to replace [A,C] Fe atoms, because the energy associated with the filling of the two lowest peaks of the Fe [A,C] d DOS is lower than that of a structure where the high-lying second peak of the Fe [B] DOS becomes (partially) filled.

2.4. *Fe Diffusion Behavior in a-Fe-Si Alloys*

2.4.1. *Atomistic Determination of Diffusion Mechanism in The Fe_3Si Lattice*

Wever and Frohberg [69] and Baker and Westerveld [70] have proposed that during diffusion in DO_3 lattices, the dominant species, i.e., the iron atoms in this case, jump between the three iron sublattices only, i.e., the A and C sublattices and the B sublattice. This model is called the A-B model. More recently, Sepiol [71] studied the atomistic jump mechanism in Fe_3Si using Mosssbauer spectroscopy. The results obtained imply that for stoichiometric Fe_3Si,. the dominating mechanism is jumps via vacancies on the three Fe sublattices. For off-stoichiometric alloys, a strong contribution comes from diffusion via antistructure sites (Fe on the D sublattice).

2.4.2. *Fe Diffusivity in a-Fe-Si Alloys*

Fitzer had already shown in 1953 [72] that the diffusion coefficient of Fe increases with increasing silicon concentration in the solid solution, and that on achieving the maximum Si concentration in α-Fe-Si, it is about 20 times higher than pure Fe. Sepiol also reported that the diffusivity of iron atoms in stoichiometric Fe_3Si is extraordinarily high (e.g., at 720°C, the diffusivity is a factor of 5 to 10 lower for the off-stoichiometric $Fe_{80}Si_{20}$ compared with stoichiometric Fe_3Si [71]) and decreases strongly when leaving stoichiometry towards the iron rich side. Million [74] measured diffusion coefficients of Fe in Fe-Si single crystals for the 5.5-19.2at% Si concentration range and these are shown in Fig.(2-5) [73].

2.4.3. *Binding States in Fe_3Si*

The affinity between neighboring Fe- and Si-atoms in bcc Fe-Si solid solutions has been analyzed by Mossbauer spectroscopy [50, 52]. It was found that the Si atoms shared their (3s)- and (3p)- electrons with their Fe neighbors, thus filling up the (3d)-states of these Fe-atoms.

In the two-center approximation, the hopping integrals are given in terms of ten simpler parameters such as ssσ, spσ, etc, listed in Table 2-2 [61]. The single-site energies that enter the matrix are E_{Si}^{s}, E_{Si}^{p} and $E_{Fe}^{d\sigma} = E_{Fe}^{d} + \sigma\Delta$. $\sigma = \pm 1$ for up and down spin electrons, respectively, and Δ is the Stroner exchange-splitter parameter. s, p, d are atomic orbitals; σ, π, δ refer to the components of angular momentum around the axis. The

affinity between neighboring Fe and Si atoms can be deduced from a linear combination the single-site energies and the atomic orbital interaction energies. According to Table 2-2, the affinity between neighboring Fe and Si atoms is stronger than between neighboring Fe and Fe atoms.

2.5. *Thin Film Fe Silicide Formation*

2.5.1. *Current Techniques For Growing Silicide Epilayers*

2.5.1.1. *Metallic Silicides and Semiconducting Silicide Epilayers*

Research on epitaxial silicides began more than a decade ago. A large number of transition-metal silicides were found to epitaxially grow on silicon [75-79]. Mainly due to a large misfit and different crystallographic structure relative to the silicon substrate, these silicides form small epitaxial grains (a few hundreds of nm) leaving large areas of bare Si substrate between them. Uniform lateral epitaxy seems rather difficult to achieve. By far most attention has been paid to $NiSi_2$ and $CoSi_2$. $NiSi_2$ and $CoSi_2$ both have a cubic CaF_2 structure and can produce satisfactory epitaxial films, the misfit with respect to Si being -0.4% and -1.2% respectively, and can produce satisfactory epitaxial films. These silicides have potential for use in high-speed-devices, such as metallic base transistors and permeable base transistors. Rare-earth-metal silicides, such as $YSi_{1.7}$ and $ErSi_{1.7}$ [80, 81], have been discovered to grow with high uniformity on silicon. A very interesting tunable internal photoemission sensor has been built recently based on a $PtSi/ErSi_{1.7}$ heterostructure [82].

Semiconducting silicides have been claimed to be promising new materials for integrated optoeletronic device applications. Only a few silicides are reported to be semiconducting. These include Si-rich phases with transition metals from Groups VI and VII in the Periodic Table. Up to now, nine semiconducting silicides have been reported [83]: $CrSi_2$, $MnSi_{1.7}$, β-$FeSi_2$, Ru_2Si_3, $ReSi_2$, OsSi, Os_2Si_3, $OsSi_2$ and Ir_3Si_5. Their crystallographic structures and electronic structures are listed in Table 2-3 and Table 2-4. Their advantages include a range of applicable band gaps, good prospects for epitaxial growth and an expected compatibility with silicon processing techniques [76, 87, 100]. There are at least two main reasons to investigate semiconducting silicide epilayers. Firstly, their respective optical gaps are expected to match nicely with some important infrared emission and detection windows. For instance, iron disilicide in its semiconducting phase (β-$FeSi_2$) and rhenium silicide (ReSi) display optical gaps close to ~ 0.84eV and

0.12eV (~1.47 and ~10.33 μm respectively). Secondly, silicide crystallographic alignment with the silicon substrate can be quite good.

2.5.1.2. Specific Properties of β-$FeSi_2$

Unlike closely related transition metal silicides like $CoSi_2$ and $NiSi_2$, β-$FeSi_2$, the compound in equilibrium with silicon at low temperatures (T<940°C), is not metallic with a cubic structure but a semiconductor with an orthorhombic structure. β-$FeSi_2$ cannot easily be compared to the common semiconductors (e.q., Si, Ge and GaAs,) as its electronic structure is not based on sp^3 hybridization but on a solid state Jahn-Teller effect [100]. This effect is simultaneously the cause of a lattice distortion and a band gap opening at the Fermi level, as compared with the metallic state of the fluorite structure of $CoSi_2$ and $NiSi_2$. Recently, a detailed theoretical study of $FeSi_2$ has shown that if a fluorite $FeSi_2$ phase exists, it should be metallic with its Fermi level pinned in a large peak of non-bonding d states of iron in the $FeSi_2$ electronic density of states [121]. This would lead to an electronic instability in the fluorite metallic $FeSi_2$ structure. Therefore, the system lowers its energy by undergoing a lattice distortion to relax toward the more stable orthorhombic and semiconducting β-$FeSi_2$.

The electronic structure of β-$FeSi_2$ has been studied theoretically [101-104, 121]. Band structure calculations have revealed its semiconducting character, i.e., the minimum in the density of states at E_F opens into a gap. On both sides of the gap the states exhibit dominantly d character. The calculations suggest a strong coupling of band edge states to the lattice. A direct transition at about 0.85 eV and an indirect transition at about 0.79 eV have been obtained [104].

Numerous optical studies have been performed on the interband edges in order to reveal gap values and gap nature. In all cases, this information has been derived from conventional square or square root plots of absorption coefficient versus photon energy. A pronounced absorption tail exists in β-$FeSi_2$. The band tail states have been approximated by an Urbach exponential edge with a dominant contribution of structural disorder [105]. Defect densities of 10^{19} cm^{-3} were determined from optical absorption studies [106]. Thin films of β-$FeSi_2$ exhibit poor electrical characteristics, mainly represented by low carrier mobility (on the order of 1 cm^2/Vs) and high carrier concentration (within the range of 10^{18} - 10^{19} cm^{-3}). The low carrier mobility in β-$FeSi_2$ was predicted by Christiansen [121] and was attributed to particularly strong electron-phonon scattering effects. Recently, Tassis et al [104] found that different growth techniques and thermal processes may

influence the electron-phonon interaction. A Hall mobility of 97cm^2/Vs and a hole concentration of 1×10^{17} cm^{-3} have been obtained for polycrystalline β-$FeSi_2$.

The high optical absorption (α (hν) > 10^5 cm^{-1}) for hν > 0.8 eV is a precondition in photovaltaic applications for β-$FeSi_2$. Photoresponse for epitaxial β-$FeSi_2$ films has been measured [107]. The internal quantum yield has a low-energy edge at 0.7 eV, which correlates with the energy of a non-direct transition [99], and the maximum is reached at the direct transition energy of 0.85 eV. The strong influence of the Fe/Si ratio during layer growth on recombination gives hope for further improvement of the quantum yield of $FeSi_2$/Si heterostructures.

The optimum efficiency of a thermoelectric device depends solely on the dimensional figure of merit ZT and temperatures of the hot and cold ends. β-$FeSi_2$ is currently under development for use in automobiles, as a source of emergency power [108]. Sintered $FeSi_2$ has been investigated as a thermoelectric material, since its Seebeck coefficient is very large and its electrical resistivity is low. Co-doped single crystal β-$FeSi_2$ has a Seebeck coefficient of 0.5mV/K up to 600 K, which is about 2 times higher than presently obtained with sintered material.

2.5.1.3. Current Techniques for Silicide Heteroepitaxy

The most widely used routes to grow epitaxial silicides on silicon are solid phase epitaxy (SPE), reactive deposition epitaxy (RDE), molecular beam epitaxy (MBE) and ion implanation techniques. In SPE, the transition metal film is first deposited on a silicon substrate maintained at room temperature. During subsequent annealing at higher temperature (~600°C), intermixing finally leads to the formation of the compound in equilibrium with silicon (β–$FeSi_2$ for the Fe/Si system).

In RDE, a flux of transition metal atoms is delivered to a hot silicon surface. The intermixing takes place easily, because atomic diffusion is well activated. In both SPE and RDE growth techniques, a common feature is that all the silicon atoms used to form the epitaxal silicide film are extracted from the silicon substrate. The intermixing and epitaxial growth are then controlled by thermodynamics, which determines the compound in equilibrium with the silicon substrate, and by atomic diffusion which determines, together with nucleation processes, the kinetics of the phase formation.

Simultaneous deposition of both species from atomic beams in MBE techniques is highly desirable to circumvent effects due to long range diffusion of atoms. MBE has been used only in a few cases for the growth of silicides [116]. A reason for that may be the limited control of the chemical composition during deposition compared to the narrow

domain of stoichiometry of disilicides. Precisely controlled codeposition of both species is a major challenge for the growth of high quality silicide films in MBE compared with the SPE and RDE techniques.

Recently, several groups have achieved the growth of epitaxial β-$FeSi_2$ layers, buried in Si substrates, with iron implantation [109-114]. Ion bombardment speeds silicide reactions in two ways. First, either through direct injection or by Ar^+ mixing, the ion beams create a mixed layer of Fe-Si. This has the advantage of not requring long range diffusion of large amounts of material. The second way that iron beams can speed the formation of silicides is through the energy they inject in the form of local defects and disorder. Defects sites and local disorder can provide the energy necessary for silicides to nucleate, especially β-$FeSi_2$, which is known to be hampered in its kinetics by a large activation energy of nucleation.

2.5.2. Epitaxial Phase Transitions in The Fe/Si System

2.5.2.1. Interfacial Reactions of Fe Thin Films on Si Substrates

In an attempt to improve the surface morphology and crystalline quality of β-$FeSi_2$ grown epitaxially on Si, interest has shifted to characterizing the Fe/Si interface and the first silicide that forms during annealing under ultrahigh-vacuum (UHV) conditions. In addition to basic issues, there are two main reasons for obtaining this information. Firstly, only with this information can the quantity of silicon consumed in the reaction be determined. The second reason is to allow prediction of the electrical characteristics of silicide/silicon contacts.

2.5.2.1.1. Fe/Si Room Temperature Interface Reaction

Results reported up to now in the literature for the early stages of reaction at the Fe/Si interface at room temperature (RT) are somewhat contradictory. Results obtained from a photoemission study indicated that FeSi formation occurred during the deposition of 0.4 nm of Fe [11]. With increasing Fe coverage, the silicide changed to an Fe-rich silicide, followed by pure Fe [11]. From their inverse photoemission investigation, De Crescenzi et al [12] concluded that a β-$FeSi_2$ -like phase formed at very low coverages (0.1−0.2 nm), followed by the growth of a metallic Fe film in the form of clusters or discontinuous islands, at increasing coverages. Li et al [114] proposed, based on an ultraviolet photoelectron spectroscopy (UPS) and x-ray photoelectron spectroscopy

(XPS) study, the formation of an intermixed $FeSi_2$-like phase in the initial stage (~0.1nm) for Fe on Si (111) and the presence of a composition gradient to Fe metal for increasing coverages. The diffusion of Si atoms was limited as the Fe coverage increased. At very high Fe coverages, a pure Fe overlayer appears. Gallego et al [6] found that the Fe/Si (100) interface was reactive at room temperature. Upon deposition of Fe above 1ML, a spontaneous reaction occurred which resulted in the formation of an amorphous silicide layer with a composition close to Fe_3Si. Above 5ML the reaction slowed down at RT and a film of metallic polycrystalline Fe, with some Si dissolved, developed. Moritz et al [13] showed, using real time reflection high-energy electron diffraction (RHEED), that the reaction of the two species at the interface at RT relied upon the fact that Fe was a fast diffusing species and the diffusion mechanism was purely interstitial [14]. Up to a coverage of 0.3 nm Fe, the intermixed region exhibited an average Si:Fe concentration ratio near or slightly higher than 2:1. With increasing Fe coverage, the surface became increasing Fe-rich. Alvatez et al [22] reported results based on XPS studies that a Fe_3Si_{1-y} type compound formed spontaneously when depositing small Fe coverages (< 2ML) at RT on Si (111). The appearance of the Fe_3Si phase was the first reaction step.

2.5.2.1.2. *Fe/Si Interface Annealing Behavior*

Early studies [15] of the Fe/Si system using Rutherford backscattering spectra (RBS) and X-ray diffraction (XRD) showed that Fe_3Si and FeSi formed after annealing a 134 nm Fe film on Si (100) at 450-525°C. At 550°C, an $FeSi_2$ phase grew between the Si substrate and ε-FeSi. The formation sequence was the same on Si (111), although the silicides formation rates were slightly lower. Transmission electron microscope (TEM) investigations [16] found that, for 30 nm Fe films deposited on Si and annealed in N_2 ambient, FeSi was formed at 400°C. Small amounts of Fe_3Si were observed at 450-500°C. Above 600°C, β-$FeSi_2$ was the dominant phase. α-$FeSi_2$ was observed only at temperatures above 800°C. XRD results [115] indicated that, for 150 nm Fe films deposited on Si (100), Fe_3Si and FeSi appeared after annealing at 600°C and 700°C, respectively. At 750°C a mixture of FeSi and β-$FeSi_2$ was obtained, while for temperatures between 800°C and 900°C only β-$FeSi_2$ was observed. At higher temperatures (1050-1100°C) only metallic α-$FeSi_2$ formed. More recent TEM results [142] showed that a Fe_3Si layer formed at 300°C and 400°C; at 400°C, the Fe_3Si and FeSi layer grew simultaneously; β-$FeSi_2$ formed above 600°C.

For all the experiments mentioned above, depositions were done under conventional vacuums (10^{-6} - 10^{-7} torr). In UHV, and for much thinner Fe films (2 -3 nm)

deposited on Si (111), Auger electron spectroscopy (AES) and electron energy loss spectroscopy (EELS) [115,117] have shown that FeSi formed at temperatures ranging from 350-500°C. β-$FeSi_2$ appeared between 500°C and 650°C. On Si (100), FeSi appeared at 300-425°C, and $FeSi_2$ between 500°C and 625°C. More recently, AES and low energy electron diffraction (LEED) results [5] have indicated, that under UHV deposition conditions, Fe_3Si formed first at 100-200°C, followed by FeSi at 350-450°C, and $FeSi_2$ at 550-650°C.

2.5.2.2. *β-$FeSi_2$ Heteroepitaxy on Si*

2.5.2.2.1. *Heteroepitaxy on Si (100)*

The first evidence of successful β-$FeSi_2$ epitaxy on Si (100) was demonstrated by Cherief et al [76, 119]. These authors used Si (100) faces in order to favor epitaxial growth. LEED, Auger and photoemission spectroscopy were used to probe their thin films. The following epitaxial relationships were found:

(1) for matching planes, β-$FeSi_2$ (100) //Si (100);

(2) for azimuthal orientations, β-$FeSi_2$ [010] and [001] // Si [110].

2.5.2.2.2. *Heteroepitaxy on Si (111)*

Samples, a few tens of nm in thickness, prepared by SPE or RDE at ~600°C, display the following epitaxial relationships [111]:

(1) for matching planes, β-$FeSi_2$ (101) // Si (111);

(2) for azimuthal orientations, β-$FeSi_2$ [010] // Si [011].

Since β-$FeSi_2$ crystallizes in an orthorhombic structure with only a very small difference between the b and c axis (a = 0.986 nm , b = 0.779 nm, c = 0.783 nm), there are other epitaxial relationships [6]:

(1) for matching planes, β-$FeSi_2$ (110) // Si (111);

(2) for azimuthal orientations, β-$FeSi_2$ [001] // Si [011].

The differences in lattice parameters are respectively -5.3% (-5.5%) along the [121] azimuth of silicon and +1.4% (+2%) along the [110] azimuth for (101) or (110) epitaxy of $FeSi_2$ on silicon (111). These relationships have been clearly established by various techniques (LEED [76], RHEED [77], TEM [16]).

2.5.2.2.3. *Strained Metastable Cubic $FeSi_2$ Heteroepitaxy on Si (111)*

Strained metastable cubic $FeSi_2$, referred to as γ-$FeSi_2$, was observed recently by a template method with a subsequent MBE growth at low temperature [78, 79, 117], by SPE [77, 42] with very low thicknesses (few nm) and by RDE [119, 120]. The authors agreed that cubic $FeSi_2$ with a lattice parameter very close to that of Si can be stabilized on the Si (111) substrate. The cubic $FeSi_2$ layers display a 2 x 2 superstructure as observed by LEED and RHEED and, in agreement with Christensen's calculations [121], they have a metallic behavior as displayed by their photoemission spectra with a metallic Fermi edge. The properties (reconstructed 2 x 2 surface and metallic behavior) have been confirmed by high resolution electron energy loss spectroscopy (HREELS) [15] and by scanning tunneling microscopy (STM) investigations [122]. Recently Derrien et al [116] showed that cubic $FeSi_2$ relaxes to the equilibrium β-$FeSi_2$ phase during RDE growth. At higher temperatures, thermal diffusion rates of Si are higher and $FeSi_2$ is readily formed for any deposited Fe coverage. Due to a strong film-substrate interaction, the cubic, metallic, strained $FeSi_2$ phase first grows and then relaxes towards the orthorhombic semiconducting β–$FeSi_2$ phase at a critical thickness.

2.5.3. Growth Kinetics of Iron Silicides Fabricated by SPE.

Up till now only a few investigations of the growth kinetics of iron silicides formed by SPE have been performed. The thickness of FeSi layers increased with the square root of time, which is indicative of diffusion-limited growth [120, 122]. The corresponding activation energies were reported to be 1.67 ± 0.15 eV and 1.36 ± 0.25 eV. The small difference may be due to a difference in the microstructures of samples grown by normal furnace annealing and by RTA [122].

Nucleation control for the formation of β–$FeSi_2$ was reported by Dimitriadis et al [20] and Freiburg [15], who showed that β–$FeSi_2$ grew more or less in columnar patches through the FeSi layer instead of in a layer by layer fashion. This result was confirmed by Baldwin and Ivey's TEM studies [123]. β–$FeSi_2$ initially nucleates at well-separated spots, e.g., grain boundaries in the FeSi layer or stress-induced "weak" spots at the interface [124]. An activation energy of 2.6 ± 0.5eV has been reported [15].

2.5.4. The Effect of Oxygen on the Formation of Iron Silicides

Various studies on the effect of oxygen on silicide formation have been performed [126-129]. From these studies it is known that the presence of oxygen may significantly

influence silicide formation. The amount of influence depends on the amount and distribution of oxygen with respect to the moving species, the annealing temperature, and the affinity between oxygen and the moving species. If the metal is the diffusing species during silicide formation and oxygen is present in the metal, the oxygen concentration at metal-silicide interface increases during annealing. It is assumed [127] that as the metal diffuses into the already formed silicide, more oxygen in the metal film will be exposed to silicon at the metal-silicide interface to form SiO_2. The SiO_2 builds up during annealing and eventually obstructs metal diffusion. If silicon is the diffusing species, the oxygen is stationary with respect to the metal during silicide formation, as was found for $CrSi_2$ by Lien et al [128]. Chemelli et al [121] have demonstrated that a thin native oxide layer on a Si (111) single crystal is an efficient barrier to the formation of an ultra-thin iron silicide layer at the Fe/Si interface at RT. At temperatures higher than 450°C, however, this thin oxide barrier is no longer effective in preventing silicide formation. In the pure Fe/Si interface case, it is Si diffusion in the silicide that is the dominant mechanism for the compound formation. In the presence of an oxide layer, the mechanism responsible for the formation of compounds is the diffusion of the metal through the oxide, leading to an SiO_x / FeSi / Si or SiO_x / $FeSi_2$ / Si type of structure. Swart et al [129] found that in Fe/Si (100) samples with a low concentration (2at%) of oxygen in the Fe film, Fe is the main diffusion species for FeSi formation. According to the literature [122], Si is the diffusion species during FeSi formation for samples without oxygen. The presence of oxygen, gettered in an iron layer, therefore changes the diffusion species from Si to Fe during FeSi formation. During formation of FeSi, SiO_x is formed at the Fe/silicide interface and acts as a diffusion barrier. The presence of higher concentrations of oxygen in Fe layer prevents silicide formation due to FeO formation.

2.6. A Comparison Between Bulk And Thin Film Phase Formation

Analysis of the kinetics of formation of silicides in bulk diffusion couples is necessary to understand the behavior of thin films for different reasons [130]: 1) Bulk diffusion couples may be studied over a wider and different temperature range; 2) the influence of interfaces should be less pronounced; 3) layer thicknesses may also vary over a wider range.

Kinetics of multiple-layer compound growth in bulk couples and kinetics of single -layer compound growth in thin films was studied some years ago by Tu et al [132]. For bulk couples, a silicide layer, β, may be characterized by an essentially constant chemical

interdiffusion coefficient D_β^*, a steady state of diffusion fluxes, and compound formation only occurring at the interface. The growth kinetics can be described as follows:

$$\frac{dx_\beta}{dt} \approx G_\beta \Delta C_\beta^{eff} k_\beta^{eff}, \quad \text{for } x_\beta << x_\beta^* \tag{2-20}$$

$$\frac{dx_\beta}{dt} \approx G_\beta \Delta C_\beta^{eff} \tilde{D}_\beta / x_\beta, \quad \text{for } x_\beta >> x_\beta^* \tag{2-21}$$

or in integrated form,

$$x_\beta \propto t, \quad \text{for } x_\beta << x_\beta^* \tag{2-22}$$

$$x_\beta \propto t^{1/2}, \quad \text{for } x_\beta >> x_\beta^* \tag{2-23}$$

x_β and t are the silicide layer thickness and annealing time, respectively, k_β^{eff} is a constant and is called the effective interfacial reaction barrier, ΔC_β^{eff} is the difference between the equilibrium concentrations of the diffuser at the two interfaces of the β. G_β is a constant determined by the compositions of the involved phases and x_β^* is a transition thickness for the β phase. Eqs. (2-20), (2-21), (2-22) and (2-23) indicate that the growth process is interface reaction-controlled, when $x_\beta << x_\beta^*$, whereas the growth process is diffusion-controlled, when $x_\beta >> x_\beta^*$. According to Tu et al [131, 132], whenever planar growth of a compound takes place, it should pass through two stages. Initially, growth will follow interface controlled kinetics. After the layer has grown so that the condition $x_\beta >> x_\beta^*$ is satisfied, the process will change over to diffusion controlled growth kinetics.

For thin films, intermetallic compounds tend to form alone; that is, they grow one by one in sequence rather than together at the same time. Hence, the theory of diffusion-controlled growth is clearly inadequate in explaining the phenomenon of "single" intermetallic compound growth in thin film interdiffusion. A simple model which combines diffusion-controlled growth and interfacial-reaction-controlled growth has been proposed to explain unique thin film behavior [133]. In this model, the most important point is the critical thickness of the phases (β and γ), x_β^c and x_γ^c. Below these thicknesses only single phase ($A_\beta B$ or $A_\gamma B$) (see Fig.2-6) growth occurs, whereas above these critical values simultaneous growth of two phases must result. Single layer growth can be explained from Fig.2-7. In Fig.2-7, vertical axis is flux ratio, referred as to r; horizontal axis is annealing time, referred as to t. If there is unlimited supply of A and B, sooner or later, $A_\gamma B$ (assuming it forms first) can grow and exceed x_γ^c. At this point, two compounds ($A_\gamma B$ and $A_\beta B$) grow at same time. If the material supply, for example B, is consumed before $x_\gamma > x_\gamma^c$, the thickening of $A_\gamma B$ will stop. After a short transition period a new steady-state diffusion situation will develop, which may approximately be described by $J_\gamma^B = 0$. J_γ^B is the flux of B through the γ phase. Thus, $\frac{dx_\beta}{dt} > 0, \frac{dx_\gamma}{dt} < 0$, which indicate that $A_\beta B$ will form and grow whereas $A_\gamma B$ will shrink. Whether single phase or

multiple phase growth occurs depends on whether the interdiffusion zone is below or greater than the critical thickness of first growing phase. It is conceivable, then, that single phase growth could occur provided a clean interface without oxides and impurities could be prepared between the two starting materials of the thin film couple.

The kinetics aspects were also analyzed recently in three systems: Ni/Si [132], Ti/Si [131], and Co/Si [134, 135]. For bulk diffusion couples, two layers of metal and silicon were maintained in intimate contact and annealed. Phase formation taking place at the metal/silicon interface was analyzed by optical microscopy, scanning electron microscopy (SEM) and EDS. The following results were obtained.

In the Ni/Si system, 5 phases were observed to grow simultaneously: Ni_5Si_2, $\delta-Ni_2Si$, $\varepsilon-Ni_3Si_2$, NiSi and $NiSi_2$. Ni_3Si_2 had the fastest kinetics of formation and grew in a very irregular fashion, i.e., "finger-like", into the silicon substrate [131]. The growth of NiSi and $NiSi_2$ occurred adjacent to the $\varepsilon-Ni_3Si_2$ "fingers" on the Si side of couple. At higher annealing temperatures Ni_5Si_2, $\delta-Ni_2Si$, $\Theta-Ni_2Si$ (stable at $T > 820^oC$), NiSi and $NiSi_2$ grew by diffusion controlled mechanisms. The highest rate of formation was obtained for $\Theta-Ni_2Si$. For the other phases, with a more limited range of solubility, the rates of formation decreased with increasing silicon content in the phases.

The Co/Si system was studied between 850-1000°C. At the scale of the observations made, Co_2Si, CoSi and $CoSi_2$ were found to grow simultaneously according to diffusion controlled kinetics. CoSi had the highest rate of formation followed by Co_2Si and then $CoSi_2$.

The Ti/Si system was studied in the temperature range 800-1000°C. Ti_5Si_3, Ti_5Si_4, TiSi and $TiSi_2$ grew simultaneously. The kinetics of growth were parabolic. The rates of formation decreased with the titanium content in the phases.

All silicides obtained from bulk couples in these three systems were also obtained during annealing of thin films. Comparing bulk couples with thin films, three notable differences can be found. The first one is the rates of growth of most silicides in the thin films are much higher than in their bulk couple counterparts. Comparing Ni_2Si formation rates in thin films with Ni lattice and grain boundary diffusion coefficients in bulk Ni_2Si, Gas et al [130] found that volume diffusion coefficients were really too low to explain the very rapid growth of thin films and a better agreement was obtained with grain boundary diffusion (gb) coefficients. This is a strong evidence that the growth of thin films in Ni/Si system is controlled by gb diffusion.

The second difference is that the reaction temperatures for thin film couples are much lower than those for bulk couples. One of the main reasons for this is that the films generally contain high densities of point defects, such as vacancies, and low temperature

short circuit paths for diffusion, such as grain boundaries and dislocations. Dial et al [134] found that Co atoms diffused through both the Co layer and CoSi layer, by a vacancy mechanism, during the CoSi growth in a Co/Si thin film couple. Comrie and Egan [135] reported that Si was the dominant moving species in both polycrystalline and epitaxial Pd_2Si growth and diffusion took place through a vacancy mechanism. Some studies have provided results demonstrating how defects can affect reaction kinetics. For instance, when metal contacts of TiPdAg, MaPdAg and NiAg to Si are capped with Ta_5O_2, the thermal reactions between the metals and Si are either suppressed or enhanced, depending on the contact system [136]. This is because the capping layer suppresses both the generation and annihilation of vacancies, which are necessary to support the reactions, at the free surface of the metal.

Diffusion studies can be complicated significantly by the presence of a high density of defects. A self diffusion coefficient measurement from a bulk sample is not necessarily the same as that in a thin film sample of the same material [135]. The high density of vacancies in the thin film will result in a smaller activation energy or larger diffusivity for self diffusion, because the vacancy concentration is much higher than the equilibrium value. If, during thermal reaction, vacancies are annihilated faster than they are generated, the diffusivity will decrease with annealing time. If the metal is the major diffuser in the growing silicide, then both the diffusion of metal atoms in the silicide and the reaction kinetics will be affected by the diffusivity change in the metal film [137]. For TiSi, a comparison between thin film and bulk diffusion couples and trace diffusion coefficients shows that the kinetics of thin film growth is anomalously slowed at low temperature. This is explained by a decrease in the grain boundary diffusion efficiency at low temperature, probably due to oxygen contamination. Consequently, the kinetics of thin film formation is also highly dependent on the oxygen content of the film.

The third difference is that for thin films, silicides tend to grow one by one or sequentially; for bulk couples, silicides grow simultaneously. Recently, a kinetic model has been proposed by Zhang and Ivey [138, 139, 140] to describe solid state reactions in thin metal film-silicon diffusion couples. This model overcomes the main disadvantages of other models, i.e., which do not consider interfacial barrier and interface energies. Their focus was concentrated not only on the first phase formation sequences, but also on single phase formation sequence and, particularly, multiple phase formation sequences. The model considers real reaction processes involving competition among nucleation rates and growth rates of all possible phases instead of only growth rates or nucleation rates.

In this model, one species is considered to be the moving reactant, while the other is considered to be a non-moving reactant. A reaction region is defined at the interface

between the metal and silicon. One element is assumed to diffuse considerably faster than the other and is defined as the moving reactant (M). The other element is then the non-moving reactant. A reaction process plot, which is a plot of the release rate of the non-moving reactant (r) vs. the diffusion rate of the moving reactant (J), can be used to predict the silicide formation sequence. A schematic reaction process plot for reactions between a moving reactant and a non-moving reactant is shown in Fig.2-8 [139]. There are three superimposed solid curves (for silicides 1, 2 and 3) shown. Each curve represents an r vs. J curve for a given silicide, whose composition is indicated by the slope of the inclined segment of the curve. A stepped curve is drawn along the border of the superimposed r vs. J curves, and this curve represents the highest release rate at any given diffusion flux. For a given diffusion flux, J_o, there are a number of possible reactions in the reaction region. The release rates can be found by drawing a vertical line at J_o. The intersection of the ith solid curve with the vertical line indicates the release rate r_i, for ith silicide formation. According to this model, the silicide that will form will be the one with the highest release rate (e.g., r_2 for silicide 2 in Fig.2-8) [138]. The model predicts that, in principle, any silicide in the equilibrium phase diagram of a metal-Si diffusion couple can form first if the release rate for this reaction is on the stepped curve of the reaction process plot, and if the initial diffusion flux is between J_{LC} and J_{UC}, the lower and upper critical fluxes respectively for that silicide. Furthermore, the model is able to predict when and which new silicide starts to form in a diffusion couple, providing reaction process plots for this couple, are available. The diffusion flux continuously decreases as the first phase grows. When the diffusion flux reaches a critical value (J_{2LC} in the example shown), a new reaction (the formation of silicide 3) with its release rate (r_{3max}) related to the J_{UC} for that silicide (J_{3UC} for this example) is initiated and a new silicide starts to grow. This model has been successfully used to explain single phase formation sequences and multiple phase formation sequences in thin film silicide growth [135, 139].

Table 2-1. Fe_3Si neighbor configurations.

No. of shell	1	2	3	4	5	6	7	8
Neighbor distance as a function of lattice parameter	0.43	0.5	0.75	0.83	0.86	1	1.08	1.11
A, C	4B 4D	6A,C	12A,C	12B 12D	8A,C	6A,C	12B 12D	24A,C
B	8A,C	6D	12B	24A,C	8D	6B	24A,C	24D
D	8A,C	6B	12D	24A,C	8B	6D	24B,C	24B

Table 2-2. Binding energy computations (Ryd): E_{Si}^{s}= 0.051, E_{Si}^{p} = 0.882 , E_{Fe}^{d} = 0.735, Δ = 0.047 [61].

	Neighbor considered		
	1	2	3
ssσ	0	0	-0.0108
spσ	0	0	0.015
sdσ	-0.0129	-0.00084	0
ppσ	0	0	-0.0628
pdσ	-0.0878	-0.0494	0
pdπ	0.0507	0.0285	0
ddσ	-0.0563	0.0285	0
ddπ	0.0257	0.0083	0
ddδ	-0.003	-0.0008	0

Table 2- 3 Structural Data for Semiconducting Silicides [83].

Phase	Structure type	Space group	Molecules/ unit cell	a (nm)	b (nm)	c (nm)
$CrSi_2$	hexagonal	$P6_266$	3	0.44313	-	0.6364
β-$FeSi_2$	orthorhombic	Cmca	16	0.9863	0.7791	0.7833
$MnSi_{1.7}$	tetragonal					
Ru_2Si_3	orthorhombic	Pbcn	8	1.1075	0.8934	0.5533
$ReSi_2$	orthorhombic	Immm	2	0.3128	0.3144	0.7677
OsSi	cubic	$P2_13$	4	0.4735	-	-
Os_2Si_3	orthorhombic	Pbcn	8	1.1157	0.8964	0.5580
$OsSi_2$	orthorhombic	Cmca	16	1.0144	0.8108	0.8218
Ir_3Si_5	monoclinic	$P2_1/2$	8	0.6406	1.4162	1.1553

Table2-4 Experimental and theoretical energy gaps for semiconducting silicides at room temperature [83].

Phase	Experimental gap (eV)	Type of gap (experimental)	Theoretical gap (eV)	Type of gap (theoretical)
$CrSi_2$	0.35[84] 0.5 [93] 0.67 [94] 0.9 [94]	indirect direct indirect direct	0.21-0.38 [95-98] 0.37-0.47 [95-98]	indirect direct
$MnSi_x$	0.46 [95]	indirect		
β-$FeSi_2$	0.78 (E_g+E_{ph})* [87] 0.75 [88] 0.84-0.87 [89,92]	indirect indirect direct	0.78, 0.74 [99] 0.82, 0.85 [99]	indirect direct
Ru_2Si_3	0.9 [91]	?	0.23	direct
$ReSi_2$	0.12 [92] 0.36 [92]	indirect		
OsSi	0.34 [93]	?		
Os_2Si_3	2.3 [93]			
$OsSi_2$	1.4 [93]			
Ir_3Si_5	1.56 [94]	direct		

* E_g is gap energy; E_{ph} is phonon energy

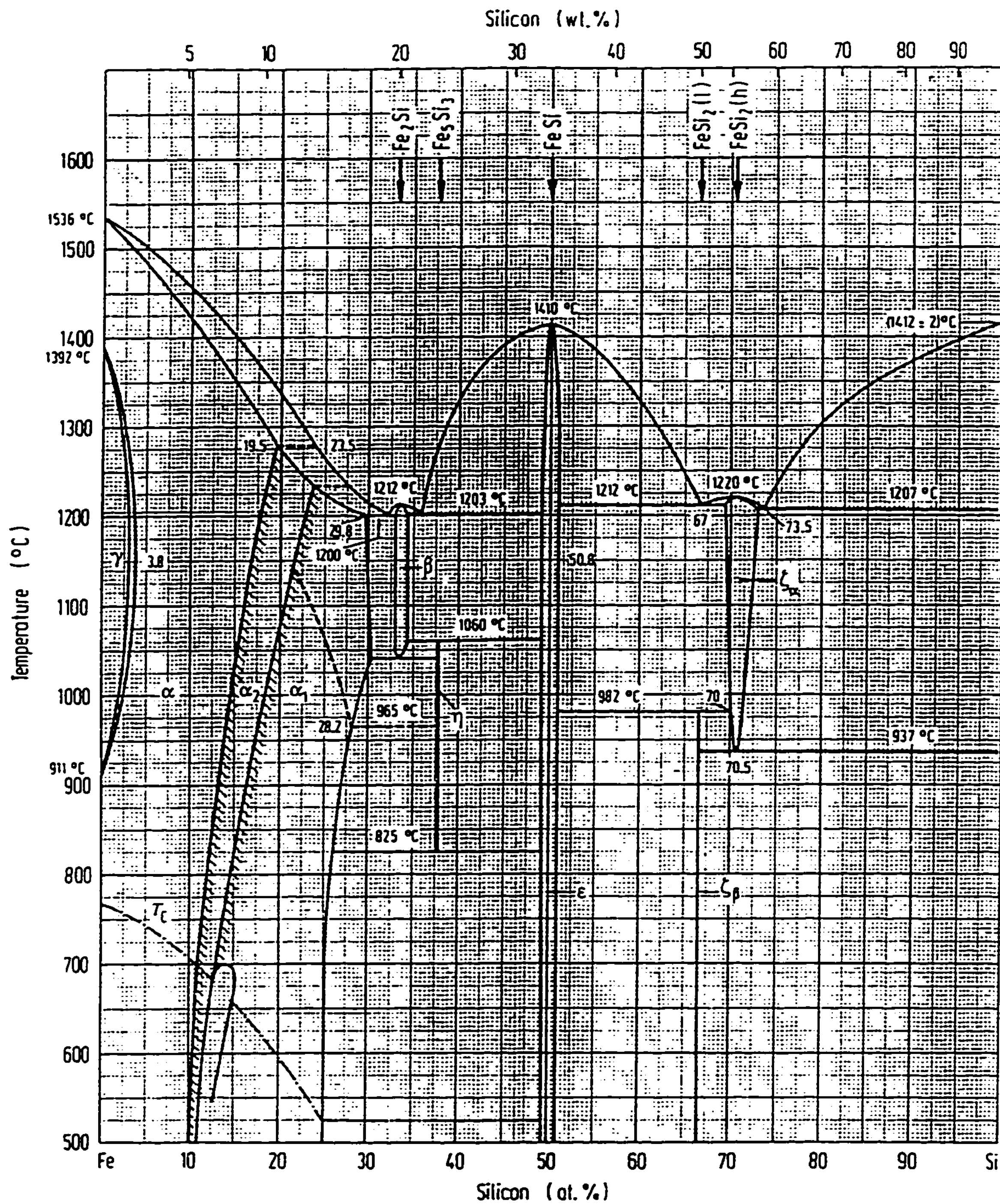

Fig.1-1 Fe-Si phase diagram [7].

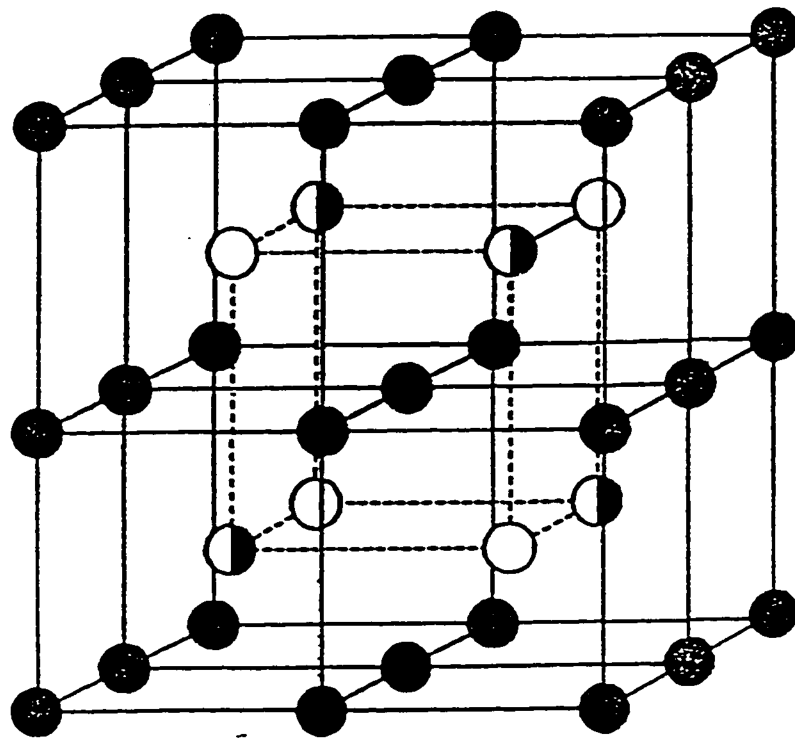

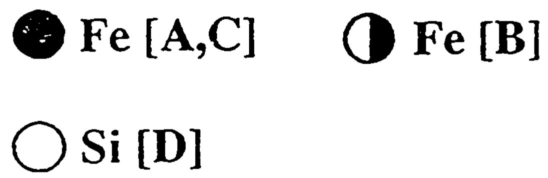

Fig.2-2 Stoichiometric Fe_3Si, DO_3 structure [27].

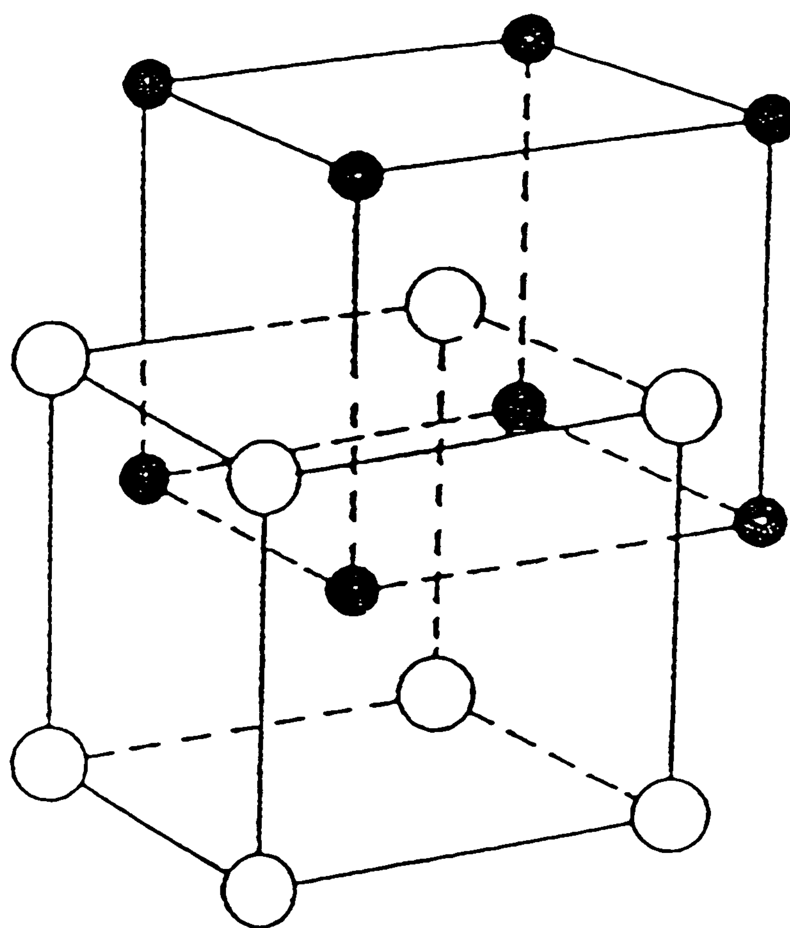

Fig.2-3 Off-stoichiometric Fe_3Si, B2 structure [50].

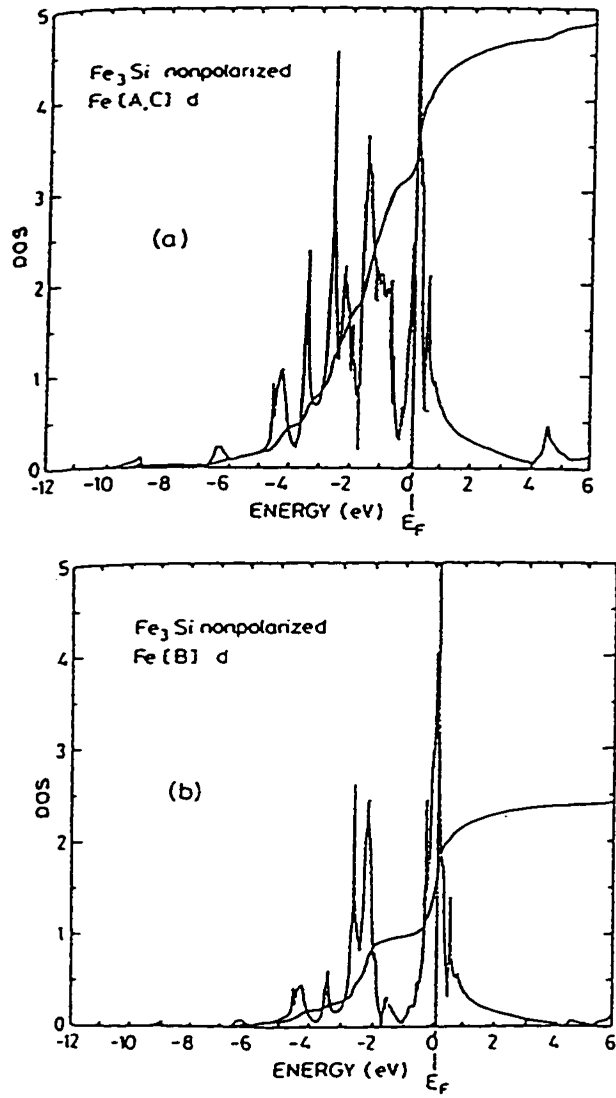

Fig.2-4 Fe_3Si. a) Fe [A,C]'s density of states function calculation without spine polarization; b) same as (a) but for the B sites.

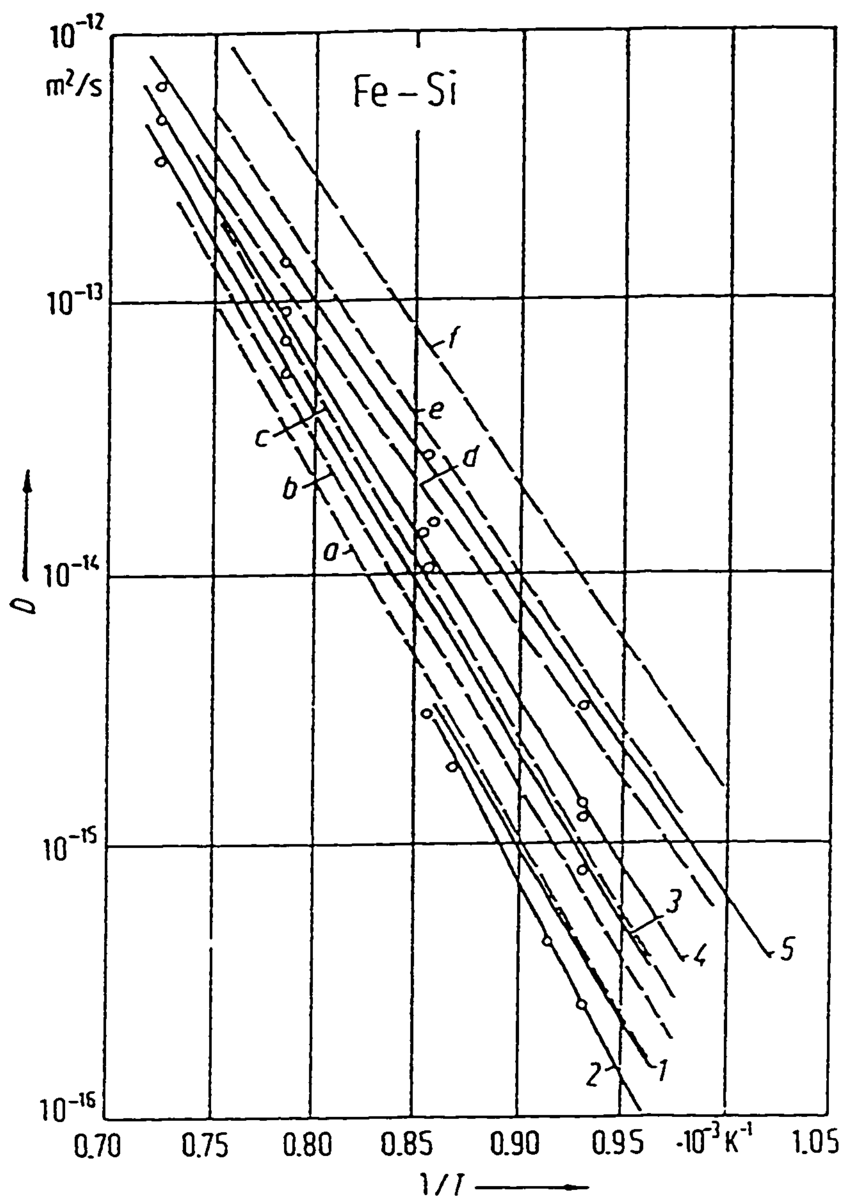

Fig.2-5 Fe-Si (1.87-19.2 at% Si). ^{59}Fe diffusion coefficient vs. reciprocal temperature for various Si concentrations (at%). Curve 1: 0; 2: 1.87; 3: 6.55; 4: 8.64; 5: 12.1. Curve a: 5.5; b: 6.5; c: 7.8; d: 11.6; e: 15.3; f: 19.22 [73].

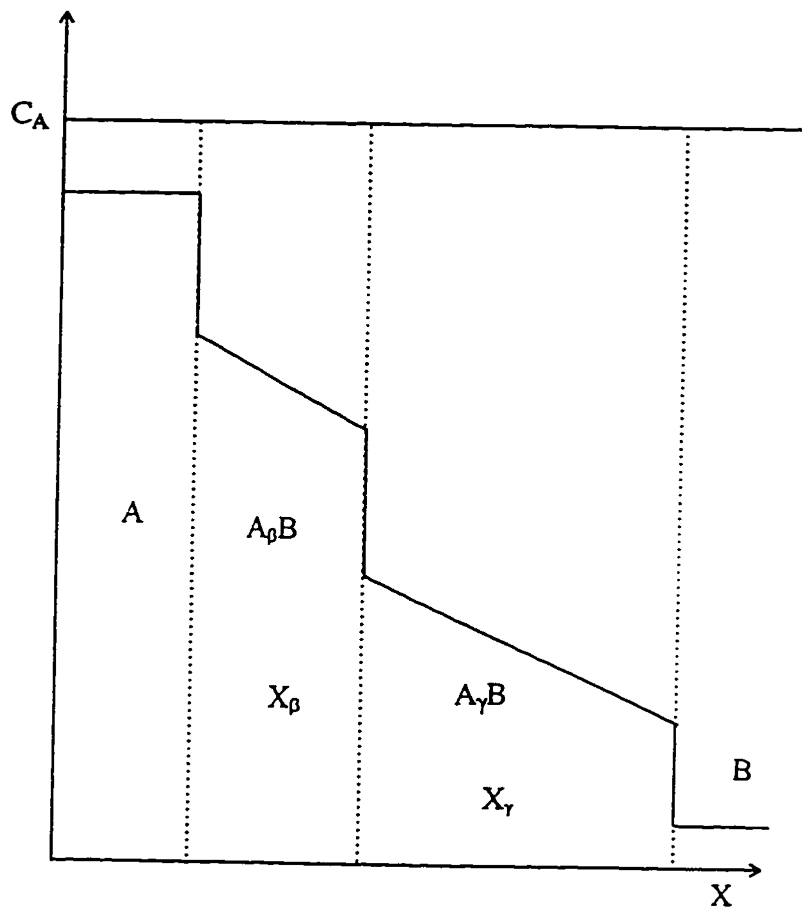

Fig. 2-6 Schematic diagram of concentration profile of A atoms in the simultaneous growth of two compounds $A_\beta B$ and $A_\gamma B$, between A and B.

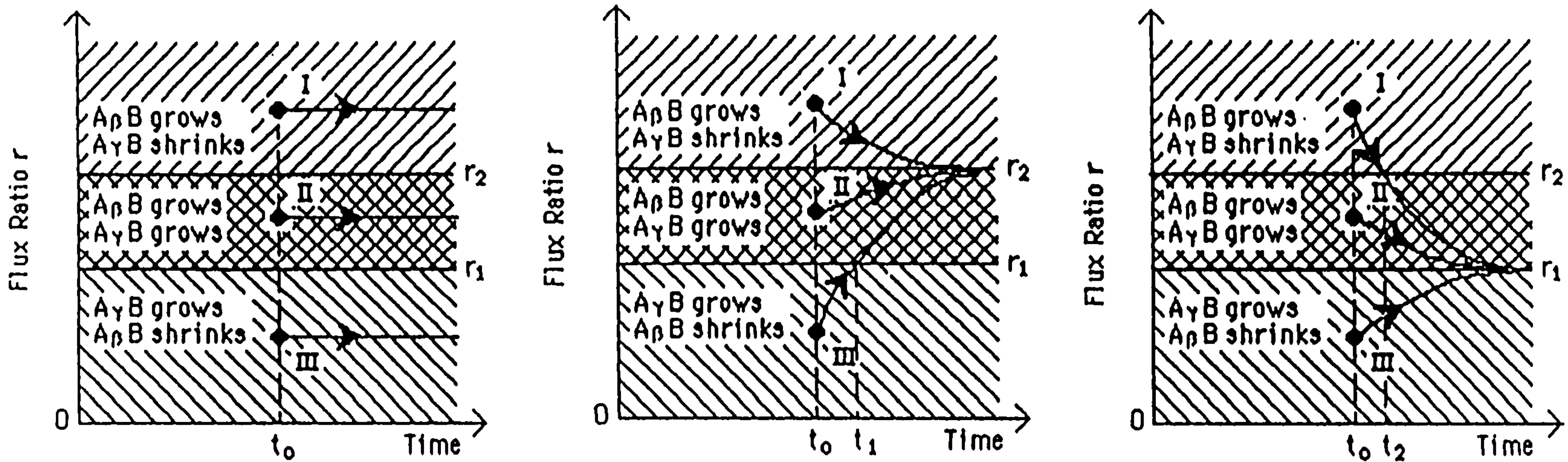

Fig.2-7 Schematic of growth/shrinkage behavior vs time. (a) It is assumed that the transport across both layers ($A_\beta B$ and $A_\gamma B$) is interface reaction controlled, $x_\beta << x^*_\beta$ and $x_\gamma << x^*_\gamma$. The flux ratio is independent of the layer thicknesses and is determined by κ^{eff}_β and κ^{eff}_γ. (b) It is assumed that transport across the $A_\gamma B$ layer is diffusion controlled, whereas transport across the $A_\beta B$ layer is interface controlled. At time $t = t_1$, in case III, the growing $A_\gamma B$ layer has reached its critical thickness x^c_γ. (c) It is assumed that transport across the $A_\beta B$ layer is diffusion controlled, whereas transport across $A_\gamma B$ layer is interfacial controlled. At time $t = t_2$, in case I, the growing $A_\beta B$ layer has reached its critical thickness x^c_β [146].

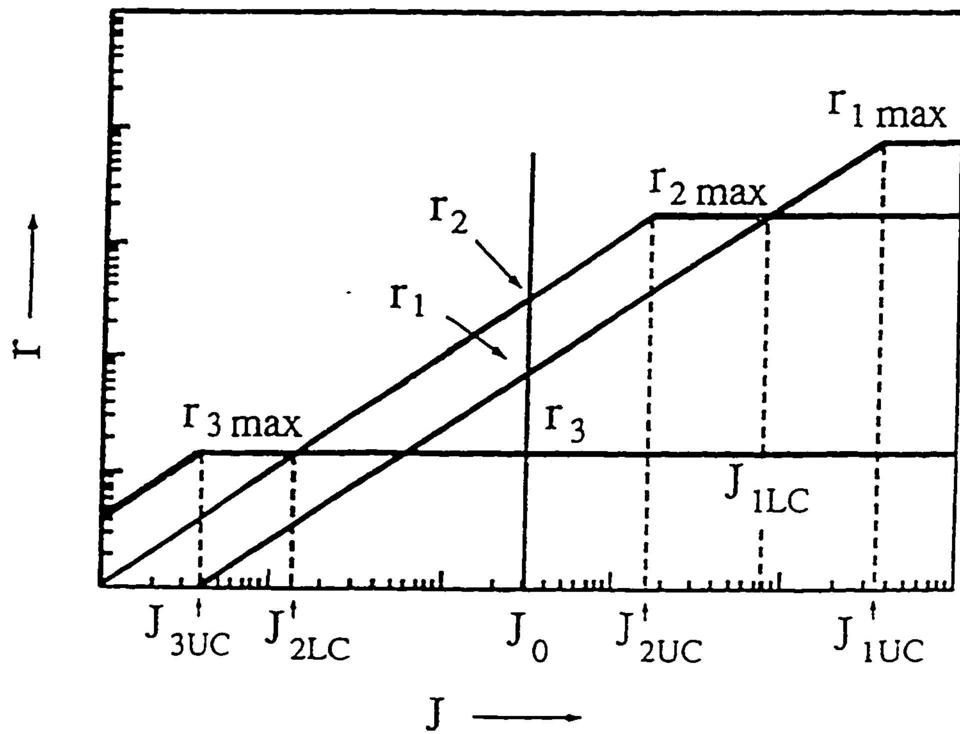

Fig.2-8 Schematic reaction process plot for silicide formation in a thin metal film-Si diffusion couple [139].

Chapter 3. Bulk Diffusion Couples

3.1. *Experimental Methods*

3.1.1. *Fabrication of Fe/Si Alloys*

The starting materials were 99.98% iron and single crystal silicon. Small pieces (3-4 grams) of alloys were produced in an induction furnace under an inert atmosphere (10% Ar and 90% He). The mass losses should not exceed 0.3 % using the method reported in [143]. Homogenization annealing was done in N_2 ambient at 1000°C for 24 hours. Four nominal alloy compositions were made: $Fe_{89}Si_{11}$, $Fe_{85}Si_{15}$, $Fe_{78}Si_{22}$, and $Fe_{75}Si_{25}$, referred to as Alloy A, Alloy B, Alloy C and Alloy D respectively.

3.1.2. *Fabrication of Bulk Diffusion Couples*

Bulk diffusion couples were made by clamping pieces of high purity Fe and Si or Fe and Fe/Si alloy together between steel plates. The Fe was originally in the form of 6.3 mm diameter rod with a purity of 99.98 %. The Si was a cylindrical single crystal, ‹111› oriented rod, about 22 mm in diameter. The Fe/Si alloys were produced as described above in an induction furnace. Fe pieces were cut from the Fe rod perpendicular to the rod axis with a low speed diamond saw, so that all of Fe pieces would have the same circular area on their ends. Slices were cut, from the silicon and alloys with the diamond saw, and these slices were subsequently cut into smaller pieces. All the Si and alloy pieces were cut so that their contact areas with the Fe surfaces would be at least 25 mm^2.

The surfaces of the Fe, Si and alloys pieces were ground and polished. The faces of the pieces that were to be the reacting interfaces were polished to a mirror finished on a 6 μm diamond wheel and a 0.05 μm Al_2O_3 wheel. Polishing, especially in the case of Fe, was done only shortly before fabrication of the couples so as to prevent oxidation of the polished surfaces.

The clamping device for each couple consisted of two square carbon steel plates, measuring 20 mm by 20 mm and about 2 mm in thickness. Four corner holes were drilled in each plate so that the plates could be tightened with screws. The four corners of each plate were ground to arcs parallel to the corner holes. The bottom plate of each pair had threaded holes while the holes in the top plate were slightly larger and unthreaded. Threading the bottom holes eliminated the need for nuts. Fig.3-1 is a schematic diagram of

a clamp plate. The screws used were 1/2 inch (12.7 mm) long uncoated carbon steel 4-40 screws with hexagonal heads so that they could be tightened with an Allen key.

Clamping plates and screws were ultrasonically cleaned in acetone and ethanol. The polished Fe and alloy surfaces were wiped and rinsed in acetone and ethanol and immediately blown dry with N_2. The polished Si surfaces were also wiped clean in acetone and ethanol, then etched in buffered oxide etch for 60 seconds, rinsed in distilled water, and blown dry with N_2. A Si piece or alloy piece and an Fe piece were stacked, polished surfaces together, between each pair of steel plates and the four screws tightened by hand with an Allen key. Care was taken to tighten the screws so that the plates would remain parallel and pressure uniform.

3.1.3. Annealing

To protect the diffusion couples from oxidation during the annealing, the couples were sealed in evacuated quartz glass tubes. Each tube contained 1.0 g of pure zirconium powder as well as a diffusion couple. The purpose of the Zr was to getter the oxygen still present inside the tube so that surface oxide would not prevent silicides from forming. The vacuum of tubes was about 10^{-4} torr when just sealed. Once at high temperature, the Zr acted to further lower the oxygen pressure to below the decomposition pressure of SiO_2 and all Fe oxides. All oxides, including the inner surface of the quartz were reduced by the preferential oxidation of the Zr. This was shown previously by Baldwin [142], as much cleaner and shinier Fe and steel surfaces were observed after removal from the tubes than prior to annealing.

Furnace controllers were adjusted to maintain the proper temperatures by calibration with an external thermocouple that was accurate to within 1 degree Celsius. The diffusion couples were placed quickly into the furnaces, which were already at the annealing temperature. About 10 minutes after inserting the couple, the furnace temperature would be stable on the setpoint.

The annealing times for sealed couples ranged from 234-1650 hrs. In order to observe first phase formation, two unsealed samples were annealed in a tube furnace at 700°C for less than 50 hrs in N_2 ambient.

3.1.4. Sample Preparation

3.1.4.1. TEM Sample Preparation

Alloys were cut into slices with a thickness of about 2 mm. The slices were cut into small pieces with diameters less than 1 cm. A small piece was then ground from both sides by mounting it, with low melting point wax, on a grinding jig. The sample was ground to about 100 μm thickness, then cut with a sharp knife into an approximately 3 mm diameter disc.

Chemical thinning was used to further decrease the disc thickness. The chemical thinning solution was 0.1 % perchloric acid, 2.5% hydrofluoric acid and 97.4 % methanol. The sample was fixed on the specimen holder and put into the solution for 20-25 seconds. The sample was cleaned in acetone. The final thinning was done by ion milling in a Gatan Duo Mill 600 CTMP. Two Ar^+ ion guns were employed to sputter the sample at an angle of 25 °C to horizontal, with an accelerating voltage of 4 kV. The ion gun current varied from 0.4 mA to 0.5 mA. The sputtering time was from 4-10 hrs depending on thickness of sample after chemical thinning.

3.1.4.2. SEM Sample Preparation

3.1.4.2.1. Bulk Couples

After annealing and cooling to room temperature, diffusion couples were removed from the quartz tubes and compressed air was used to blow away the Zr powder. Each diffusion couple was mounted in about 20 ml of cold mount material, which cures at room temperature. The mounted couple was then cut perpendicular to the reaction interface with a low speed diamond saw. Of the two halves of each couple, one was polished for examination. Polishing was done on two different polishing wheels: 1) A napless cloth with 6 μm diamond paste and an oil lubricant; 2) a napless cloth with a 0.05 μm Al_2O_3 suspension and distilled water for lubricant.

3.1.4.2.2. Fe-Si Alloys

Small pieces of the alloys were ground and polished using the same steel jig described in the preparation of TEM samples. The following polishing procedure was used: A 10 μm diamond-impregnated wheel, using water as the lubricant, was used initially. This was followed by polishing on a napless lap with 6 μm diamond paste and an oil lubricant. This was followed by polished with a napless lap with 1 μm diamond paste and an oil lubricant. The final stage was polishing on a napless lap with a 0.05 μm Al_2O_3 suspension and distilled water for lubricant. A mirror-like surface was achieved for these samples.

3.2. *Characterization*

3.2.1. *Alloy Phase Identification*

A Hitachi H-7000 TEM with an accelerating voltage of 125 keV, a JEOL-2010 TEM (200kV) equipped with a Noran, ultra thin window, Ge x-ray detector and an x-ray diffractometer with a Rigaku-Denki D-F3 generator were used for phase identification. Selected area diffraction (SAD), energy dispersive x-ray spectroscopy (EDS) and x-ray diffraction (XRD) were used in combination to identify phases in the alloys.

Selected area diffraction (SAD)

A selected aperture was used to select the desired area. A single crystal diffraction pattern consists of a simple array of bright spots; each spot represents a set of lattice planes with the same d-spacing. A polycrystalline ring diffraction pattern is formed by a large number of grains, each with exactly the same atomic array, but at different orientations to one another. Ring and spot SAD patterns were obtained with the H-7000 TEM.

Energy dispersive x-ray spectroscopy (EDS)

A JEOL-2010 TEM was used for EDS to analyze the composition of the phases. The composition in a given phase can be determined according to the following:

$$\frac{C_A}{C_B} = k_{AB}\frac{I_A}{I_B} \tag{3-1}$$

$$\frac{X_A}{X_B} = k_{AB}\frac{I_A W_B}{I_B W_A} \tag{3-2}$$

where, C_A and X_A are the concentrations of element A in weight percent and atomic percent respectively, as are C_B and X_B for element B. I_A and I_B are the intensities from element A and B in the EDX spectrum, and k_{AB} is the Cliff-Lorimer proportionality factor. k_{AB} factors can be determined empirically from standards or calculated theoretically . In this work, the k factor ($k_{Fe/Si}$) was determined from an FeSi standard.

X-ray diffraction (XRD)

X-ray diffraction patterns were recorded on a Rigaku X-ray Diffractometer equipped with a rotating anode. All experiments were carried out with CuK_α radiation at 40 kV and 110 mA. A polished alloy piece was mounted on a glass slide coated with a thin layer of petroleum jelly. The diffractometer was scanned from 10-85° 2θ, with a step scan of 0.2° for 5 seconds. PDF-2 Database Sets 1-42 (Powder Diffraction File, 1992,

International Center for Diffraction Data) were used to analysis the spectra and identify the phases.

3.2.2. Bulk Diffusion Couple Characterization

The silicide layers formed in bulk diffusion couples were characterized with a Hitachi S-2700 SEM with a Link eXL energy dispersive Si detector with a Be window. All SEM imaging was done with the backscattered electron signal, which generated average atomic number contrast between the various phases in the couples.

The principle component of the SEM work was performing EDS analysis on diffusion couples to check phase identities and composition gradients, particularlyfor Fe_3Si. Spectra were collected from pure powder standards of FeSi and used to quantify the Fe:Si ratios. All experimental spectra were collected at a working distance of 12 or 13 mm from the level surface, with the backscattered detector out, and during a 100 second live time period with a dead time of about 20% of real collection time.

Investigation of the kinetic growth behavior of silicides in bulk diffusion couples was another goal of the bulk diffusion couple work. Short time annealing was done for several diffusion couples in order to determine the critical time for each silicide to form. Various times and temperatures were chosen to calculate layer thickness as a function of time and temperature. The entire length of every diffusion couple interface was imaged and recorded with a video printer connected to the microscope monitor. From these video prints, the average thicknesses of the FeSi and β-$FeSi_2$ and Fe_3Si layers were calculated. The thickness measurements were made perpendicular to the original Fe/Si interface.

3.3. Results and Discussion

3.3.1. Fe/Si Alloys Composition Analysis, Microstructure and Lattice Parameter Calculation

3.3.1.1. Fe/Si Alloy Composition Analysis

The Hitachi S-2700 SEM was used to analyze the composition of the alloys. Six random areas, at least 50 μm x 50 μm in size, were chosen for composition analysis, using FeSi as a standard. The results are listed in Table 3-1. According to the EDS results, the alloys were homogeneous and alloy A and alloy B were off-stoichiometric Fe_3Si. Fig.3-2 shows the single phase in alloy B and alloy C.

3.3.1.2. Fe_3Si Electron Diffraction

Stoichiometric Fe_3Si has a DO_3 structure. One unit cell has 16 atoms, i.e., 12 Fe and 4 Si atoms. The atom configuration is shown in Table 3-2. Off-stoichiometric Fe_3Si has a DO_3-related structure. There are two possible atom configurations. One Si atom is replaced by 1 excess Fe atom or 2 Si atoms are replaced by 2 excess Fe atoms on specific sites, referred to as ordered off-stoichiometric Fe_3Si (see Table 3-3). The other possibility is that excess Fe atoms are randomly positioned in Si sites; this is referred to as random off-stoichiometric Fe_3Si (see Table 3-4). Based on these atom configurations, Structure Factors were calculated for stoichiometric Fe_3Si and off-stoichiometric Fe_3Si and are listed in Table 3-5. D-spacings were also calculated and these are listed Table 3-6.

Table 3-5 and Table 3-6 indicate that more reflections are allowed for ordered off-stoichiometric Fe_3Si than for ordered Fe_3Si or random off-stoichiometric Fe_3Si. It should therefore be relatively straight forward to distinguish off-stoichiometric Fe_3Si from stoichiometric Fe_3Si using electron diffraction. All d spacings listed in Table 3-6 were done assuming the same lattice parameter (that for stoichiometric Fe_3Si). The atomic radius for Fe (0.174 nm) is larger than that for Si (0.146 nm), so that as Fe_3Si becomes more non-stoichiometric (Fe-rich) there should be a corresponding increase in the lattice parameter. Quantitative lattice parameter calculations were done for the fabricated alloys, based on XRD data, and are discussed below.

3.3.1.3. Fe_3Si Lattice Parameter and Fe/Si Alloy Microstructures

Fig.3-3 shows XRD spectra from Alloy A, Alloy B and Alloy C annealed at 700°C. The d spacings for the alloys are shifted relative to those for stoichiometric Fe_3Si. This is an indication of distortion in the Fe_3Si lattice. Lattice parameter calculations are shown in Fig.3-4. Extra peaks for alloy A are identified and labeled in Fig.3-3a. The lattice parameter increases with increasing Fe concentration. Fig.3-5 shows bright field images and representative SAD patterns from the alloys. D-spacings obtained from all the SAD and the XRD patterns are listed in Table 3-7 for comparison. There is good agreement between the SAD and XRD data. In both instances the lattice parameters and d spacings increase with increasing Fe concentration.

3.3.2. Fe/Si Bulk Diffusion Couples

3.3.2.1. Phases and Compositions

Nineteen Fe/Si diffusion couples were fabricated. The annealing temperatures and times for these diffusion couples are listed in Table 3-8.

Each couple produced layers of iron silicides along its entire interface length. No Zr was detected by EDS analysis to have entered any of the diffusion couples.

Compositional gradients and phase identities were determined by EDS analysis. All annealed couples contained the same five phases, each phase having a consistent composition. The five phases and their ideal compositions are listed in the Table 3-9.

Fig.3-6 shows an SEM backscattered electron image of the interface of one of diffusion couples. The five layers mentioned can all be clearly discerned as a result of the average atomic number contrast in the backsacttering electron signal. EDS spectra were quantified against the pure powder standard of FeSi.

3.3.2.2. Fe_3Si in Fe/Si Couples.

An SEM backscattered electron image for an Fe-Si couple annealed at 700°C for the shortest time studied (7 hrs) is shown in Fig.3-7a. A corresponding composition profile is shown in Fig.3-7b. This condition clearly represents the early stages of silicide formation and demonstrates that Fe_3Si forms initially in bulk couples. No FeSi or $FeSi_2$, the other 2 phases that would be expected to form at this temperature, were detected, at least within the resolution of the SEM. Fe_3Si was found to be stoichiometric, which is in agreement with previous work [142], with a composition corresponding to 27.5 ± 0.4 at% Si, which is slightly, but consistently, above the ideal value of 25 at% Si. The slightly higher Si concentration, relative to the stoichiometric value, can be attributed to the fact that FeSi, and not Fe_3Si, was used as the standard for EDS analysis. In any case, it is clear that the composition of Fe_3Si is constant throughout the layer.

An SEM image and a concentration profile of an Fe-Si couple, annealed at 700°C for 1007 hours (longest annealing time at 700°C), are shown in Fig. 3-8. Three silicide layers, corresponding to Fe_3Si, FeSi and $FeSi_2$, appear in Fig.3-8b. The solid line is drawn through experimental data and the dashed line represents what would be expected from the phase diagram. The dashed line is different from the solid line because it does not have a third step at 25at% Si. Since, according to the Fe-Si phase diagram, there is no two-phase region between the α-Fe and Fe_3Si, the theoretical profile contains no step. The transition from one structure to another is supposed to occur smoothly with no vertical segment between the Fe_3Si and Fe. The same type of concentration profiles were obtained from all other couples. EDS results from all Fe-Si diffusion couples studied showed only stoichiometric Fe_3Si adjacent to α-Fe. More than 100 positions along the Fe_3Si/α-Fe

interface of each couple were examined in order to confirm these results. Fig.3-9 shows a concentration profile across the Fe_3Si layer in a couple annealed at 700°C. The concentration is still in the 27.5 ± 0.4 at% range.

3.3.2.3. Growth Kinetics of Fe_3Si, β-$FeSi_2$ and FeSi

The silicide thicknesses, for all bulk couples, were found to be thicker in the middle area of couples than those at the edges. This is because Fe and Si contact was better in the middle than at the edges. During fabrication of the diffusion couples, it was difficult to obtain completely parallel Fe and Si surfaces, when the Fe pieces and Si pieces were clamped together. The pressure exerted by the steel plates on the Fe and Si pieces affected the thickness of the silicides. In order to reduce error, the center portion (~200 μm) of each couple was used for thickness measurements for each silicide. Ten measurements were made per couple for each silicide layer. The average thickness of the Fe_3Si, β-$FeSi_2$ and FeSi layers for each couple were calculated and plotted. The thickness of the Fe_3Si layer is plotted as a function of the square root of the annealing time in Fig.3-10. Fe_3Si continues to grow throughout annealing and the linear dependence indicates that growth is diffusion controlled.

The early stages of FeSi formation are illustrated in the SEM backscattered electron image in Fig.3-11 of an Fe-Si couple annealed at 700°C for 23 hrs. Protrusions of FeSi can be seen extending into the Fe_3Si layer. No evidence for the formation of $FeSi_2$ was found in this sample. $FeSi_2$ was only detected after much longer annealing times, i.e., >200 hrs at 700°C. After 234 hrs, all diffusion couples were observed to have three layers, i.e., Fe_3Si, FeSi and $FeSi_2$. The Si/β-$FeSi_2$, β-$FeSi_2$/FeSi and Fe_3Si/Fe interfaces were smooth, and almost planar. Thickness vs. time plots for FeSi at 700°C are shown in Fig.3-12. FeSi growth is also diffusion-controlled.

The thickness of the β-$FeSi_2$ layer also follows parabolic growth kinetics, the rate of growth being controlled by diffusion through the layer. Fig.3-13 shows thickness vs. $t^{1/2}$ plots for β-$FeSi_2$ at 700° and 666°C respectively. These results agree quite well with those in reference [141].

3.3.2.4. Major Diffuser in Fe_3Si and FeSi

Iron appears to be the major diffuser in Fe_3Si, at least at 700°C. This is in agreement with results reported by Baker [28]. Indirect evidence to support this claim was obtained from a concentration profile of the Fe_3Si/Fe interfacial region of the couple

annealed for 23 hrs at 700°C (Fig.3-14). The Si composition decreases sharply from ~25 at% to ~1 at% at the interface. Even for couples annealed for longer times, the maximum Si concentration in α-Fe only reaches ~4 at%. This is considerably less than the maximum of ~10 at% Si (at 700°C) indicated on the Fe-Si phase diagram (Fig.2-1). Immediately adjacent the Fe_3Si/Fe interface the Si concentration must correspond to the concentration from the Fe-Si phase diagram, to satisfy local equilibrium requirements; however, Si levels in α-Fe drop off rapidly. This is an indication that only a limited amount of Si is diffusing through the Fe_3Si layer to the Fe_3Si/Fe interface and into α-Fe. Most of Fe_3Si must then form through Fe diffusion through the Fe_3Si layer and subsequent reaction with Si at the Fe_3Si/Si interface.

For the short annealing time couples, the FeSi/Fe_3Si interface was rough with FeSi protrusions extending into Fe_3Si (see Fig.3-11). It appears then that Si is the major diffuser during the initial stages of FeSi formation.

3.3.2.5. Fe/Fe-Si Alloy Diffusion Couples

An SEM micrograph and a corresponding concentration profile of the diffusion zone between Fe_3Si and α–Fe, for a couple annealed at 700°C for 120hrs, are shown in Fig.3-15. A variable composition layer, identified as off-stoichiometric Fe_3Si is present at the Fe_3Si/α–Fe interface. The layer thickness (~ 15-20μm) was of the same order as the Fe_3Si thickness in the Fe/Si couples annealed at 700°C for only 7 hrs. Other couples produced similar results, i.e., off-stoichiometric Fe_3Si formed between Fe_3Si and Fe, and the Fe_3Si growth rate was considerably lower compared with stoichiometric Fe_3Si growth in Fe/Si couples.

3.3.2.6. Fe_3Si Formation in Bulk Diffusion Couples

3.3.2.6.1. Fe_3Si Free Energy

In a phase transformation, in general, there are two main factors controlling phase formation, i.e., thermodynamics (free energy change) and kinetics. Free energy calculations can be done, taking into account chemical and magnetic interactions, using a BWG model [52]. As discussed in the Chapter 2, the configurational free energy F_k can be expressed as:

$$F_k = U_k - TS_k \qquad (2\text{-}5)$$

The internal energy can be written as:

$$U_k = U_k^o - N\{4[W + J(2q-1)^2]x^2 - 3wx^2 + \frac{3}{2}w(y^2 + z^2)\}$$

$$-NC_{Fe}C_{Si}\{4[W + J(2q-1)^2] + 3w\} + 4NC_{Fe}J(2q-1)^2 \quad (2\text{-}16)$$

with

$$U_k^o = N\{4(C_{Fe}C_{FeFe} + C_{Si}V_{SiSi}) + 3(C_{Fe}v_{FeFe} + C_{Si}v_{SiSi})\} \quad (2\text{-}7)$$

The entropy can be written as:

$$S_k = S_k^c + S_k^q \quad (2\text{-}17)$$

with

$$S_k^c = -k\frac{N}{4}\sum\{p_{Fe}^L \ln p_{Fe}^L + p_{Si}^L \ln p_k^L\} \quad (2\text{-}18)$$

and

$$S_k^q = -kNC_{Fe}\{q\ln q + (1-q)\ln(1-q)\} \quad (2\text{-}19)$$

k is the Boltzman constant.

According to reference [144], W = 2010 k-units and w = 1000 k-units (1 k-unit $=3.3\times10^{-24}$ cal $=13.8\times10^{-24}$ J). T_X and T_Y in Eq. (2-11) and (2-12) can be determined from the phase diagram. x_{min}, y_{min} and $F_k - U_k^o$ can be obtained from T_X, T_Y and the equations above, with respect to C_{Si}, assuming $z_{min}=0$. The results are listed in the Table 3-7.

The difference between the configurational free energy term (F_k) and the internal energy term (U_k^o), which is not a function of the order parameter, vs. Si atom fraction at 700°C is plotted in Fig.3-16. The free energy decreases with increasing Si fraction from 0.12 to 0.25. Thermodynamically, then, stoichiometric Fe_3Si is the most stable form of Fe_3Si and would be expected to from preferentially to off-stoichiometric Fe_3Si.

3.3.2.6.2. Atomic Diffusion Mechanism in Fe_3Si Lattice

Reaction kinetics in diffusion couples are influenced by diffusion processes. Wever and Frohberg [69] and Baker and Westerveld [70] have proposed that during diffusion in ordered DO_3 lattices, the dominant species (Fe in this case) jumps between the three Fe sublattices only, i.e., A, C and B sublattices. This model has been confirmed by Sepiol and Vogl [71] using quasielastic Mossbauer spectroscopy (QMS) and quasielastic incoherent neutron scattering (QNS). Strong affinity exists between neighboring Fe and Si atoms in Fe_3Si, which has been confirmed by Mossbauer spectroscopy [52]. It was found that Si atoms share their 3s and 3p electrons with neighboring Fe atoms, thus filling the 3d states of the Fe atoms. Garba [61] also calculated the affinity of Fe_3Si, using a tight binding model, and showed that a stronger affinity exists between neighboring Fe and Si atoms

than between neighboring Fe and Fe atoms. Therefore, it is easier for Fe to occupy Fe sites than Si sites, when Fe atoms are diffusing in Fe_3Si. If Fe atoms only diffuse via A,C and B sites in stoichiometric Fe_3Si, the system structure and free energy will be unchanged.

In off-stoichiometric Fe_3Si, a fraction of the Fe atoms must occupy antisite positions on the D sublattice [71, 145]. The antistructure has a little lower density and a little higher vacancy concentration than the ordered structure [70,146]. Therefore, one might intuitively expect the antistructure to exhibit faster diffusion rates due to the higher vacancy concentration. Kikuchi and Sato [140, 147], however, have shown that in an antisite disordered structure, an atom that has jumped to the "wrong" sublattice does not return immediately to a "correct" position, thereby inhibiting migration over long distances. As the Fe concentration increases in Fe_3Si, the number of antisite positions increases which leads to a reduction in the diffusion coefficient. Diffusivities have been measured for stoichiometric and off-stoichiometric Fe_3Si [147]. At 720°C, the diffusivity for $Fe_{80}Si_{20}$ is a factor of 5-10 times lower than that for stoichiometric Fe_3Si.

One can conclude from the above arguments that not only is stoichiometric Fe_3Si thermodynamically the most stable form of Fe_3Si, but its growth is also kinetically preferred over off-stoichiometric Fe_3Si. As such, only stoichiometric Fe_3Si would be expected in Fe/Si couples. In the Fe/Fe_3Si couples, off-stoichiometric Fe_3Si forms at the interface, but grows more slowly as a result of slower diffusion rates through the antistructure.

3.3.2.7. Silicide Growth at 700°C in Bulk Diffusion Couples

The iron silicide sequence growth sequence in bulk diffusion couples, is shown schematically in Fig. 3-17. During initial stages of annealing of the bulk diffusion couple, Si atoms and Fe atoms can break their bonds forming a thin (~ few atoms thick) reaction region at the Fe/Si interface. The driving force for this process depends on the Gibbs free energy for silicide formation. The rate at which of Si and Fe atoms can break their bonds is given by the release rate r [141].

$$r = n^* \nu_0 \exp(-\frac{E}{kT}) \qquad (3\text{-}1)$$

where n* is the number density of reactant atoms per unit area of surface layer (atom cm^{-2}). E is binding energy (per N atom or molecule) of N atoms at surface (E_{Si} = 450 kJ/mol, E_{Fe} = 406 kJ/mol [156]. ν_0 *is* a vibration frequency. The ratio $\frac{r_{Fe}}{r_{Si}}$ is ~ 940 at 500°C, according to Eq.(3-1). It is therefore easier for Fe atoms to break their bonds than for Si

atoms. Therefore, the Fe concentration is initially significantly higher than that of Si. The first silicide phase to form would be the most Fe-rich phase Fe_3Si (Fig.3-17b). Once Fe forms, Fe is the major diffuser in Fe_3Si . As the Fe_3Si thickens, the Fe diffusion rate will continually decrease, which results in a decrease in Fe/Si ratio at the interface. At some point, the Fe/Si composition is such that FeSi formation is kinetically more favorable and FeSi starts to forms. (Fig. 3-17c) at the interface between Fe_3Si and Si. Si is the major diffuser in FeSi. FeSi grows into a continous layer. Fe_3Si continues to form. Extra Si nucleated on the FeSi and formed β-$FeSi_2$. Silicide sequence growth in bulk diffusion couples at 700°C is shown in Fig.3-17.

3.4. Conclusions

The work on alloys and bulk diffusion couples has led to the listed conclusions:

(1) The lattice parameter of Fe_3Si is slightly increased with increasing Fe concentration in off-stoichiometric Fe_3Si.

(2) According to Structure Factor calculations, off-stoichiometric Fe_3Si can be distinguished from stoichiometric Fe_3Si by electron diffraction.

(3) Fe_3Si is the first phase to form in the Fe/Si couples, followed by FeSi and then $FeSi_2$.

(4) In the Fe_3Si diffusion layer of Fe-Si diffusion couples, only stoichiometric Fe_3Si forms. These results are explained based on thermodynamic and kinetic arguments.

(5) Off-stoichiometric Fe_3Si forms in Fe_3Si-Fe couples. Fe diffusion in the off-stoichiometric Fe_3Si lattice is slower than in stoichiometric Fe_3Si.

(6) Fe is the major diffuser in Fe_3Si and Si is the major diffuser in FeSi.

(7) At 700°C, stoichiometric Fe_3Si is the most stable form of Fe_3Si.

(8) Fe_3Si, $FeSi_2$ and FeSi growth is proportional to $t^{1\ 2}$, i.e., diffusion-controlled.

Table 3-1 Alloy compositions.

EDS Spectrum	Alloy A (at%Si)	Alloy B (at%Si)	Alloy C (at%Si)
1	11.8	18.7	25.3
2	11.9	18.8	24.7
3	11.5	17.9	25.2
4	11.9	17.6	25.4
5	11.5	18.2	24.9
6	11.8	19.3	25.4
Average	11.8	18.6	25.3
Stand. Dev.	0.2	0.2	0.2

Table 3-2 Atom positions for stoichiometric Fe_3Si.

Atom#	x	y	z	Occupancy (%)	Element
1	0	0	0	100	Si
2	0	1/2	1/2	100	Si
3	1/2	0	1/2	100	Si
4	1/2	1/2	0	100	Si
5	1/2	1/2	1/2	100	Fe
6	1/2	0	0	100	Fe
7	0	1/2	0	100	Fe
8	0	0	1/2	100	Fe
9	1/4	1/4	1/4	100	Fe
10	1/4	3/4	3/4	100	Fe
11	3/4	1/4	3/4	100	Fe
12	3/4	3/4	1/4	100	Fe
13	3/4	3/4	3/4	100	Fe
14	3/4	1/4	1/4	100	Fe
15	1/4	3/4	1/4	100	Fe
16	1/4	1/4	3/4	100	Fe

Table 3-3 Atom positions for ordered off-stoichiometric Fe_3Si.

Atom#	x	y	z	Occupancy (%)	Element
1	0	0	0	100	Fe*
2	0	1/2	1/2	100	Si*
3	1/2	0	1/2	100	Fe*
4	1/2	1/2	0	100	Si *
5	1/2	1/2	1/2	100	Fe
6	1/2	0	0	100	Fe
7	0	1/2	0	100	Fe
8	0	0	1/2	100	Fe
9	1/4	1/4	1/4	100	Fe
10	1/4	3/4	3/4	100	Fe
11	3/4	1/4	3/4	100	Fe
12	3/4	3/4	1/4	100	Fe
13	3/4	3/4	3/4	100	Fe
14	3/4	1/4	1/4	100	Fe
15	1/4	3/4	1/4	100	Fe
16	1/4	1/4	3/4	100	Fe

- 1 or 2 Fe atoms replace 1 or 2 Si atoms in any one or two Si positions in the stoichiometric Fe_3Si lattice.

Table 3-4 Atom positions for random off-stoichiometric Fe_3Si.

Atom#	x	y	z	Occupancy (%)	Element
1	0	0	0	X*	Si
2	0	1/2	1/2	X*	Si
3	1/2	0	1/2	X*	Si
4	1/2	1/2	0	X*	Si
5	1/2	1/2	1/2	100	Fe
6	1/2	0	0	100	Fe
7	0	1/2	0	100	Fe
8	0	0	1/2	100	Fe
9	1/4	1/4	1/4	100	Fe
10	1/4	3/4	3/4	100	Fe
11	3/4	1/4	3/4	100	Fe
12	3/4	3/4	1/4	100	Fe
13	3/4	3/4	3/4	100	Fe
14	3/4	1/4	1/4	100	Fe
15	1/4	3/4	1/4	100	Fe
16	1/4	1/4	3/4	100	Fe
17	0	0	0	100-X	Fe
18	0	1/2	1/2	100-X	Fe
19	1/2	0	1/2	100-X	Fe
20	1/2	1/2	0	100-X	Fe

- X is Si occupancy, which ranges from 0-100%.

Table 3-5 Structure Factor calculations for Fe_3Si.

Reflection condition	Stoichiometric Fe_3Si	Random off-stoichiometric Fe_3Si	Ordered off-stoichiometric Fe_3Si ($1Fe \rightarrow 1Si$)	Ordered off-stoichiometric Fe_3Si ($2Fe \rightarrow 2Si$)
$h+k+l=4n^{*a}$				
h k l all even	$4(f_{Si}+3f_{Fe})$	$4[xf_{Si}+(1-x)f_{Fe}]$	$3f_{Si}+13f_{Fe}$	$2f_{Si}+14f_{Fe}$
hkl; 2 odd 1 even	0	0	$f_{Fe}-f_{Si}$	$2f_{Fe}-2f_{Si}$
$h+k+l=2n^{*b}$	$4f_{Si}-4f_{Fe}$	$4[xf_{Si}-(1-x)f_{Fe}]$	$2f_{Si}-2f_{Fe}$	$2f_{Si}-2f_{Fe}$
hkl; 2odd 1 even	0	0	$f_{Fe}-f_{Si}$	$2f_{Si}-2f_{Fe}$
$h+k+l=n^{*b}$	$4f_{Si}-4f_{Fe}$	$4[xf_{Si}-(1-x)f_{Fe}]$	$3f_{Si}-3f_{Fe}$	$2f_{Fe}-2f_{Si}$
hkl all odd	0	0	$f_{Fe}-f_{Si}$	$2f_{Fe}-2f_{Si}$

[a] n* = 0,1, 2,... [b] n* = 1,3,5...

Table 3-6 Allowed Reflections for Fe_3Si Based on Structure Factor Calculations*.

h k l	d-spacing (nm) stoichiometric Fe_3Si	d-spacing* (nm) random off-stoichiometric Fe_3Si	d-spacing (nm) ordered off-stoichiometric $Fe_3Si(1Fe \rightarrow 1Si)$	d-spacing* (nm) ordered off-stoichiometric $Fe_3Si(2Fe \rightarrow 2Si)$
100			0.566	0.566
110			0.400	0.400
111	0.327	0.327	0.327	0.327
200	0.283	0.283	0.283	0.283
210			0.253	0.253
211			0.231	0.231
220	0.200	0.200	0.200	0.200
221			0.187	0.187
300			0.187	0.187
310			0.179	0.179
311	0.171	0.171	0.171	0.171
222	0.163	0.163	0.163	0.163
320			0.157	0.157
321	0.151	0.151	0.151	0.151

* Calculations were done assuming the stoichiometric Fe_3Si lattice parameter.

Table 3-7 D-spacings for alloys and Fe_3Si.

	d-spacing (nm)						
	$Fe_{88}Si_{12}$		$Fe_{82}Si_{18}$		$Fe_{75}Si_{25}$		
h k l	Fe_3Si SAD	Fe_3Si[1] XRD	Fe_3Si SAD	Fe_3Si[2] XRD	Fe_3Si SAD	Fe_3Si[3] XRD	Fe_3Si*
200	0.2880	0.2870	0.2850	0.2856			0.2830
210			0.2552	0.2557			
220			0.2011	0.2020	0.2000	0.2000	0.2000
311			0.1718	0.1723			0.1706
331			0.1303	0.1311			0.1298
400	0.1440	0.1435	0.1425	0.1428			0.1415
420	0.1307	0.1284	0.1276	0.1279			0.1266
422	0.1177	0.1172	0.1160	0.1166			0.1155
440			0.1005	0.1010	0.4000	0.4000	0.4000
620			0.0884	0.0903			0.0853

[1] a = 0.5742 nm; [2] a = 0.5713 nm; [3] * a = 0.5657 nm

Table 3-8 Fe/Si Bulk diffusion couples produced.

Temperature (°C)	Annealing Time (hours:minutes)
600°C	739:00 961:25 1132:25 1653:50
637°C	709:36 711:30 1065:30 1517:25
666°C	234:10 504:00 721:00 1011:00
700°C	234:30 410:00 485:30 600:00 718:30 836:30 1007

Table 3-9 Phases observed in bulk diffusion couples.

Si	Virtually pure
Phases	ideal composition (atomic)
β-$FeSi_2$	33% Fe and 67% Si
FeSi	50% Fe and 50% Si
Fe_3Si	75% Fe and 25 % Si
α-Fe	Solid solution with < 10 % Si

Table 3-10 x_{min}, y_{min} and $F_k - U_k^o$ with respect to C_{Si} at 700°C.

C_{Si} (at%)	x_{min}	y_{min}	$F_k - U_k^o$ (kJ/g-atom)
0.25	0.25	0.5	-37.26
0.23	0.156	0.386	-30.65
0.20	0.133	0.333	-27.13
0.18	0.096	0.276	-25.73
0.15	0.086	0.236	-22.75
0.12	0.07	0.19	-19.25

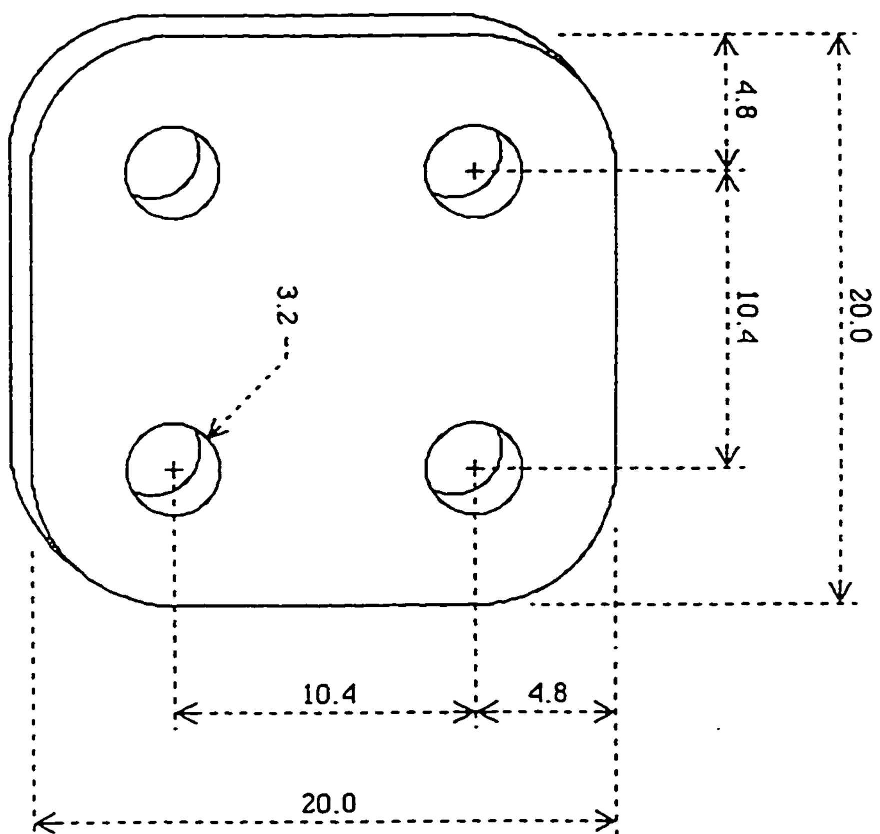

Fig.3-1 Diagram of steel clamping plate for bulk diffusion couples. Dimensions are in mm [142].

a

b

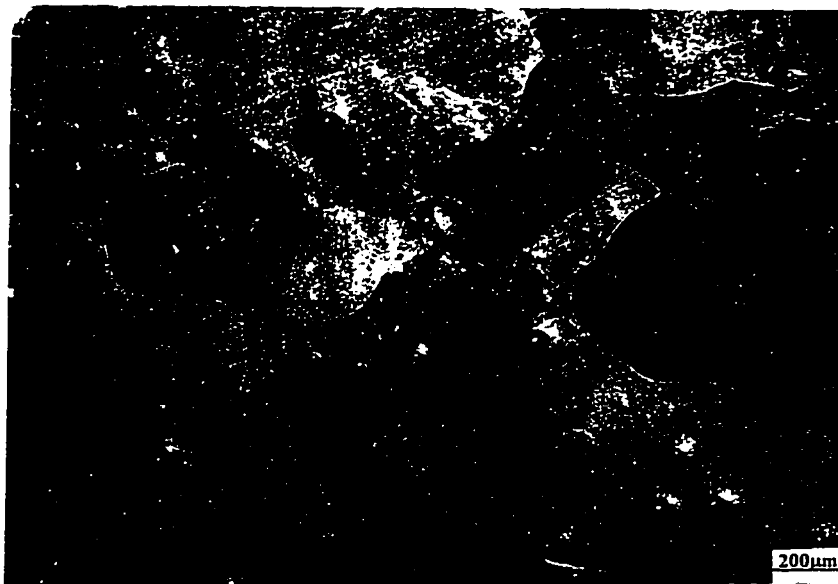

Fig.3-2 SEM micrographs of a) Alloy B and b) Alloy C.

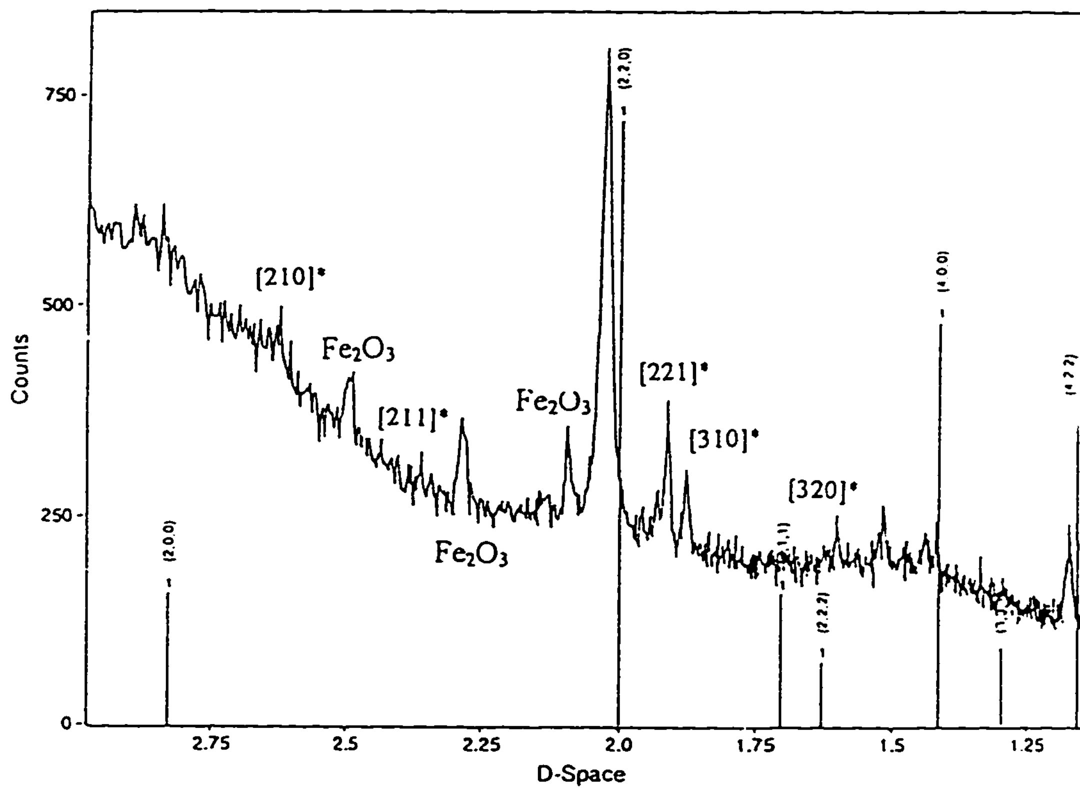

1>Gupeiite-Fe_3Si *off stoichiometric Fe_3Si

Fig.3-3a XRD spectrum for Alloy A.

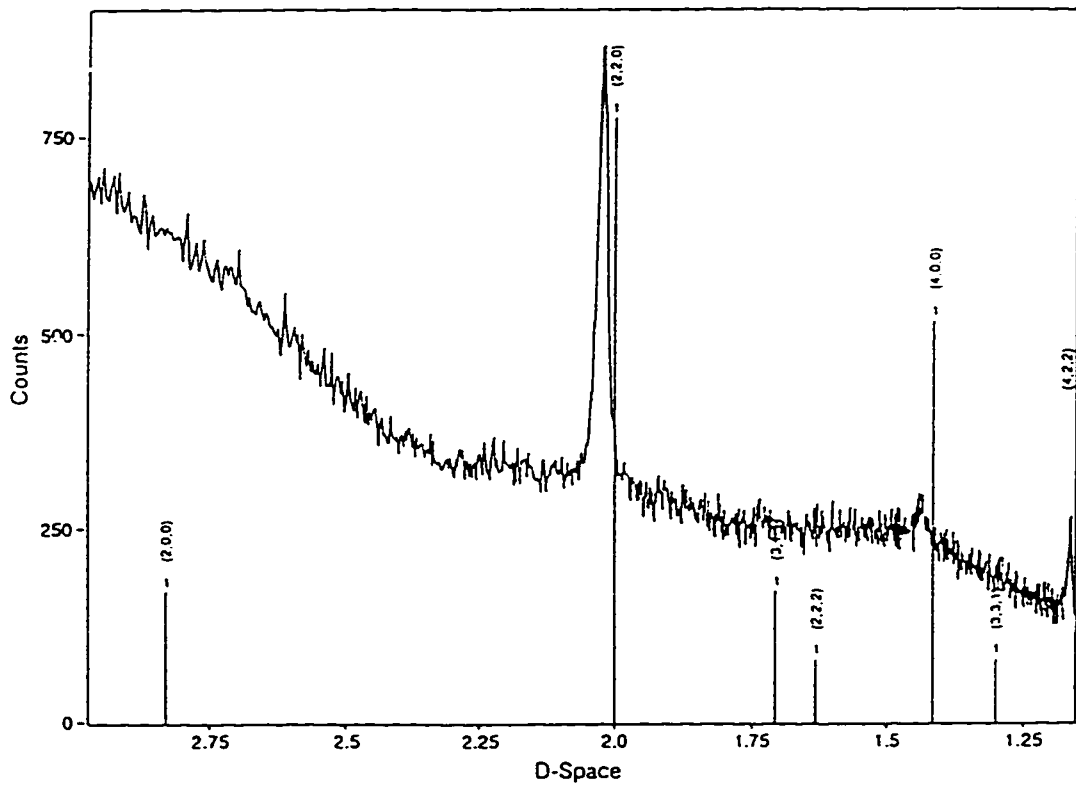

1>Gupeiite-Fe_3Si

Fig.3-3b XRD spectrum for Alloy B.

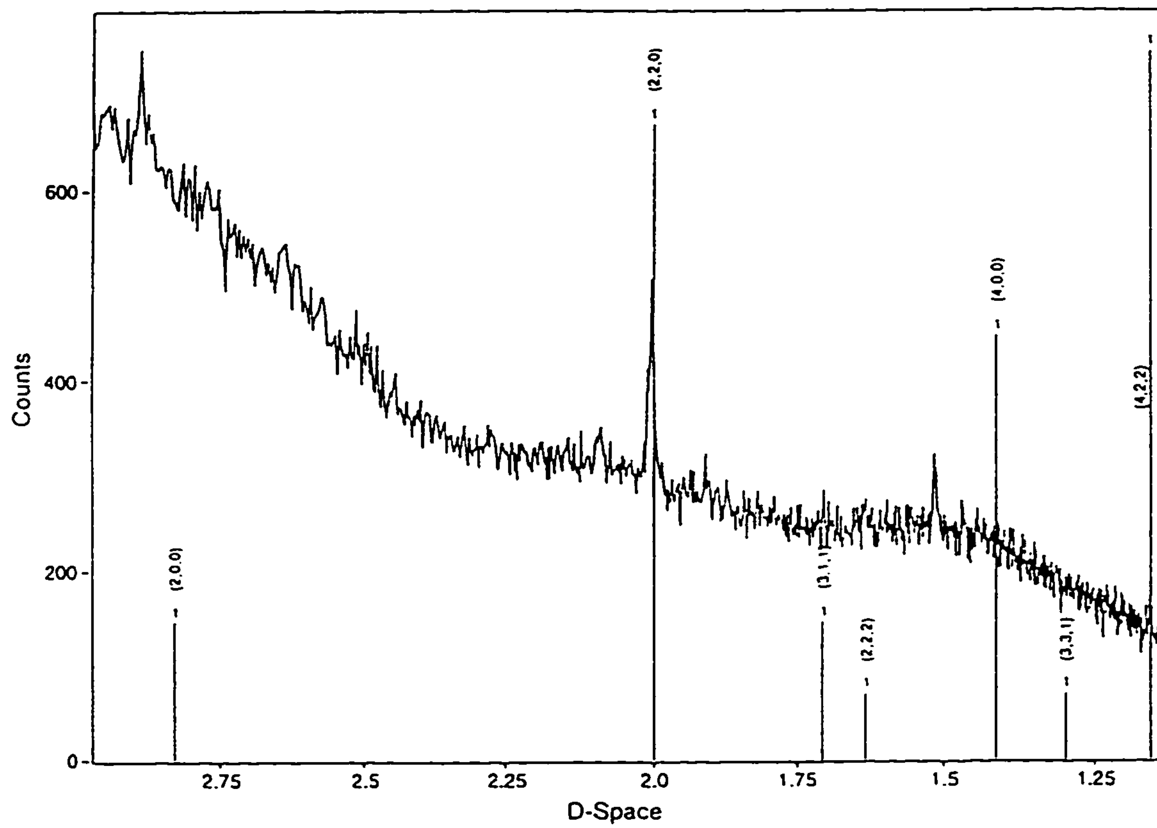

1>Gupeiite-Fe_3Si

Fig.3-3c XRD spectrum for Alloy C.

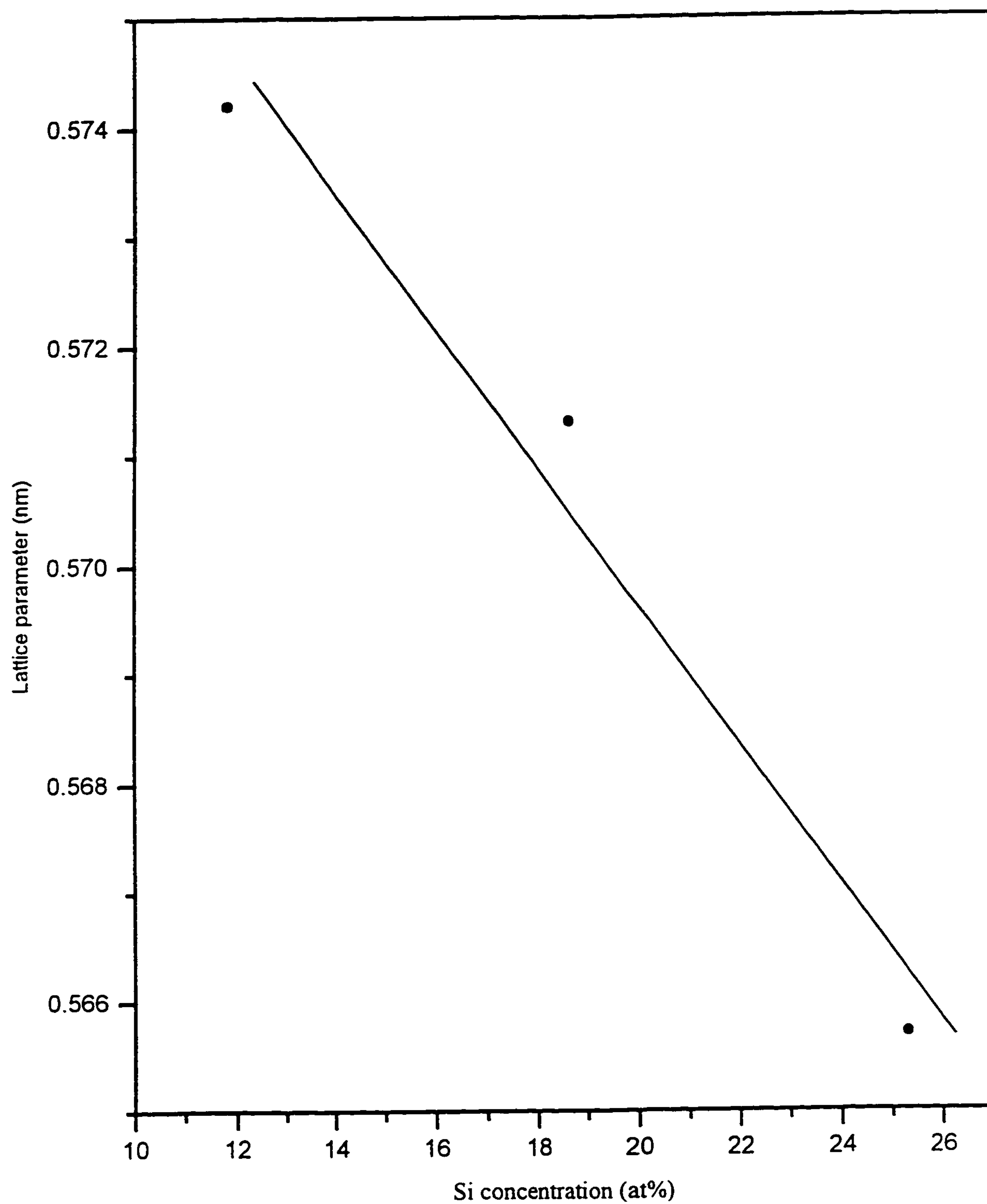

Fig.3-4 Lattice parameter vs. Si concentration in Fe_3Si.

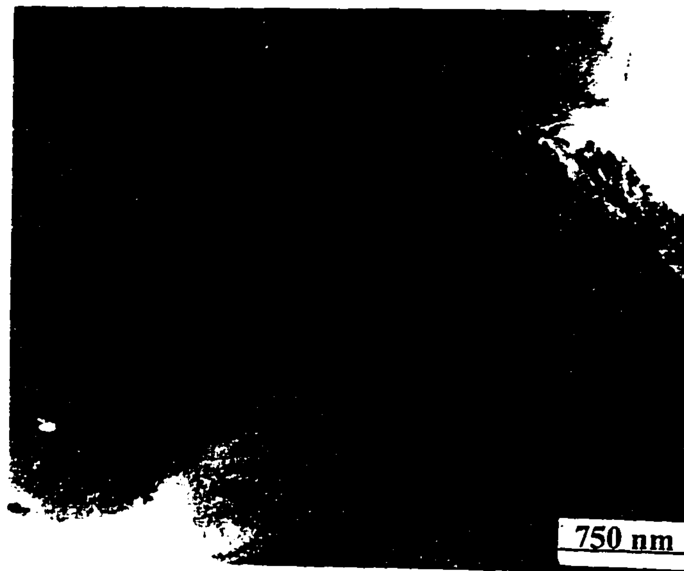

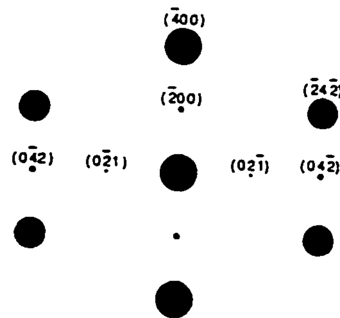

Fig.3-5a Bright field micrograph and SAD pattern for Alloy A

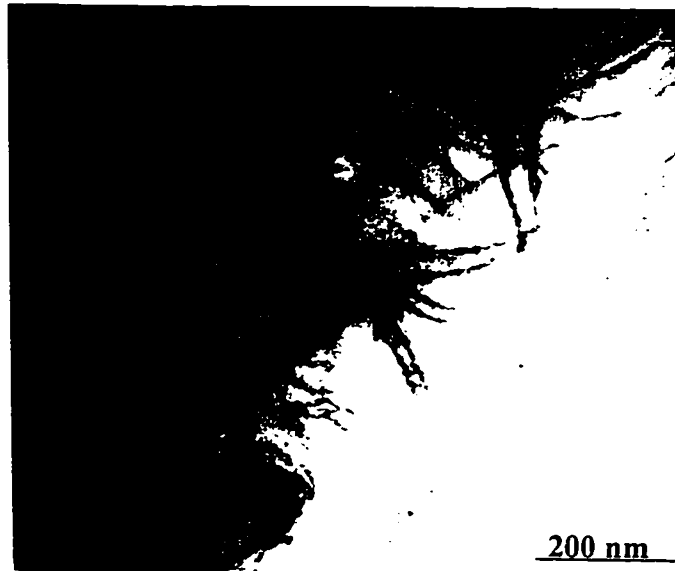

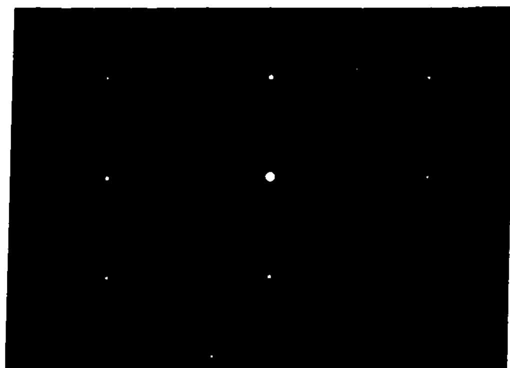

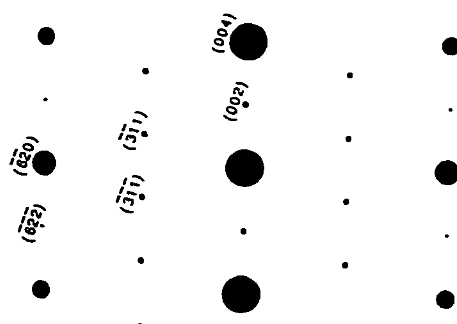

Fig.3-6b Bright field micrograph and SAD pattern for Alloy B.

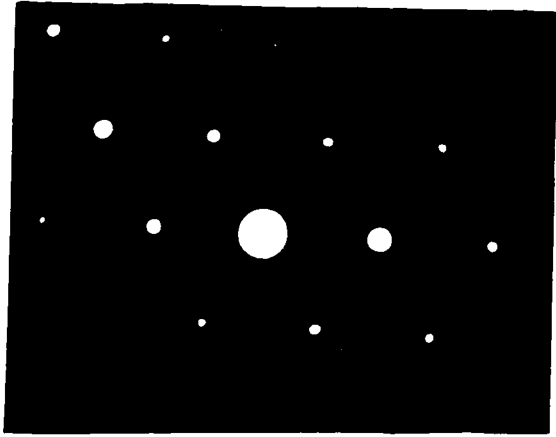

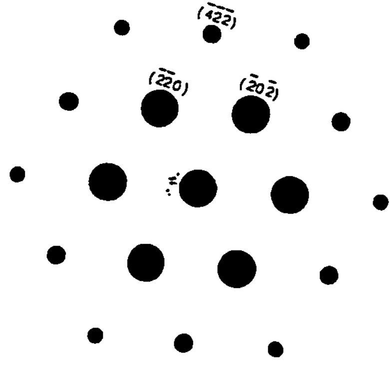

Fig. 3-5c Bright field micrograph and SAD pattern for Alloy C.

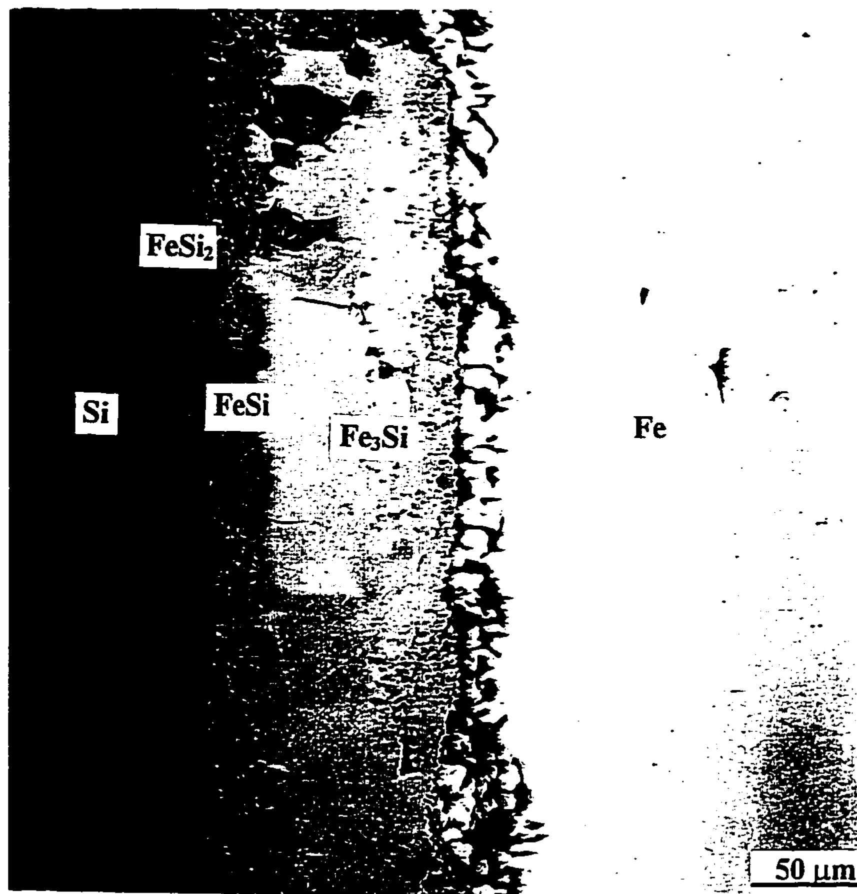

Fig. 3-6 SEM backscattered electron image of a Fe/Si bulk couple annealed at 666°C for 721 hrs.

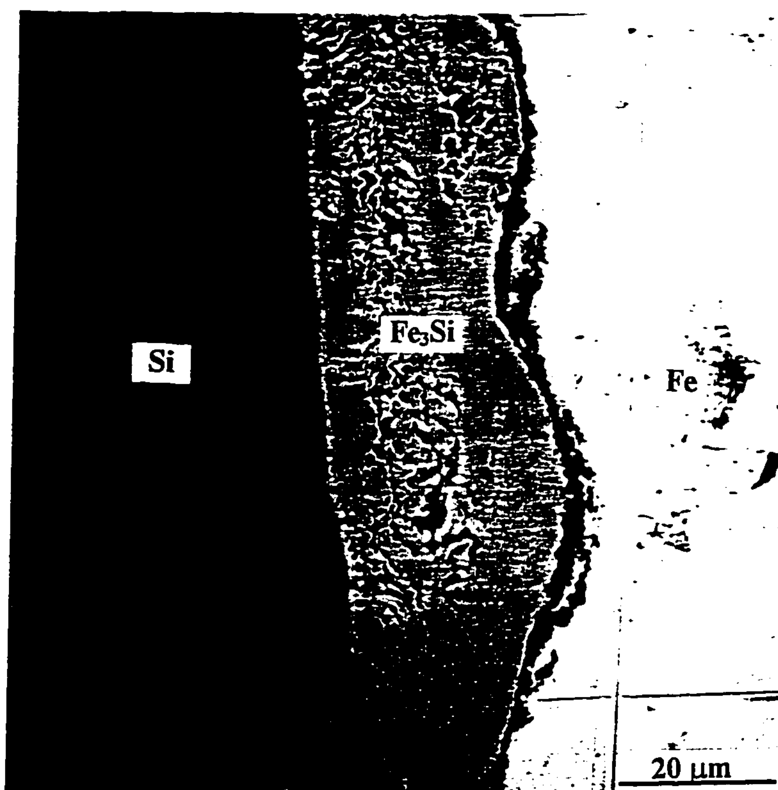

Fig.3-7a SEM backscattered electron image of a Fe/Si bulk couple annealed at 700°C for 7 hrs.

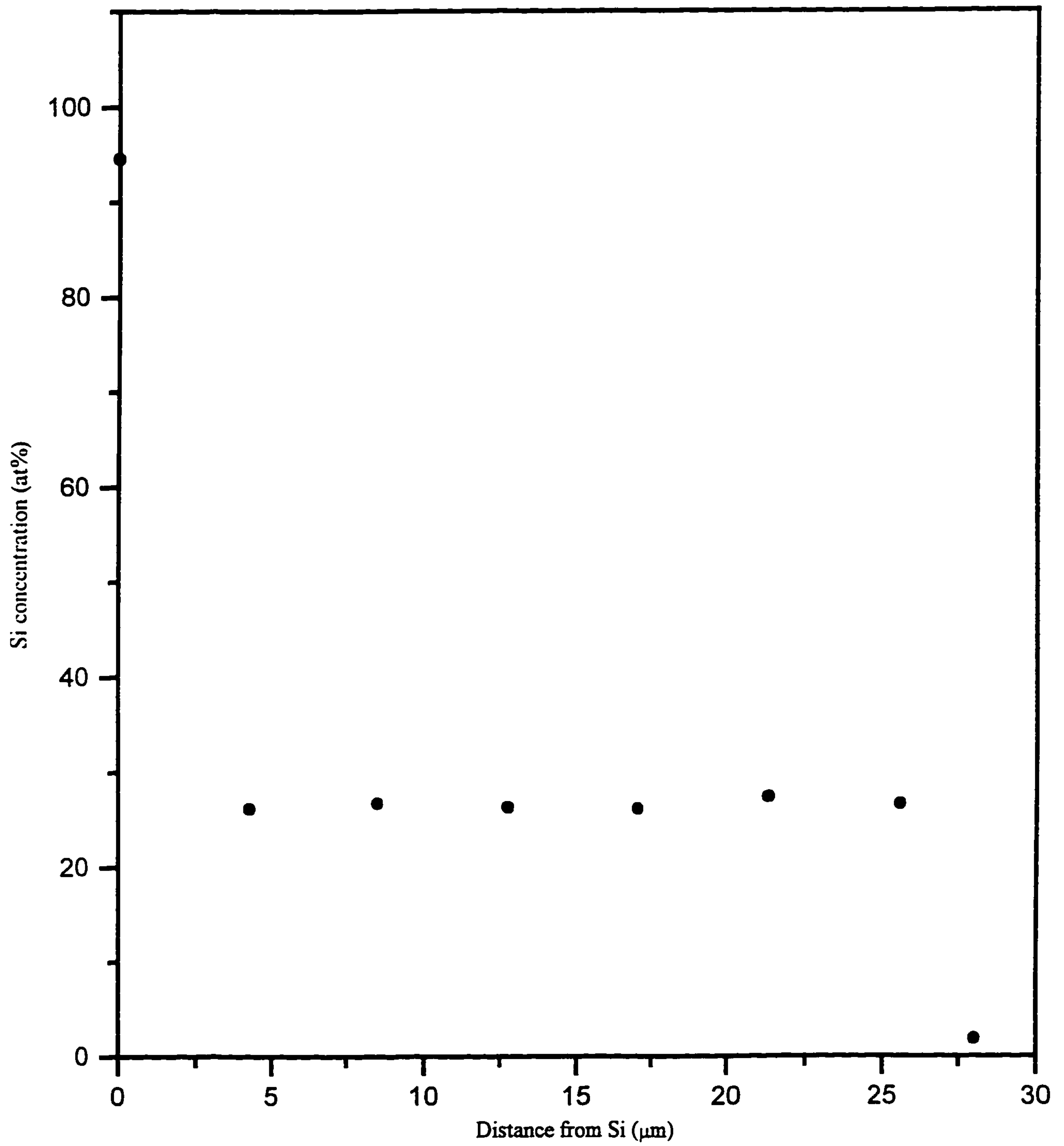

Figure 3-7b Concentration profile of the couple in (a).

Fig.3-8 SEM backscattered electron image of a Fe/Si bulk couple annealed at 700°C for 1007 hrs.

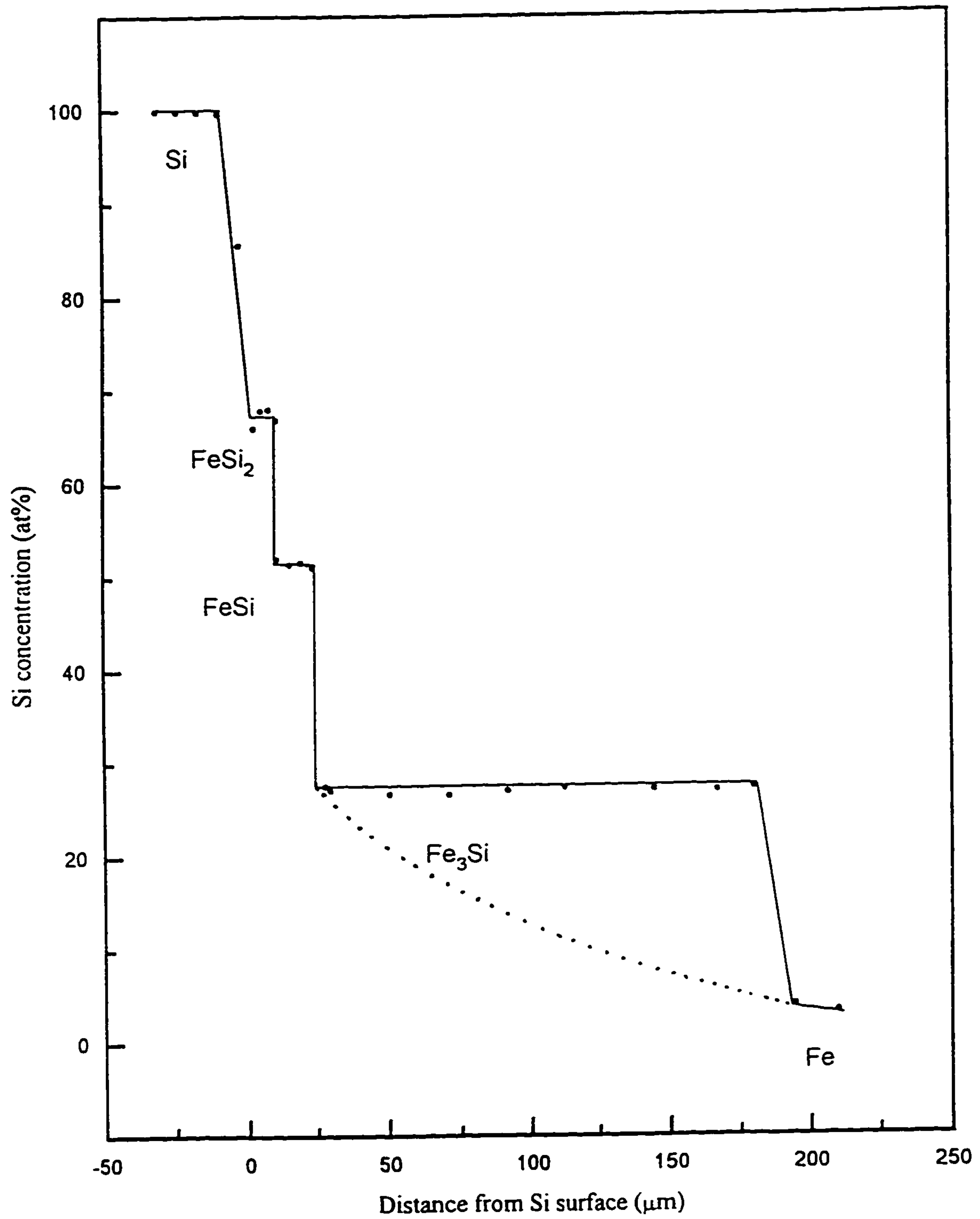

Fig.3-8b Concentration profile for the couple in (a)

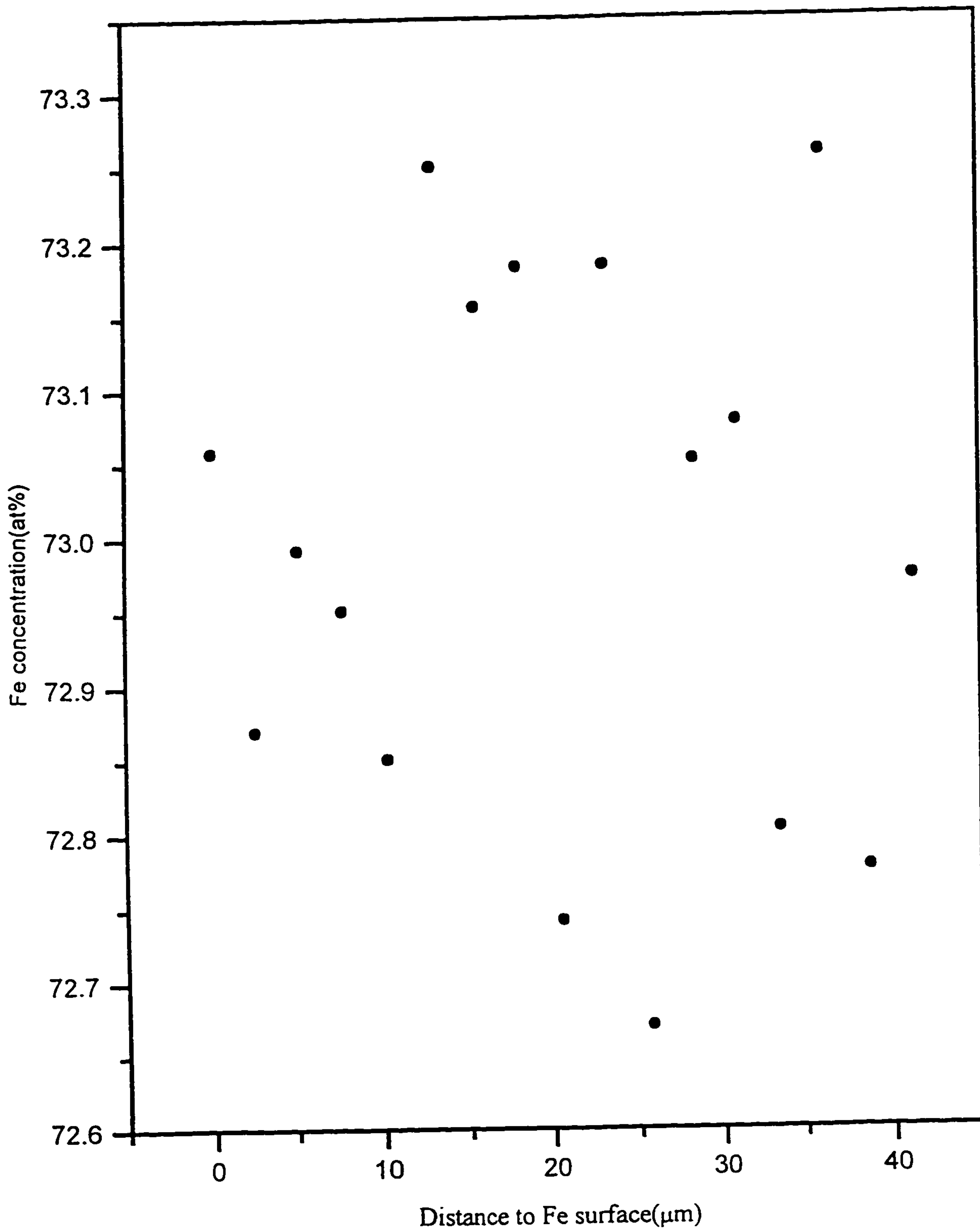

Fig.3-9 Concentration profile from Fe_3Si layer on Fe/Si couple annealed at 700°C for 600 hrs

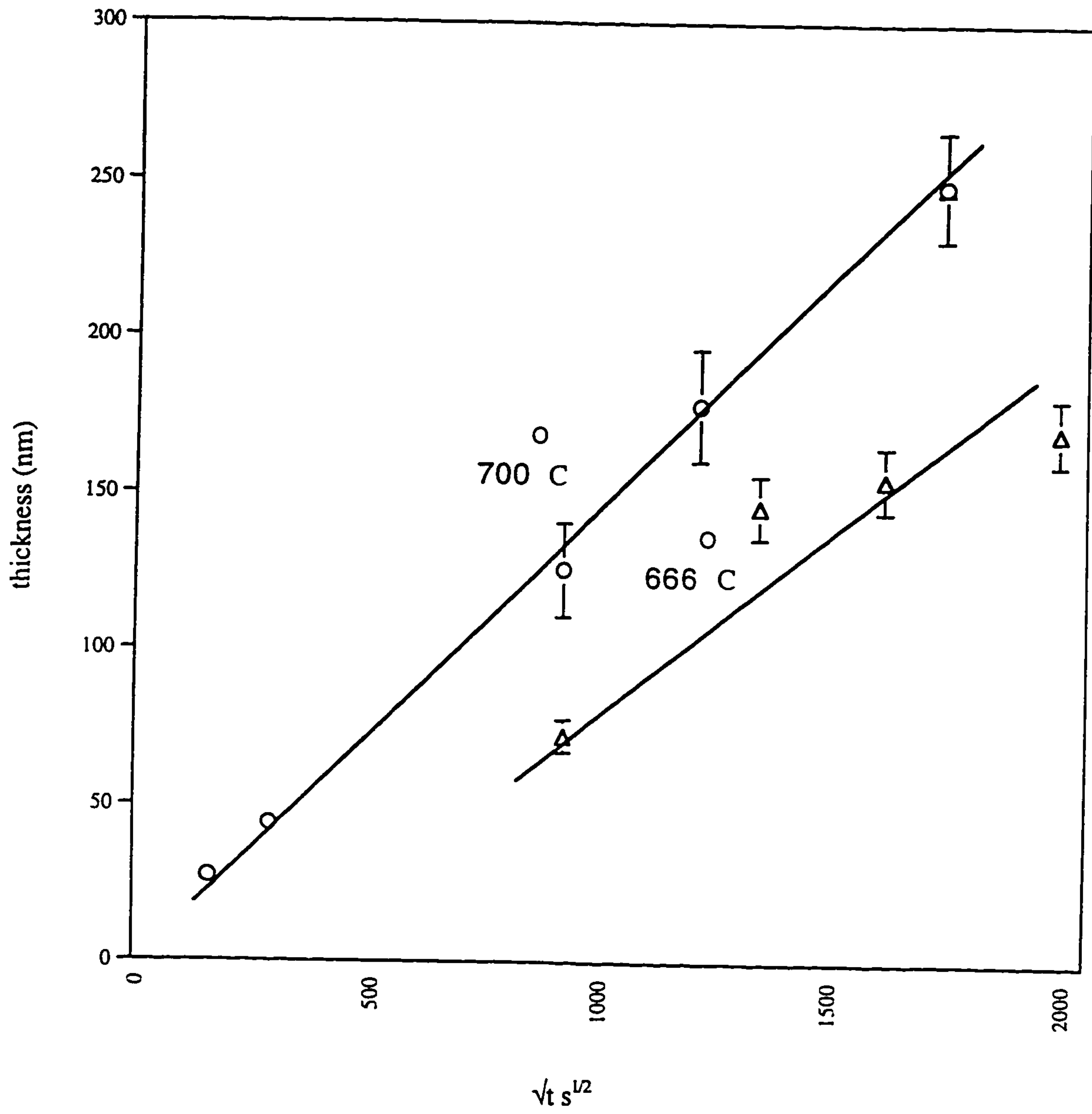

Fig.3-10 The thickness of Fe_3Si as a function of annealing time. Error bars represent one standard deviation (±) in the thickness measurment.

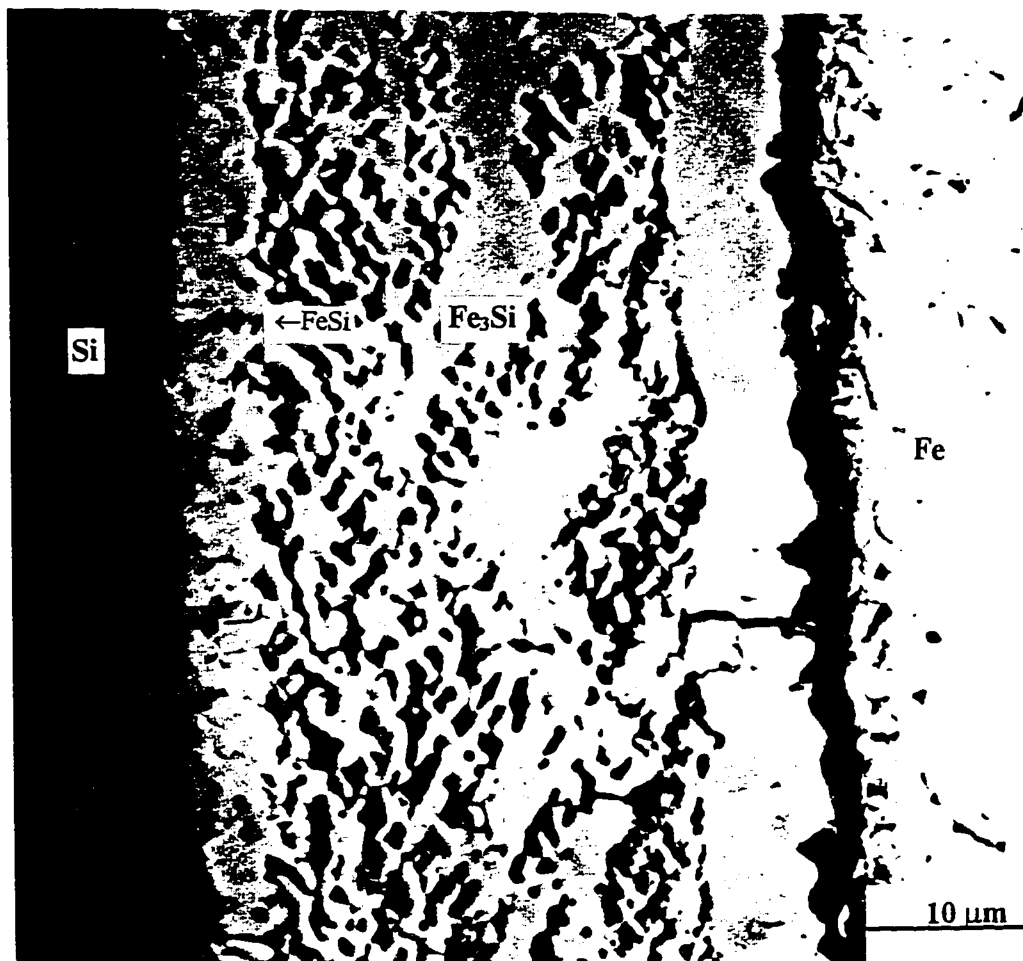

Fig.3-11 SEM backscattered electron image of a couple annealed at 700°C for 23 hrs.

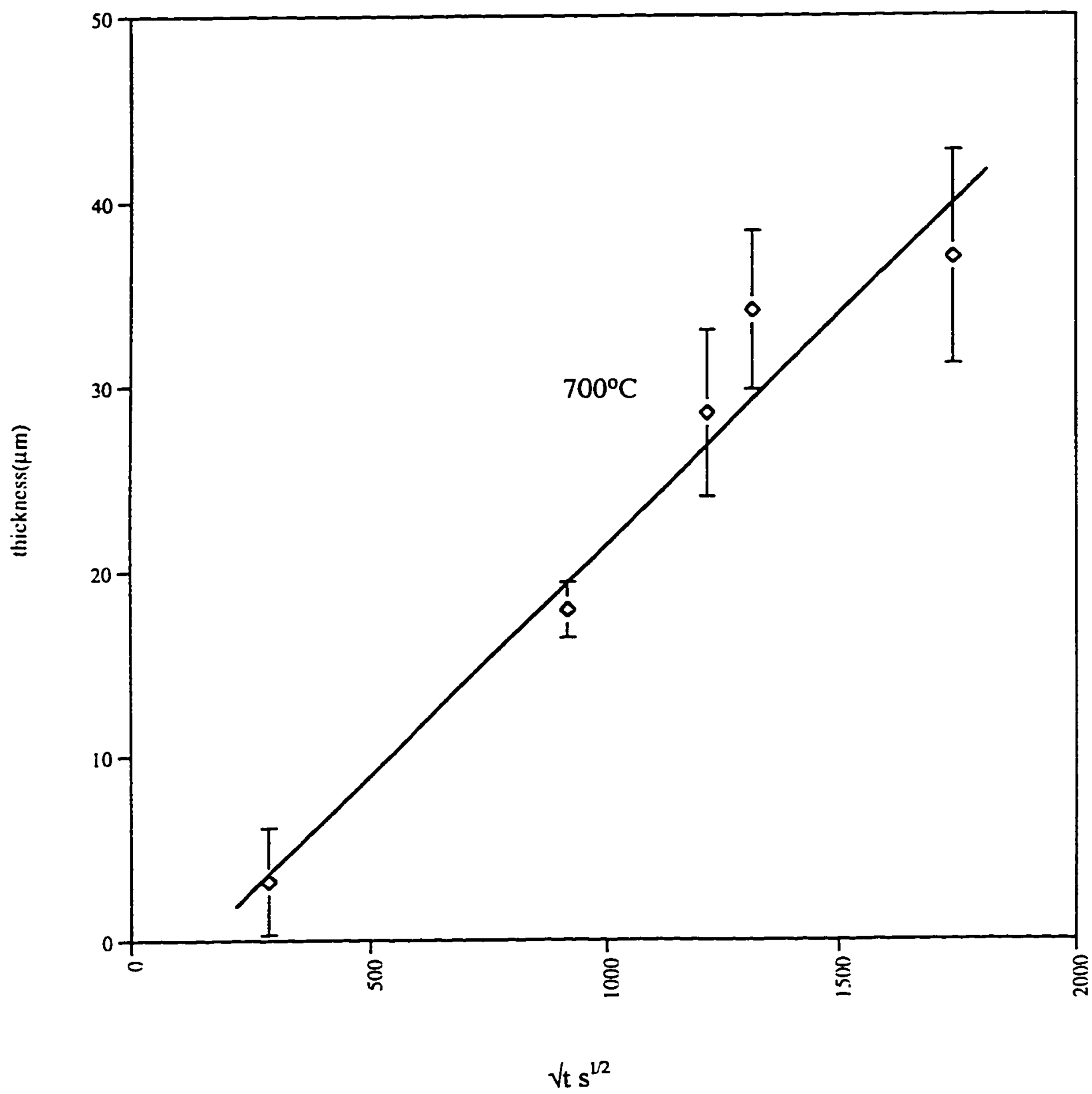

Fig.3-12 FeSi thickness as a function of annealing time. Error bars represent one standard deviation (±) in thickness measurment.

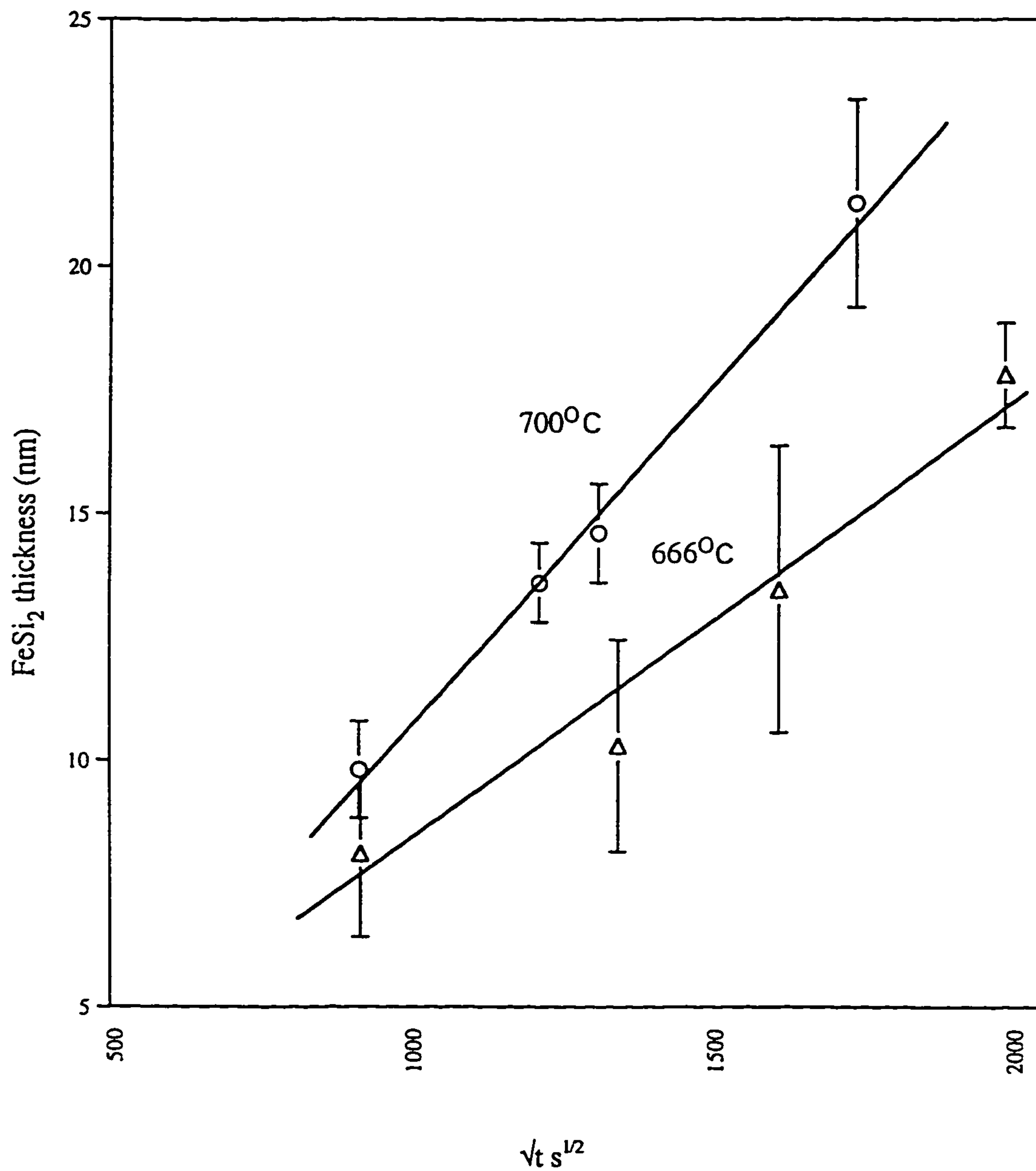

Fig.3-13 $FeSi_2$ thickness as a function of annealing time. Error bars represent one standard deviation (±) in the thickness measurment.

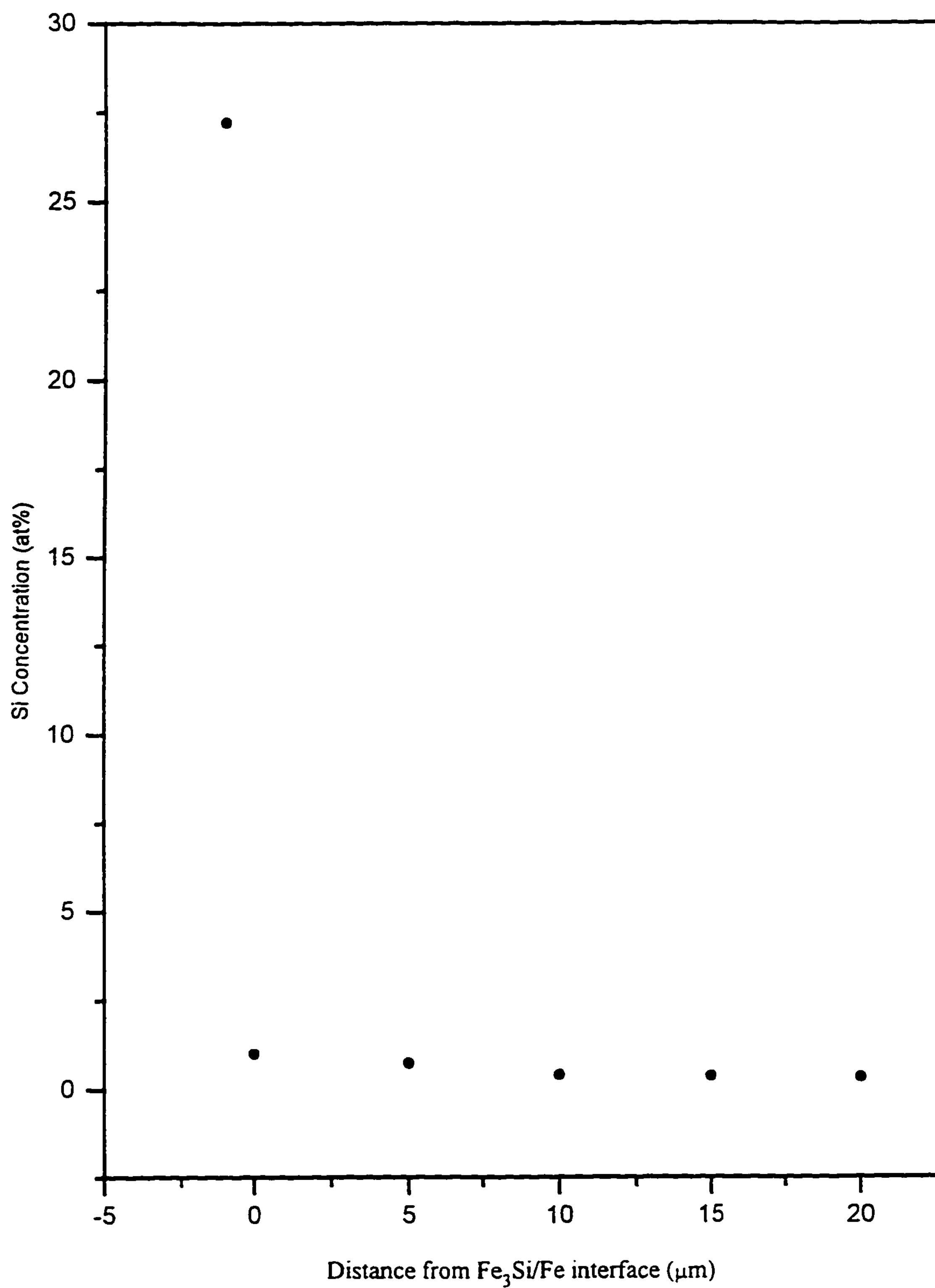

Fig.3-14 Concentration profile for the Fe_3Si/Fe interfacial region for the couple annealed at 700°C for 23 hrs

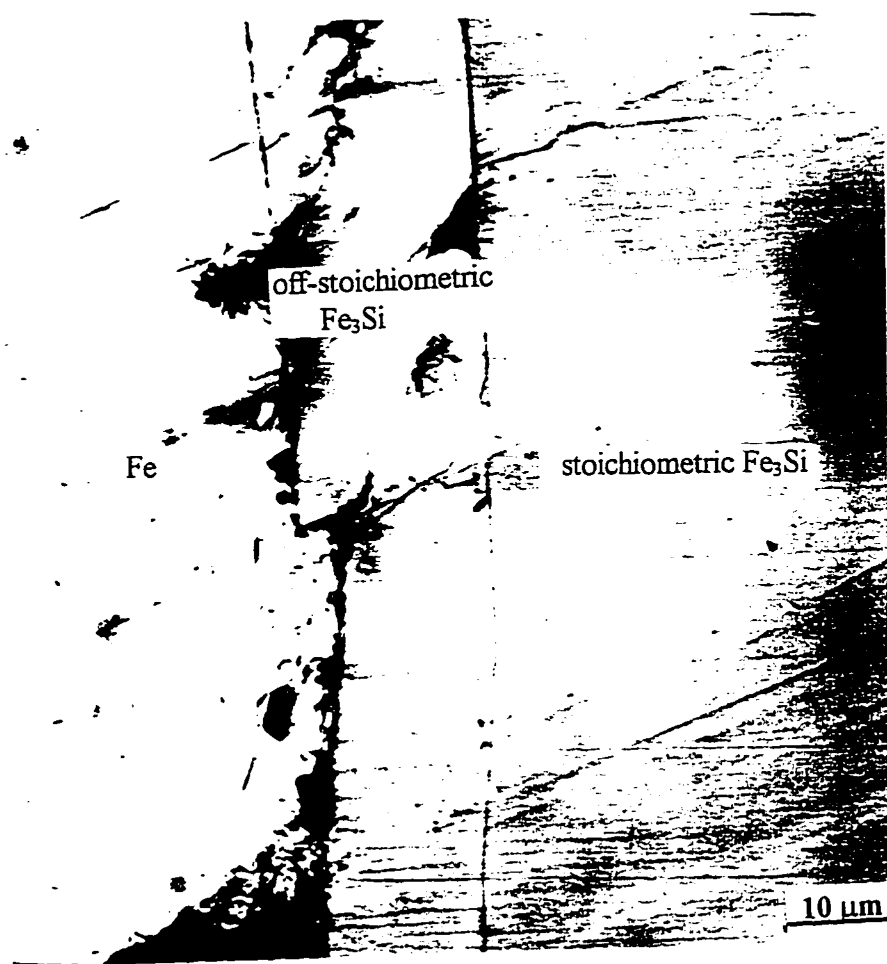

Fig.3-15a SEM backscattered electron image of diffusion zone of Fe_3Si/Fe couple annealed at 700°C for 120 hrs.

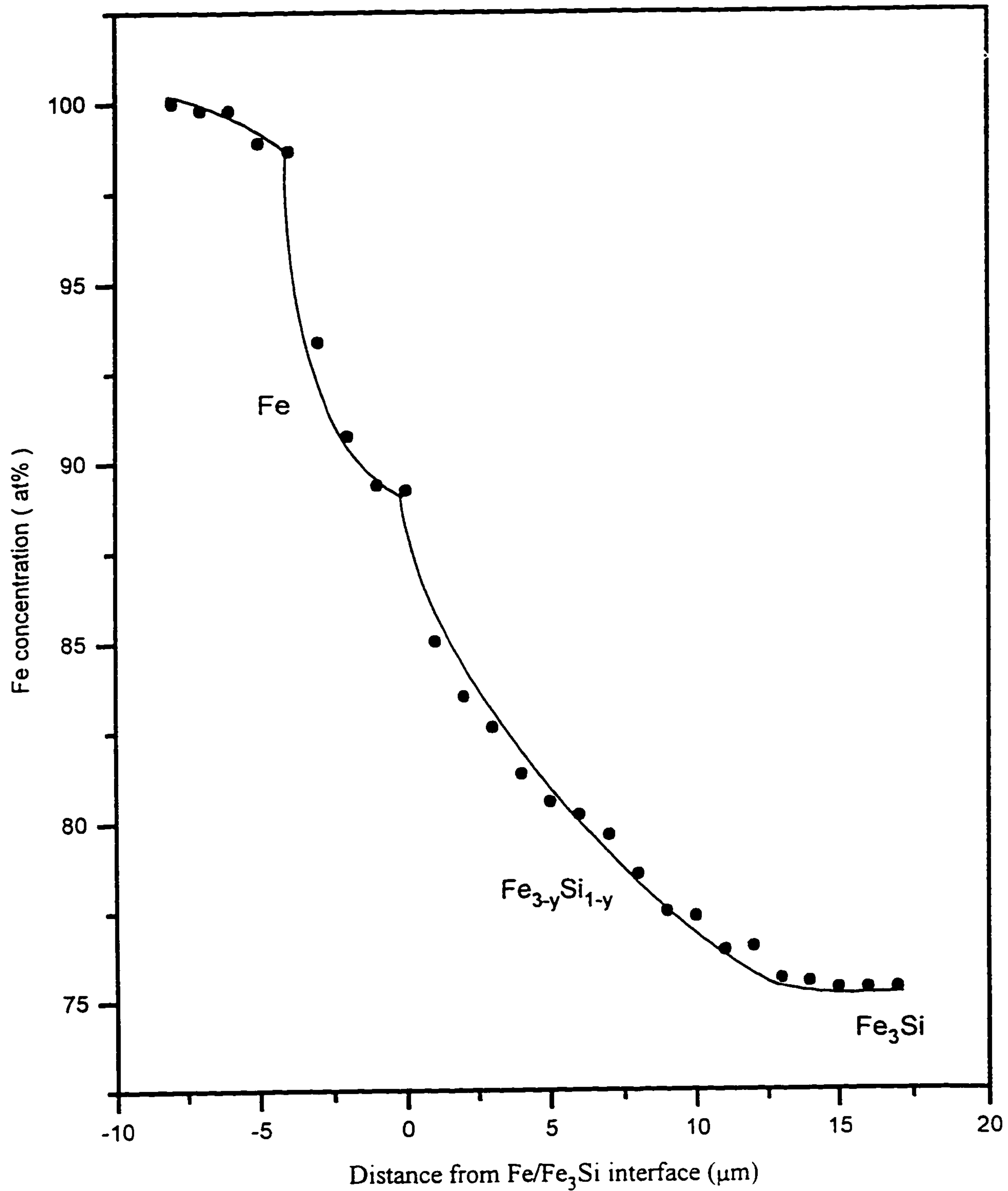

Fig.3-15b Concentration profile for the couple in (a)

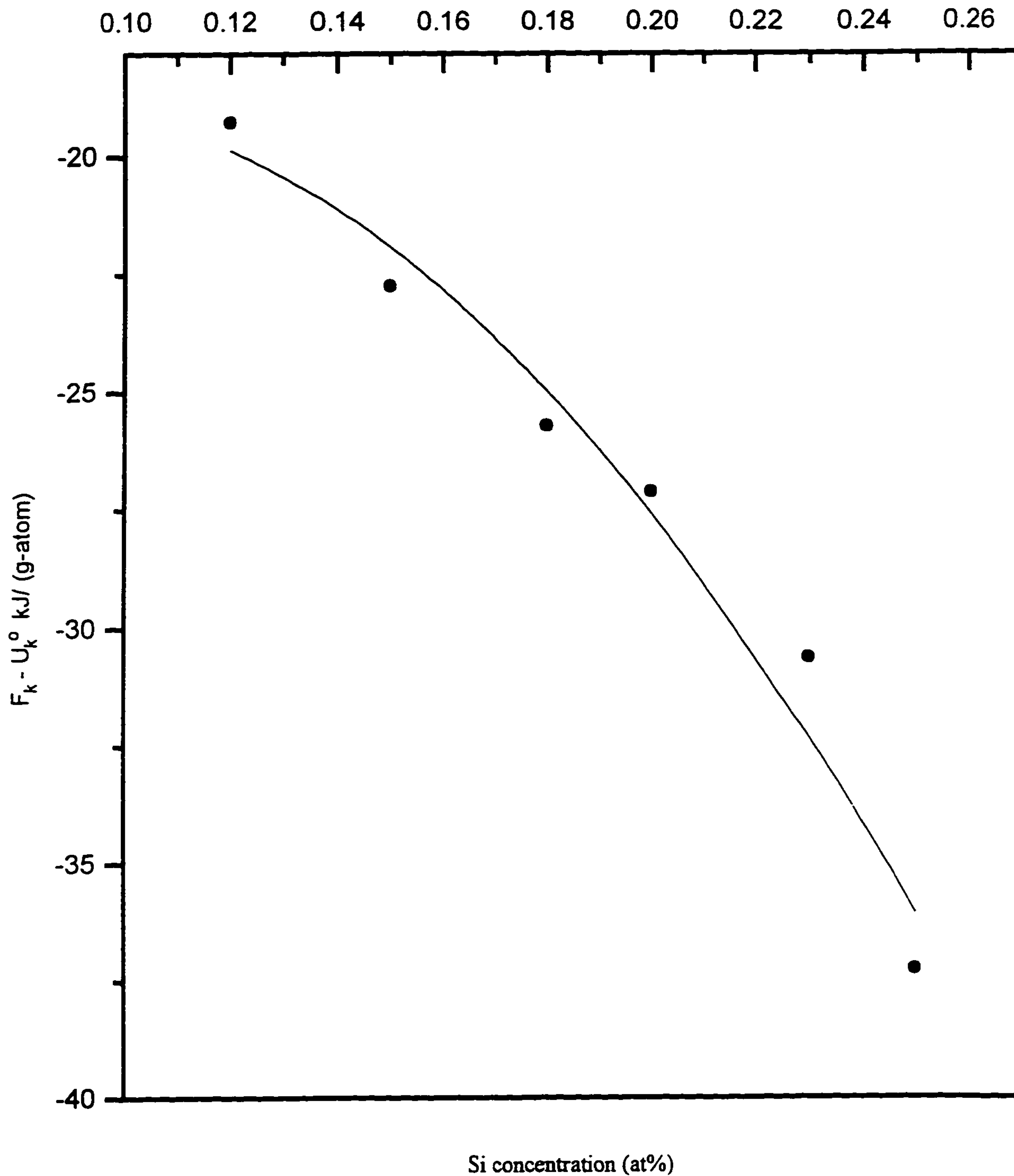

Fig.3-16 Plot of the difference between the configurational free energy term (F_k) and the internal energy term (U_k), which is not a function of the order parameter, vs Si atom fraction at 700°C. The dark spots are calculation results and the curve is fitted by exponential decay.

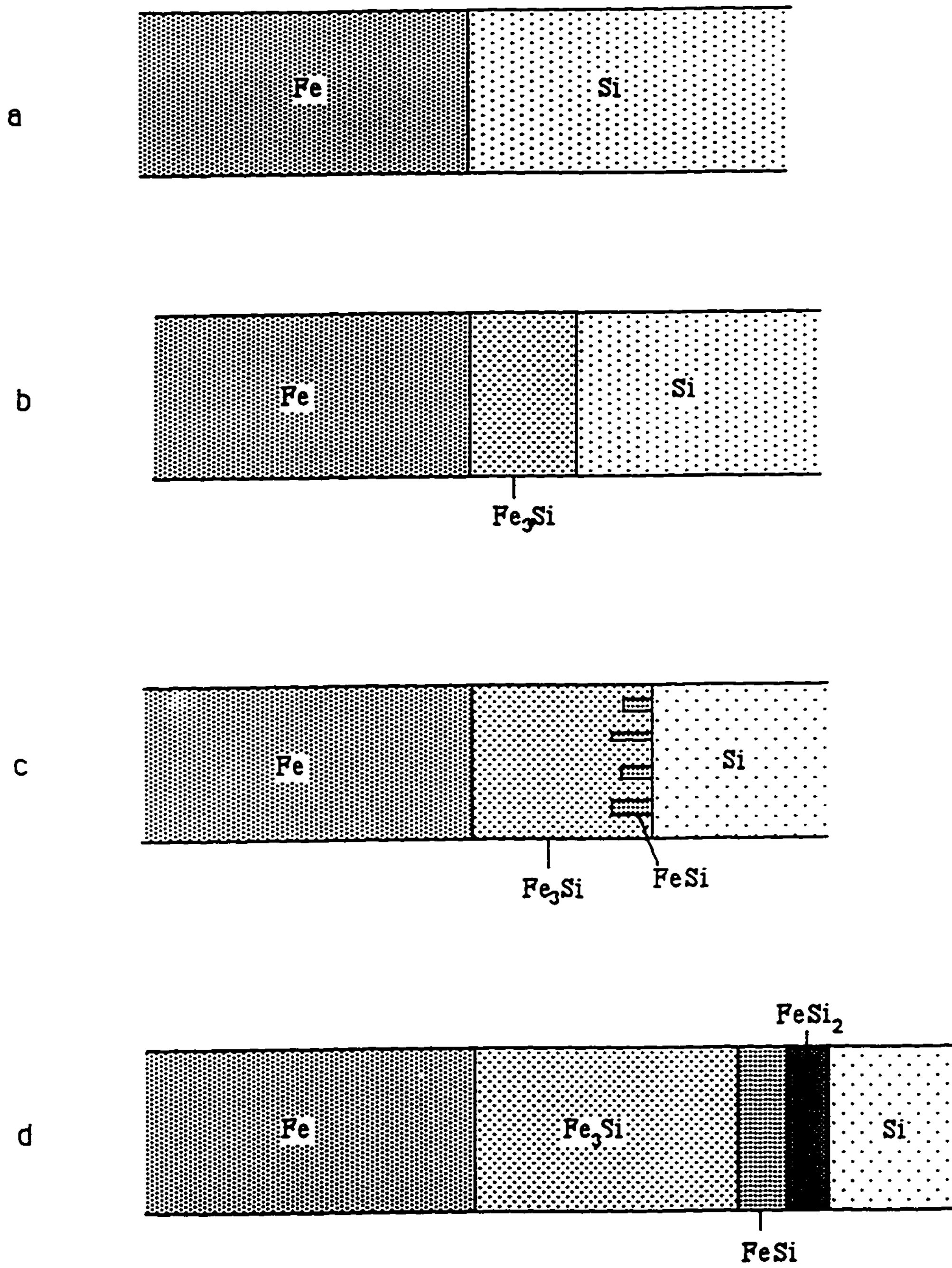

Fig.3-17 Silicide sequence growth in diffusion couple at 700°C.

Chapter 4. Thin Film Diffusion Couples

4.1. *Experimental Methods*

4.1.1. *Deposition of Iron*

Iron films were deposited onto Si (111) oriented wafers by electron beam evaporation. The Si (111) wafers were doped with boron to a resistivity of 1.0-10.0 Ω·cm. The Fe target had a purity of 99.95% Fe, and had been recently degassed. Deposition was done in a vacuum chamber. In the same chamber, a protective capping film of SiO_2 was immediately evaporated on top of the Fe. The capping layer has been found to be necessary to prevent oxidation and agglomeration of the Fe film during ex situ annealing [148]. Base pressures were ~ 4×10^{-8} torr, and deposition pressures were ~ 3×10^{-6} torr for the Fe and ~ 5×10^{-7} torr for the SiO_2. The Fe was deposited at a rate of ~1.7 nm/s and the SiO_2 at a rate of ~ 0.2 nm/s. Film thicknesses were monitored during deposition by a quartz thickness monitor, but were more accurately determined later by cross-sectional TEM. The Fe layer was found to be ~162 nm thick; the SiO_2 was ~100 nm thick.

Two deposited wafers were prepared. One was cut into pieces, each piece measuring 4.5 mm by 1.5 mm, with a computer-controlled diamond saw for TEM cross-section construction. The other one was left unsawn and an ultrasonic disc cutter was used to cut discs for TEM plan view specimens

4.1.2. *Annealing*

Iron silicide formation was achieved during anneals within a small quartz furnace. The furnace temperature was monitored and controlled by an electronic controller. During each anneal, only enough material was placed in the furnace to make a single TEM sample. The furnace was continuously flushed with N_2 (99.7% pure). The sample pieces were placed on the furnace stage with the film side up to avoid contamination from the stage surface. The furnace temperature was monitored and controlled by an electronic controller. Ramp up (45-90s) and ramp down (3 minutes) times from the preset temperature were not included in the annealing time.

4.1.3. *TEM Sample Preparation*

Both plan view and cross section TEM specimens were prepared using ion-milling techniques reported in the literature [149, 150]. The procedure for plan view specimen preparation included the following steps:

1. 3mm discs were cut from wafers with an ultrasonic cutter.
2. Discs were polished from the Si side down to a thickness of less than 200 μm with SiC abrasive paper. Samples were mounted on a small steel stage, which sits in the center of a flat steel grinding jig.
3. The discs were dimpled, using a Gatan Dimple Grinder from the Si side to a central thickness about 10 μm. Final polishing was then done to produce a very small hole and a mirror-like surface.
4. Final thinning was done by ion milling in a Gatan Duo Mill 600 CTMP. One or two Ar^+ ion guns were employed to sputter the sample at an angle of 13° to the horizontal, with an accelerating voltage of 3-4 kV; the ion gun current varied from 0.4 to 0.5 mA. The sputtering process depended on the location and thickness of the layer to be studied.

The procedure for cross section preparation was as follows [142, 151]:

1. The two rectangular pieces (4.5 mm x 1.5 mm) of annealed wafer material were glued together with silver epoxy, so that the film surfaces faced each other as shown in Fig.4-1. Other pieces of plain silicon were held together tightly in a small screw tightened press, which was put into a furnace and heated at 100°C for one hour to cure the epoxy.
2. After curing the epoxy, the sample was polished with 600 grit SiC abrasive paper on both sides, so that the two sides were parallel and the sample thickness was approximately 400 μm. A 3 mm diameter disc was cut from the material. The disc was further ground down to a thickness of less than 200 μm.
3. Using a Gatan Dimple Grinder, one side of the disc was polished with a polishing wheel to produce a highly reflective surface. The other side was ground to a thickness about 40 μm, then polished to transparency.
4. The sample was ion milled using a Gatan Duo Mill 600 CTMP. The sample was kept cold with liquid nitrogen at a base pressure of $<10^{-6}$ torr. Two $Ar+$ ion guns were employed to sputter the sample with the same angle as the plan view sample sputtering process. A 4 kV accelerating voltage and 0.5 mA ion gun current were employed for 45 min to 1hour depending on the location and thickness of layer to be studied. A 2.5 kV accelerating voltage and 0.2 mA ion gun current for 20 minutes were used as a final step to minimize defects, generated by relatively high accelerating voltage.

4.1.4. *Characterization*

TEM cross-sectional and plan view samples were examined in the two microscopes discussed previously - a Hitachi H-7000 and a JEOL 2010. SAD and EDS were used together to identify phases that formed at the Fe/Si interface. Commercial software, i.e., Virtual Laboratories Diffract 1.5B Diffract version 1.5b, was used to simulate and solve the diffraction patterns.

Ring and spot SAD patterns were observed with the H-7000 TEM. The Si substrate served as an internal calibration standard. The JEOL microscope, which is fitted with EDS equipment (a Ge ultrathin window x-ray detector), was used to check the composition of silicide layers in the cross-sectional samples. Actual atomic concentration (C) ratios of Fe:Si were calculated by determining the Cliff-Lorimer factor (k) (Eq.(2-3)) from a pure FeSi standard and multiplying this factor by the x-ray intensity (I) ratios of the two elements.

4.2. *Results and Discussion*

4.2.1. *Interfacial Oxide and Interfacial Reaction at Room Temperature*

Fig. 4-2 shows cross-section and plan view images along with an SAD pattern from the as-deposited sample. The SAD image is from the plan view image in Fig. 4-2b. Most of the rings in the SAD pattern correspond to Fe reflections; the extra rings (indicated in Fig. 4-2c) match those of off-stoichiometric Fe_3Si. This is an indication that Fe_3Si is present in the as-deposited specimen. Two thin layers are visible at the Fe/Si interface. A plan view image of the interface layer is shown in Fig. 4-3a. The layer adjacent to the Fe layer (~3 nm thick) is amorphous and discontinuous. EDX analysis of this layer, from the plan view specimen (Fig. 4-3c), indicates that it contains a significant amount of oxygen as well as Fe and Si. The layer is likely SiO_2 which was present on the Si surface prior to Fe deposition. The layer adjacent to Si (~5 nm thick) is polycrystalline, as it exhibits diffraction contrast. A selected area diffraction (SAD) pattern (Fig. 4-3b) was obtained from a plan view specimen (see indicated region in Fig. 4-3a) prepared of the interface region. The rings in Fig. 4-3b can be indexed as ordered off-stoichiometric Fe_3Si, which confirms the results obtained above. The SAD pattern provides clear evidence that Fe has diffused through the oxide layer to react with Si forming Fe_3Si as the

initial reaction product. The presence of Fe in SiO_2 layer (Fig. 4-3c) provides further evidence for Fe diffusion towards Si at low temperatures.

There are two possible explanations for Fe_3Si formation. One is that Fe_3Si formed during deposition. The other is that Fe_3Si formed during the TEM specimen preparation. In both cases heating to about 100°C occurred. In either case, Fe_3Si formed at or below 100°C and Fe_3Si was the only silicide identified in the as-deposited specimens.

4.2.2. Annealing Reactions at Low Temperatures

Table 4-1 lists the low temperature annealing conditions that were examined with TEM.

At 300°C, the silicide reactions progress slowly and Fe_3Si was the only iron silicide formed within 2 hours of annealing. A cross section micrograph of a sample annealed at 300°C for 3hrs is shown in Fig.4-4a. Two layers are visible; one corresponds to α-Fe and the other to Fe_3Si. Two silicides, Fe_3Si and FeSi, can be identified from plan view SAD patterns, shown in Fig.4-4b (from the Fe/Fe_3Si interface) and Fig.4-4c (from the Fe_3Si/Si interface). The rings in Fig.4-4b can be indexed to α-Fe and Fe_3Si. The rings shown in Fig. 4-4c can be indexed as Fe_3Si and FeSi. FeSi exhibits a <111> preferred orientation relative to the <111> oriented Si substrate. The rings corresponding to FeSi are quite weak, which indicates that FeSi formation has just begun. In fact, FeSi was not visible in any cross section micrographs (Fig. 4-4a).

At 400°C, silicide growth was more rapid. FeSi was first observed at 400°C after annealing for 20 min. An SAD pattern from the Fe_3Si/FeSi layers is shown in Fig. 4-5. All the rings can be indexed to either FeSi or Fe_3Si. Several Fe_3Si reflections are absent, e.g., the 210 and 211 reflections, which is an indication that Fe_3Si has transformed to the stoichiometric phase. The FeSi preferred orientation is still evident and is more pronounced.

Most of the study was focused on the reactions at 500°C. Silicides, particularly FeSi, grew much faster. After annealing for 5s, FeSi was visible between Fe_3Si and Si. After annealing for 10s, off-stoichiometric Fe_3Si had transformed to stoichiometric Fe_3Si, and the Fe_3Si thickness was ~ 10nm (Fig.4-6). The Fe_3Si thickness was ~35nm and FeSi thickness was about ~50nm after annealing for 3min. This is an indication that both Fe_3Si and FeSi grow simultaneously (Fig. 4-7a). The SAD pattern in Fig. 4-7c from the plan view specimen in Fig. 4-7b indicates that Fe_3Si is stoichiometric. For longer annealing times, a gap between the Fe and FeSi layers is visible (Fig.4-8). Fe films had peeled away from the substrate. The poor interfacial contact resulted in a shortage of Fe, leading to

Fe_3Si consumption by FeSi. The FeSi thickness was greater than 200nm after 2.5hrs of annealing. No clear Fe_3Si layer was found (Fig.4-8). FeSi growth as a function of time is shown in Fig.4-9. FeSi growth is diffusion-controlled. Preferred orientation is evident for short time annealing. For longer annealing times (> 1hr), silicide growth became more random.

No indication of β-$FeSi_2$ formation was found for even the longest annealing times at 500°C. This is in agreement with previous work [142]. β-$FeSi_2$ formation is nucleation controlled [142]; at temperatures less than 500°C, the thermal energy is not sufficient to overcome the activation barrier.

4.2.3. Growth Process of β-$FeSi_2$ at High Temperature (600°C-700°C)

Table 4-2 lists the high temperature annealing conditions which were examined with TEM.

In all cross section samples that had been annealed at high temperature, there is a gap between Fe and silicide layers (as in Fig.4-8). The gaps are similar to those observed for samples annealed at 500°C. There are two possible explanations for the gap formation. One is that Fe_3Si was sputtered away during cross section preparation. The other explanation is that the gap is not a specimen preparation artiface and Fe peeled away from the silicides due to shrintage effects during silicide formation. If the first possibility is correct, it indicates that the Fe_3Si sputtering rate is greater than the other silicides. This is unlikely, however, as previous TEM micrographs show FeSi and Fe_3Si coexisting (e.g. Fig.4-7a). In addition, diffraction analysis of plan view specimens prepared from a sample annealed at 600°C for 15 min revealed reflections belonging only to α-Fe and FeSi.

The more likely scenario is the second one. The following simple mass balance calculation indicates that the gap is real phenomenon. A cross section specimen of a sample annealed at 600°C for 15 min is shown in Fig. 4-10. Only one silicide layer (FeSi) is visible, its thickness measured ≈150 nm. A sample annealed at 600°C for 2 hrs exhibits 2 silicide layers, FeSi and $FeSi_2$, with layer thicknesses of ≈90 nm and 100 nm respectively (Fig. 4-11). Plan view specimens were used to confirm the identities of the silicides. FeSi (small grains) and $FeSi_2$ (large grains) are clearly visible in the TEM micrograph shown in Fig. 4-12. Assuming bulk densities - which are not strictly correct, but reasonable - to form 100 nm of $FeSi_2$ would require consumption of ≈60 nm of FeSi. The 60 nm of FeSi accounts for the reduction in FeSi thickness from 150 nm to 90 nm. This calculation is based on the assumption that the Fe layer has delaminated and is no longer a source for

the thin film reactions. In other words, the amount of $FeSi_2$ can be completed accounted for by the consumption of FeSi.

The gap arises due to shrinkage effects as illustrated in the following simple calculation. To form 10 nm of Fe_3Si and 10 nm of FeSi at Fe/Si interface, requires 11.9 nm Fe +Si and 13.9 nm Fe + Si respectively. The total thickness of Fe and Si consumed in both cases is greater than the thickness of silicide formed. The corresponding shrintage will result in the formation of a gap. Scince Fe is the major diffuser in Fe_3Si, the gap must appear on the Fe side.

Examination of samples annealed at 700°C yields similar results. After 1 min of annealing, a single FeSi layer, ≈220 nm thick, had formed. After 2 min of annealing, $FeSi_2$ started to form (Fig.4-13). After 2 hrs, only $FeSi_2$ was observed. The thickness of the $FeSi_2$ layer was ≈380 nm, which again can be accounted for solely through the consumption of the FeSi layer.

The formation of $FeSi_2$ at 600°C-700°C relies on Si diffusion through $FeSi_2$ and the consumption of FeSi at $FeSi/FeSi_2$ interface according to the following:

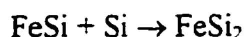

$$FeSi + Si \rightarrow FeSi_2$$

$FeSi_2$ formation is diffusion controlled, as indicated by the $\sqrt{t}$ dependence of thickness in Fig.4-14.

4.3 The Formation Sequence of Iron Silicides

4.3.1. The Assumptions

In order to explain initial phase formation in Fe/Si thin film couples, the following assumptions, based on Zhang and Ivey's kinetic model, were adopted [145]:

1. The phase boundary between the growing phase (the product) and contracting phase (the nonmoving reactant) is assumed to be the reaction region (Fig.4-15a).
2. One of the reactants diffuses through the growing phase to arrive at the reaction region and is considered to be the moving reactant (M). The other reactant (i.e., the element or compound which makes up the contracting phase) is considered to be a nonmoving reactant (N) due to its low diffusivity in the growing phase. If the moving reactant does not dissolve in the contracting phase (as in most silicide formation reactions), some of the nonmoving reactant has to dissolve from its own lattice into the reaction region. The two reactants atomically mix together in the reaction region. These atoms then rearrange themselves on the lattice of the growing phase.

reaction region is kinetically preferred. Since the number of dissolved nonmoving atoms in the reaction region is limited, the composition in this region mainly depends on the diffusivity of the moving reactant.

4. In the reaction region, the reaction must satisfy the basic thermodynamic criterion, which is $\Delta G<0$, where ΔG is Gibbs free energy for the reaction.

According to these assumptions, a kinetic model to describe the solid state reactions in thin film metal-silicon diffusion couples has been proposed [141]. In this model, 2 main physical quantities control the reaction process. These are the diffusion flux (J) of M into the reaction region and the release rate (r) of non-moving reactant (N). The relationship between the release rate r and diffusion flux J determines which silicide compound will form [153].

An expression for the maximum release rate of the non-moving reactant for a given silicide (i.e., the ith silicide) was given in [141]:

$$r_{i\,max} = n^* \nu \exp(-\frac{E}{kT})\exp(-\frac{\Delta G_i}{kt})$$
$$= n^* \nu \exp(-\frac{E+\Delta G_i}{kT}) \quad (4\text{-}1)$$

ν is the vibration frequency of non-moving reactant atoms at the surface exposed to the reaction region; ΔG_i is the driving force for the reaction, i.e., the free energy change for the reaction per N atom, for ith silicide to form; n^* is the number density of n atoms per unit area of exposed surface layer; E is the energy barrier. In a given reaction region, n^*, ν and E are the same for all possible reactions so that r_{imax} is exponentially dependent on the driving force for the reaction. Equation (4-1) can be simplified to the following relationship for the relative maximum release rate at 2 silicide reaction [141]:

$$\frac{r_{imax}}{r_{1max}} = \exp(-\frac{\Delta G_i - \Delta G_1}{kT}) \quad (4\text{-}2)$$

r_{1max} is the maximum release rate of the silicide which has the smallest negative value of ΔG_i (ΔG_1). Enthalpy values (ΔH) are more readily available than free energies, so that ΔH_{298}, i.e., the standard enthalpy change at 298K, is used in place of ΔG. This is a reasonable approximation as entropy effects are expected to be minimal. Eq.(4-2) then becomes:

$$\frac{r_{imax}}{r_{1max}} = \exp(-\frac{\Delta H_i - \Delta H_1}{kT}) \quad (4\text{-}3)$$

An arbitrary value, 1 at. $cm^{-2}s$, is assigned to r_{1max} , so that other values are calculated relative to it. Semiquantitative reaction process plots can be obtained from Equation (4-3), using enthalpy values [141]. For a given diffusion flux, the silicide with the largest relative

maximum release rate should form first. Iron silicide relative maximum release rates for 500°C were calculated and the semiquantitative reaction process plot is shown in Fig.4-16. The plot is based on Fe being the major diffuser and Si being the non-moving reactant. The relative maximum release rate is largest for Fe_3Si. Any change in the diffusing species and/or change in non-moving reactant would require calculation of a new reaction process plot.

4.3.2. Explanation for the Iron Silicide Formation Sequence

The initial stages of silicide formation are indicated in Fig. 4-15b. This figure is virtually the same as Fig. 3-17, except for the thin native oxide layer. The oxide layer can be considered to be inert (acts as a marker) and is not involved in the silicide reactions. The oxide layer may affect diffusion rates and may have some bearing on which element is the major diffuser. Initially, Fe diffuses through the oxide layer (Fig.4-15b) to arrive at the oxide/Si interface. Below 700°C, three reactions are thermodynamically possible:

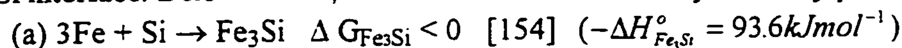
(a) $3Fe + Si \rightarrow Fe_3Si \quad \Delta G_{Fe_3Si} < 0 \quad [154] \quad (-\Delta H^o_{Fe_3Si} = 93.6 kJmol^{-1})$

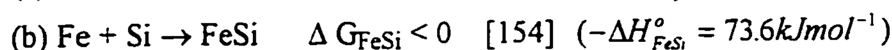
(b) $Fe + Si \rightarrow FeSi \quad \Delta G_{FeSi} < 0 \quad [154] \quad (-\Delta H^o_{FeSi} = 73.6 kJmol^{-1})$

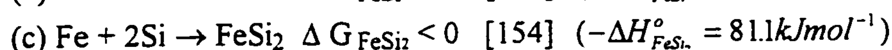
(c) $Fe + 2Si \rightarrow FeSi_2 \quad \Delta G_{FeSi_2} < 0 \quad [154] \quad (-\Delta H^o_{FeSi_2} = 81.1 kJmol^{-1})$

The Fe diffusion flux determines which reaction is the kinetically preferred. In Fig.4-16, the Si release rate for Fe_3Si formation is the largest. Therefore, if the diffusion rate of Fe is high enough, Fe_3Si formation will be preferred.

Subsequent silicide formation is shown schematically in Fig. 4-17. After Fe_3Si forms, the diffusion flux of Fe decreases with increasing Fe_3Si thickness. Defects in the Fe film also can reduce diffusivity of Fe as annealing time increases [153]. When the Fe diffusion flux reaches a critical value (J_{ILC}) (Fig.4-16) [155], FeSi formation is preferred. Once FeSi forms, FeSi and Fe_3Si grow simultaneously. Fe may continue as the major diffuser through FeSi (Fig. 4-17b) or the Fe diffusion rate may decrease to such a level that Si becomes the major diffuser through FeSi (Fig. 4-17c). From this work, it was not possible to determine the major diffuser in FeSi, however, previous research has indicated that Si is the major diffuser in FeSi [15]. With increasing annealing time, due to the stresses induced during the annealing, the Fe film peels away from the silicide, eliminating the Fe source (Fig.4-17d). Fe_3Si is then consumed by FeSi. Si is the major diffuser through FeSi. When the annealing temperature is above 600°C, delimitation occurs sooner and Si becomes the major diffuser. β-$FeSi_2$ nucleates [142] and grows very rapidly (Fig.4-17e). β-$FeSi_2$ is the major silicide for high temperature annealing.

For thin films, previous work shows that intermetallic compounds tend to form alone; that is, they grow one by one in sequence rather than together at the same time [131,132]. Our work shows that FeSi and Fe_3Si grow simultaneously. This difference can be explained by Zhang's model (Fig.4-16). If the thin film is very thin, the diffusion flux of moving specie can not reach the critical value (J_{ILC}). Therefore only one phase forms alone. In our work, Fe thickness is 165 nm. The diffusion flux of Fe can reach the J_{ILC}. Therefore Fe_3Si and FeSi grow in same time.

4.4. Conclusions

From the thin film work, the following conclusions have been obtained.

(1) Off-stoichiometric Fe_3Si formed below 100°C and was the only silicide to form at the Fe/Si interface in as-deposited specimens.

(2) Fe is the major diffuser during Fe_3Si formation.

(3) During low temperature annealing from 300°C to 500°C, off-stoichiometric Fe_3Si transformed to stoichiometric Fe_3Si.

(4) FeSi formed at temperatures ranging from 300-500°C. At 500°C, Fe_3Si and FeSi grow simultaneously first and then Fe_3Si is consumed due to Fe delamination from substrate. FeSi growth is diffusion controlled.

(5) During high temperature annealing (600°C to 700°C), Si is the major diffuser and β-$FeSi_2$ is the main silicide.

(6) β-$FeSi_2$ formation is nucleation controlled. At 700°C, β-$FeSi_2$ growth diffusion is controlled.

(7) A semiquantitative reaction process plot for the Fe-Si system was calculated and drawn. Fe_3Si formation can be explained using this model.

Table 4-1 Low temperature annealing conditions for Fe/Si thin film couples.

Temperature (°C)	Time (hour:min)	Temperature (°C)	Time (hour:min:s)	Time (hour:min)
300	3:00	500	0:0:05	0:45
300	4:00	500	0:0:10	1:00
300	6:00	500	0:0:15	1:30
400	0:15	500	0:0:30	2:00
400	0:20	500	0:1:00	2:30
400	0:30	500	0:2:00	
400	1:00	500	0:3:00	
400	2:00	500	0:5:00	
400	6:00	500	0:30:00	

Table 4-2 High temperature annealing conditions for Fe/Si thin film couples.

Temperature (°C)	Time (hours:min)	Temperature (°C)	Time (hour:min:s)	Time (hour:min:s)	Time (hour:min)
600	0:05	700	0:00:01	0:05:00	0:30:00
600	0:30	700	0:00:05	0:10:00	1:00:00
600	1:00	700	0:01:00	0:15:00	2:00:00
600	2:00	700	0:02:00	0:20:00	

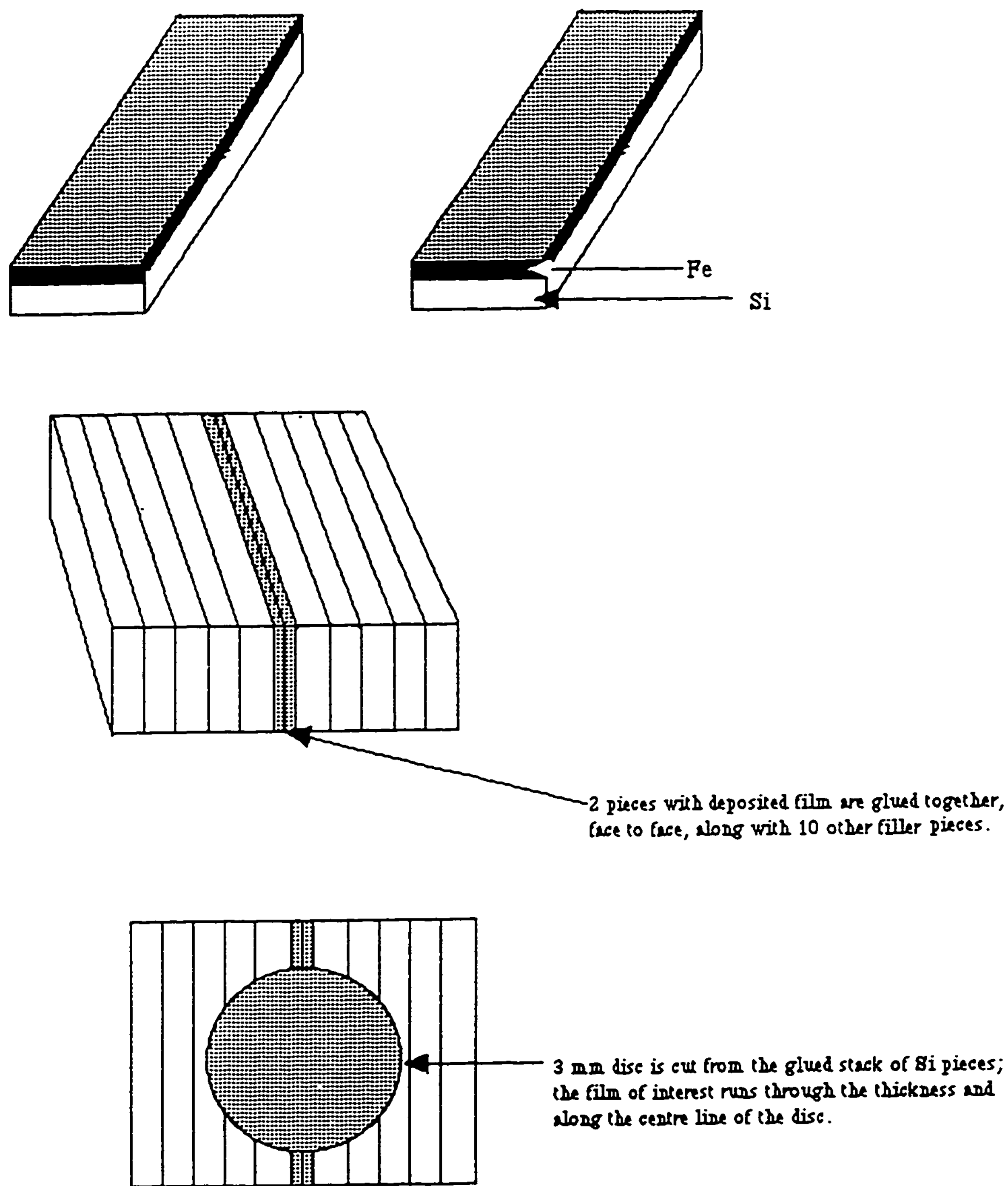

Fig. 4-1 Construction of cross-sectional TEM samples.

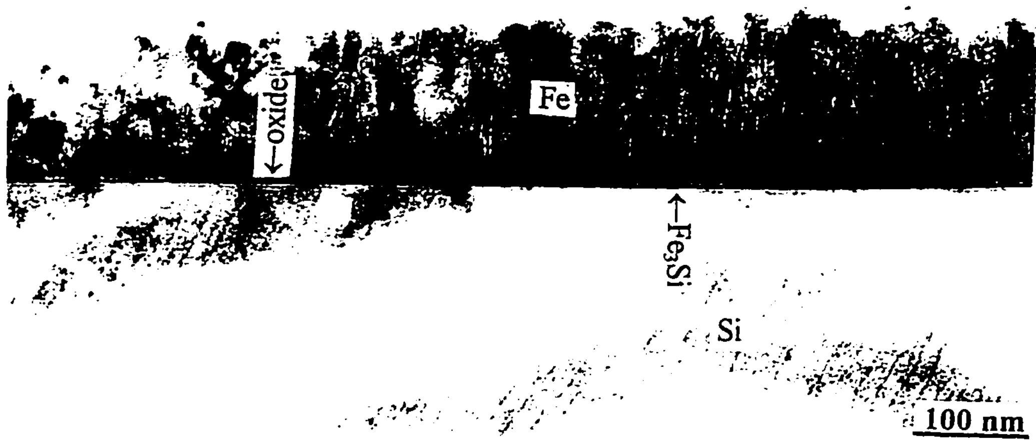

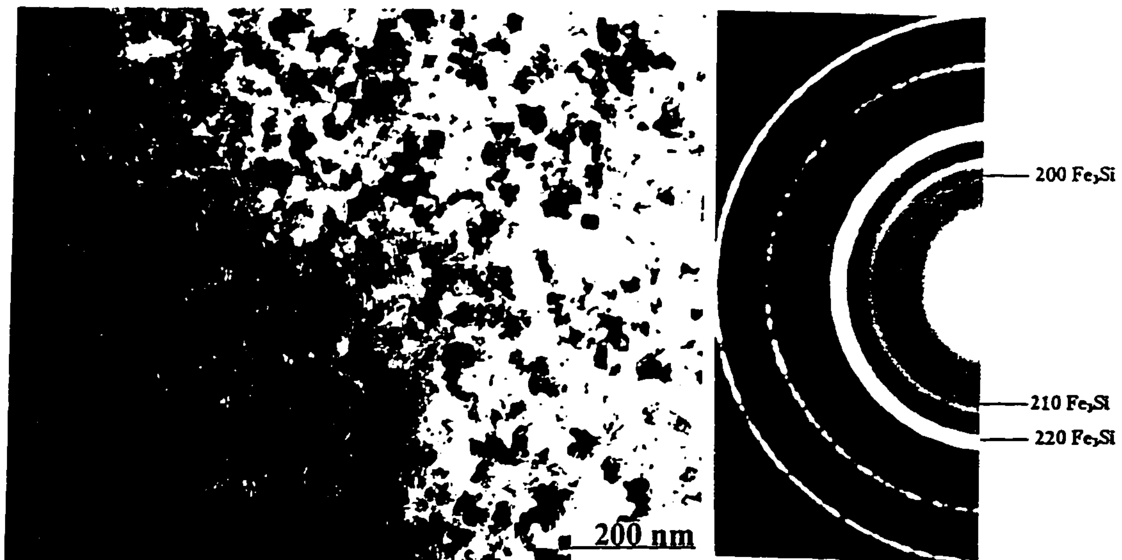

Fig.4-2 TEM micrographs from as-deposited specimen: a) cross section sample, b) plan view sample and c) an SAD pattern from the region shown in (b).

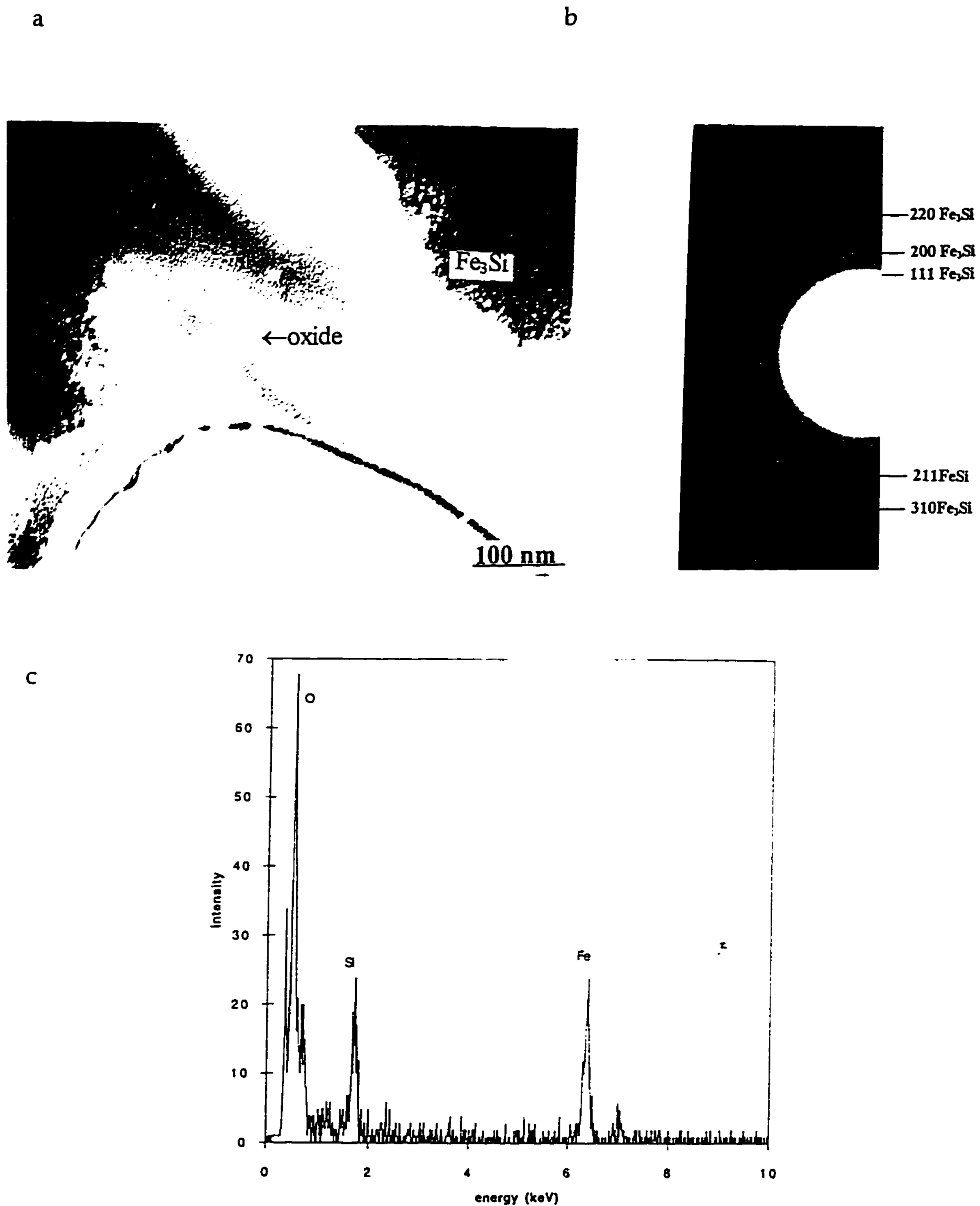

Fig. 4-3 a) TEM plan view micrograph of Fe/Si interface in as-deposited specimen, b) SAD pattern from polycrystalline region, c) EDS spectrum from amorphous region.

a

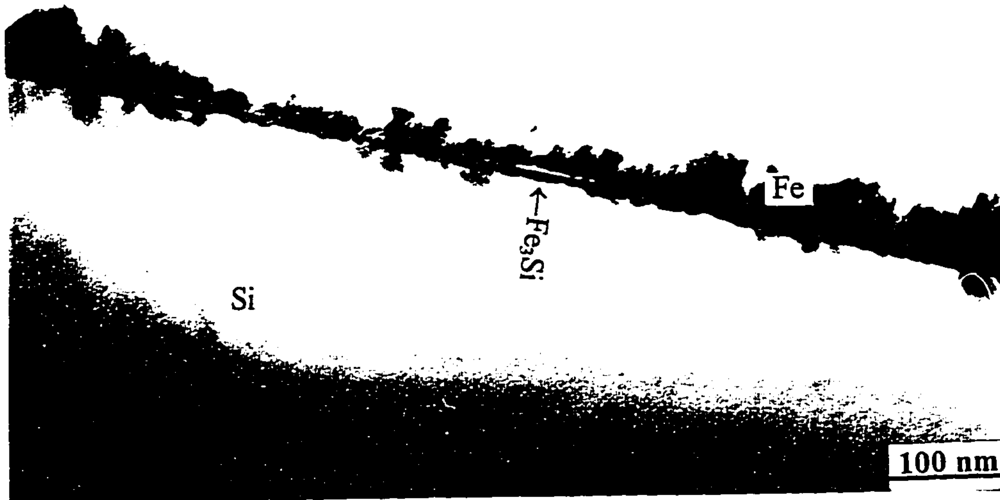

b

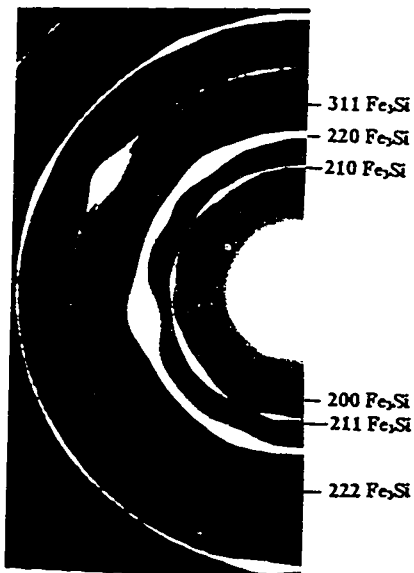

c

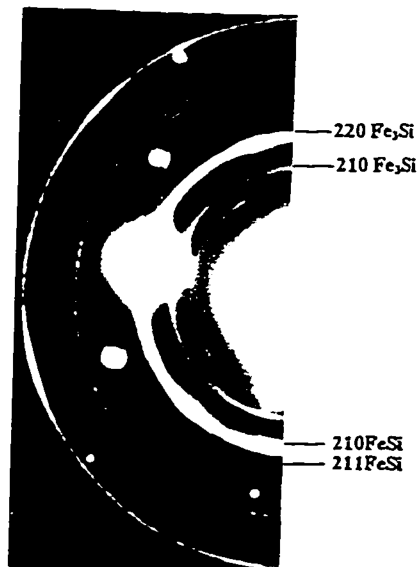

Fig. 4-4 TEM micrographs of Fe/Si interface in specimen annealed at 300°C for 3 hrs: a) cross section; b) an SAD pattern from Fe_3Si; c) an SAD pattern from Fe_3Si and FeSi.

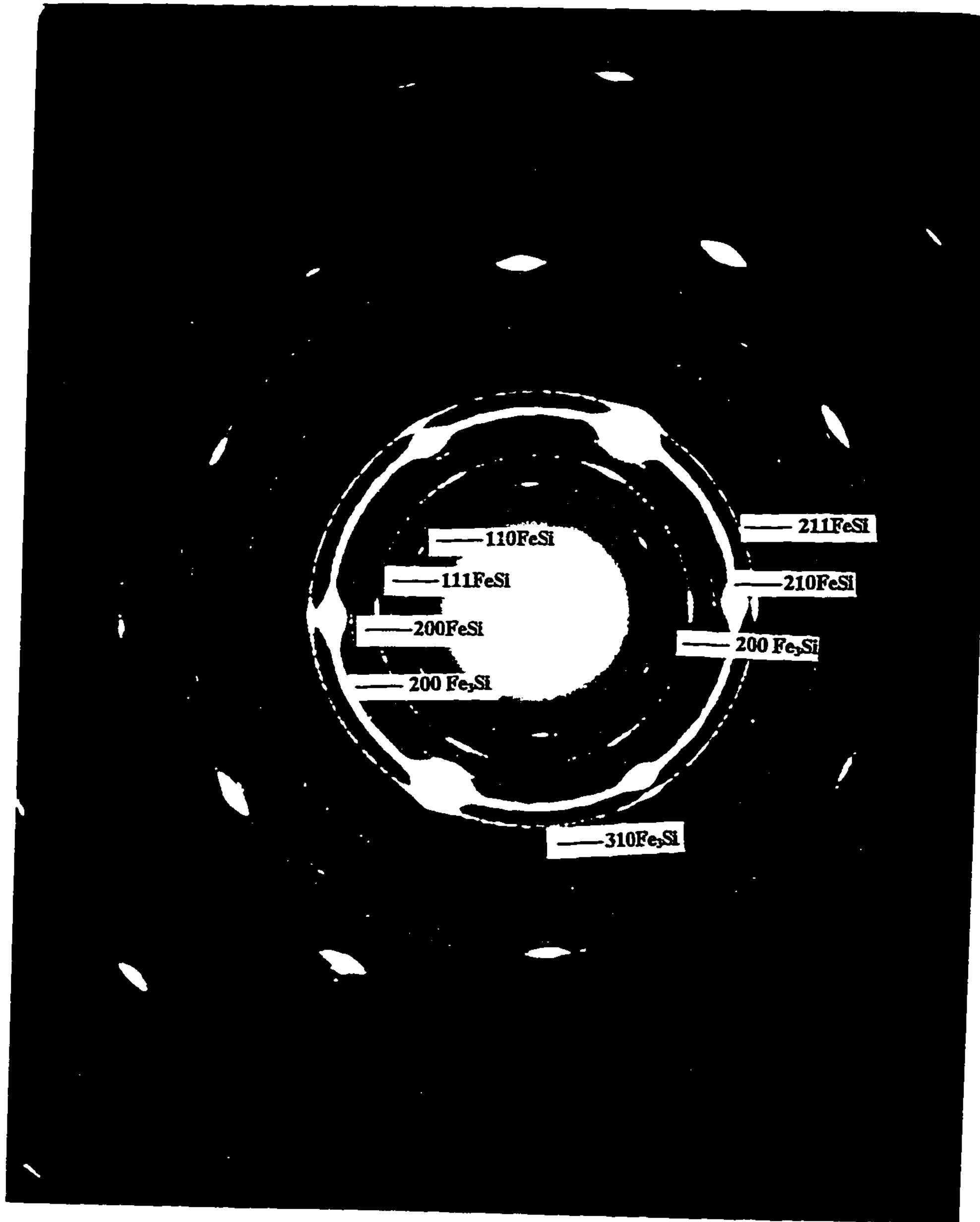

Fig. 4-5 SAD pattern from Fe_3Si and FeSi layers in specimen annealed at 400°C for 1 hr. Off-stoichiometric Fe_3Si has transformed to stoichiometric Fe_3Si.

Fig.4-6 TEM micrograph of cross section specimen annealed at 500°C for 10 sec.

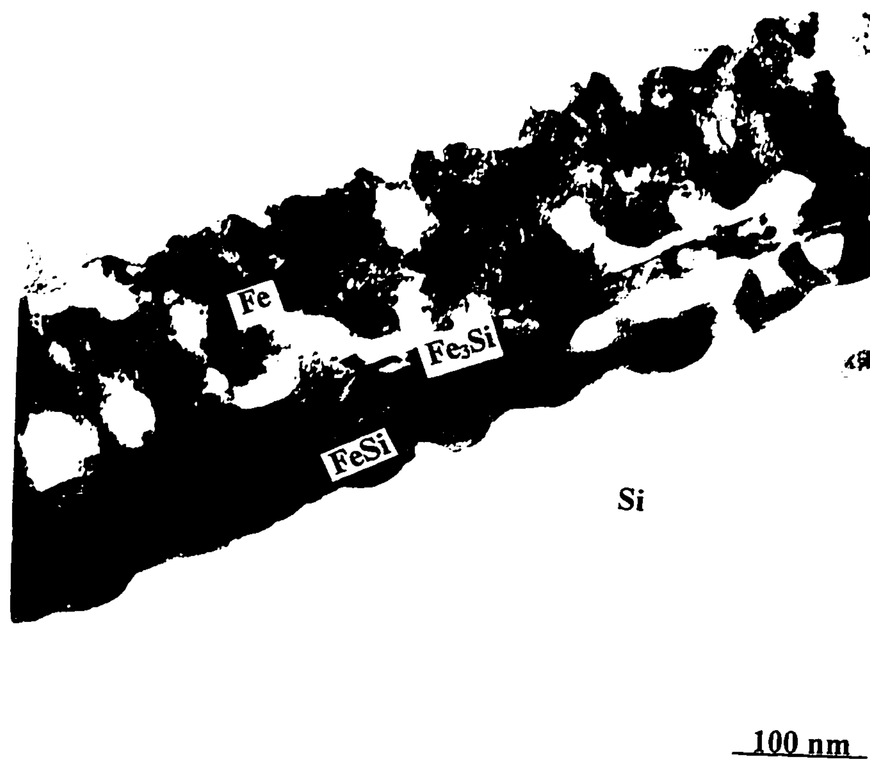

Fig. 4-7 TEM micrograph of a cross section from the thin film sample annealed at 500°C for 3min.

b

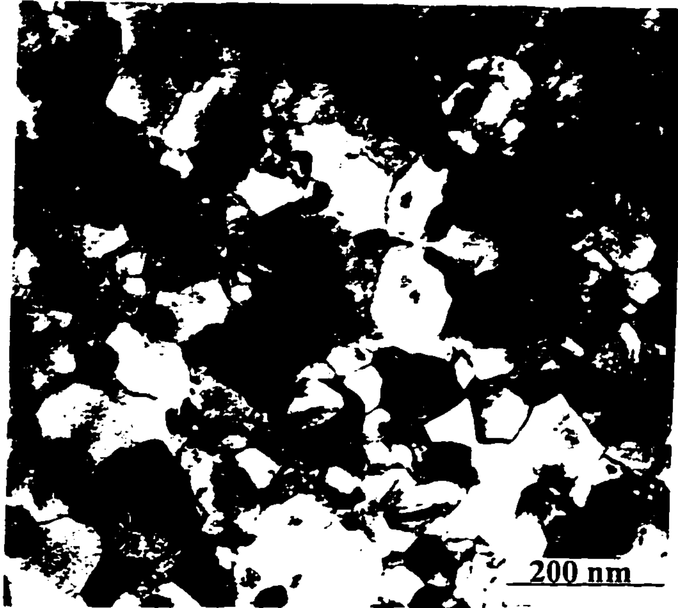

c

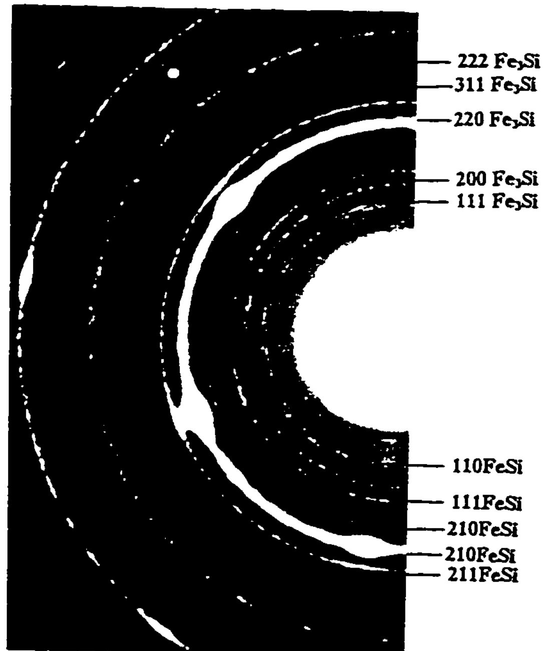

Fig. 4-7 b) Plan view micrograph and c) SAD pattern from FeSi and Fe_3Si layers in specimen annealed at 500°C for 3 min.

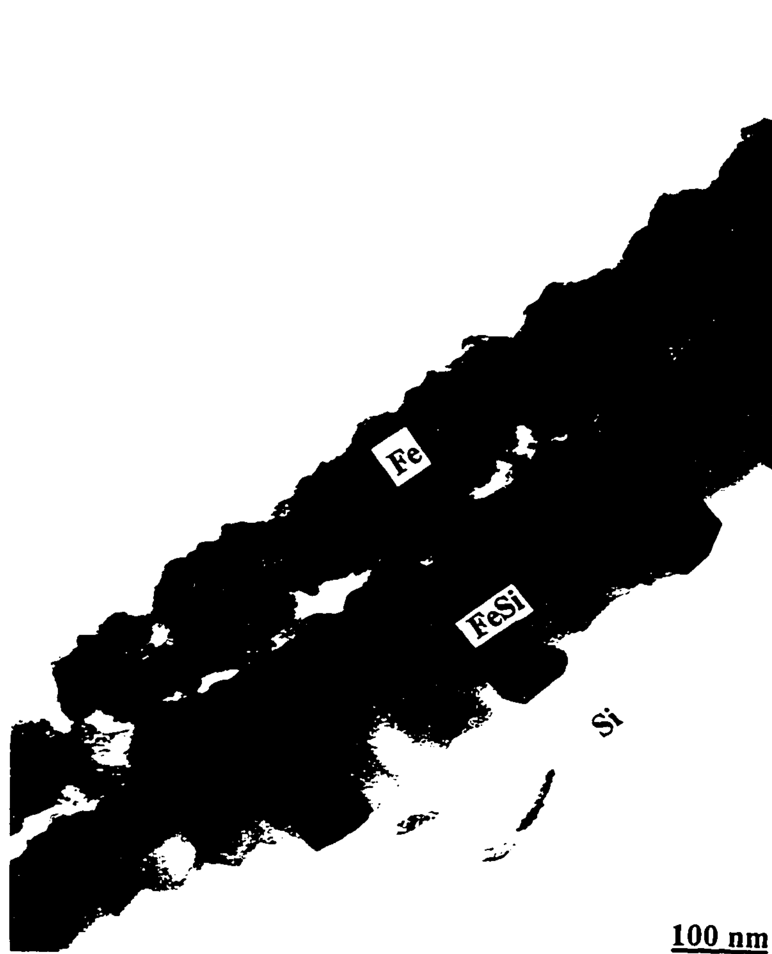

Fig. 4-8 TEM micrograph of a cross section from the thin film sample annealed at 500°C for 2.5hrs.

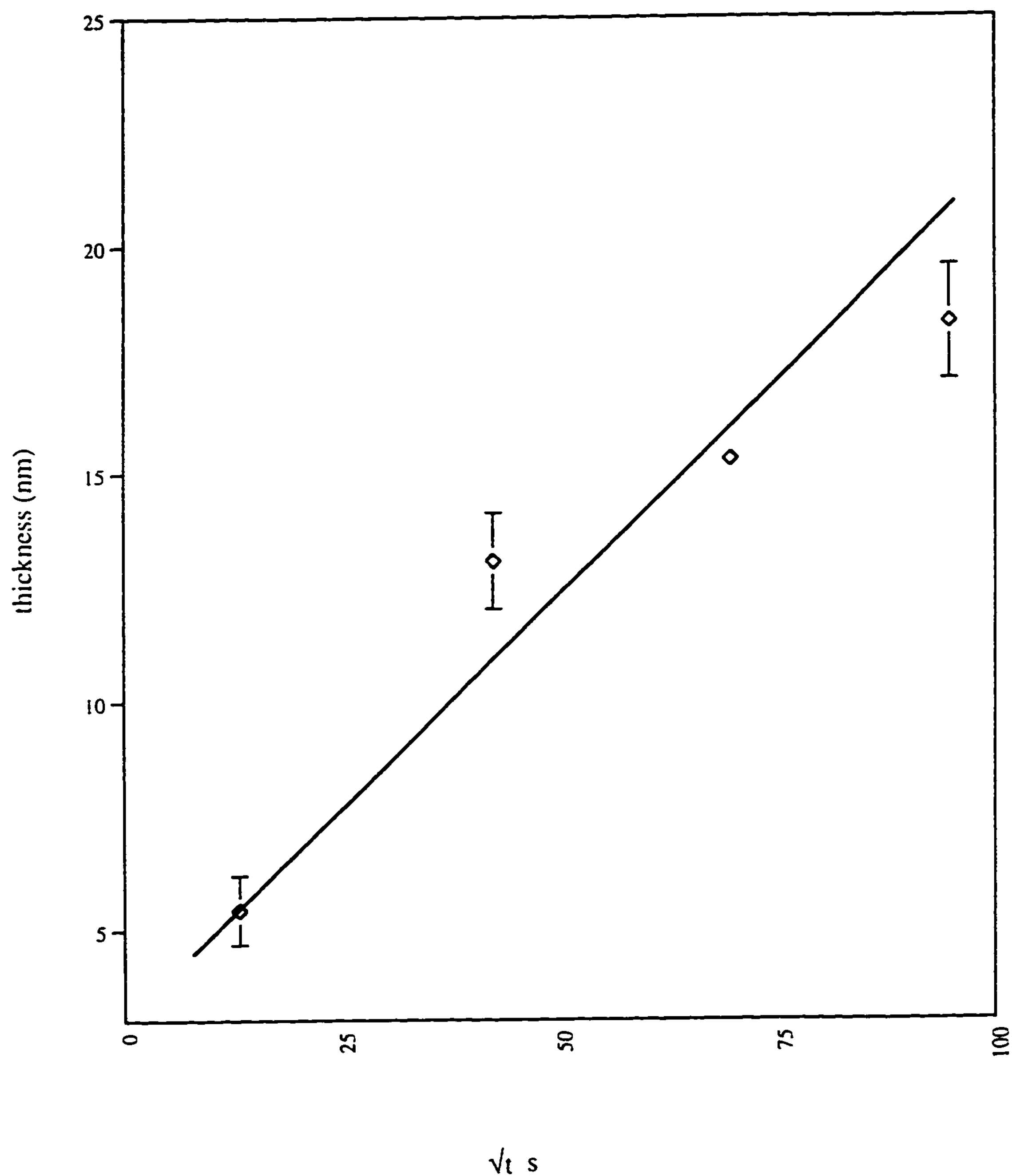

Fig.4-9 Thickness of FeSi as a function of time in Fe-Si thin films at 500oC. Error bars represent one standard deviation (±) in the thickness measurments.

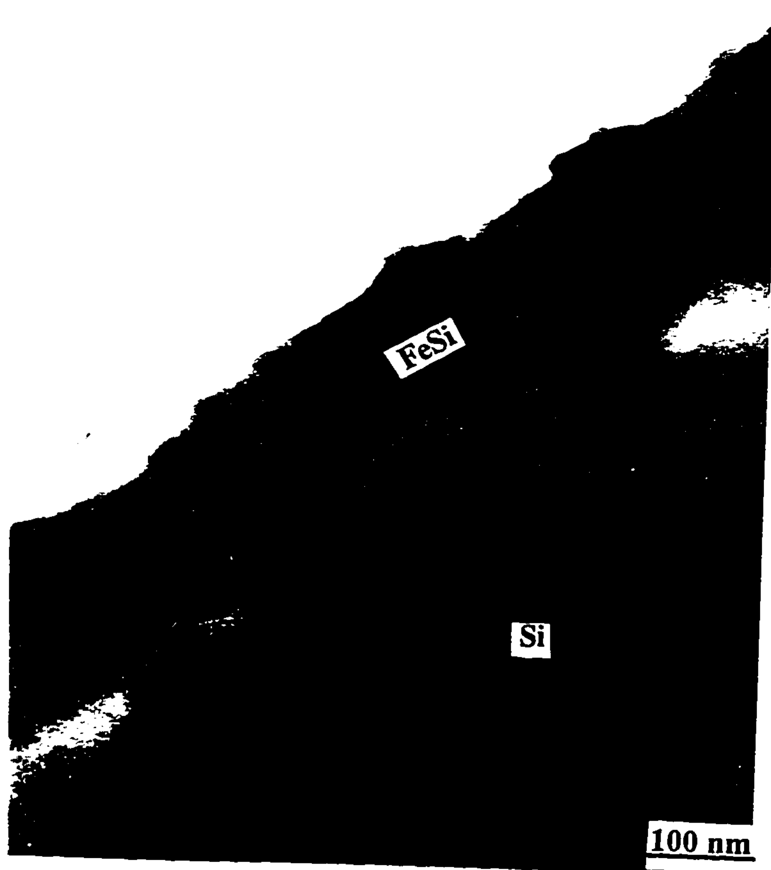

Fig. 4-10 TEM micrograph of a cross section from the thin film sample annealed at 600°C for 15 min.

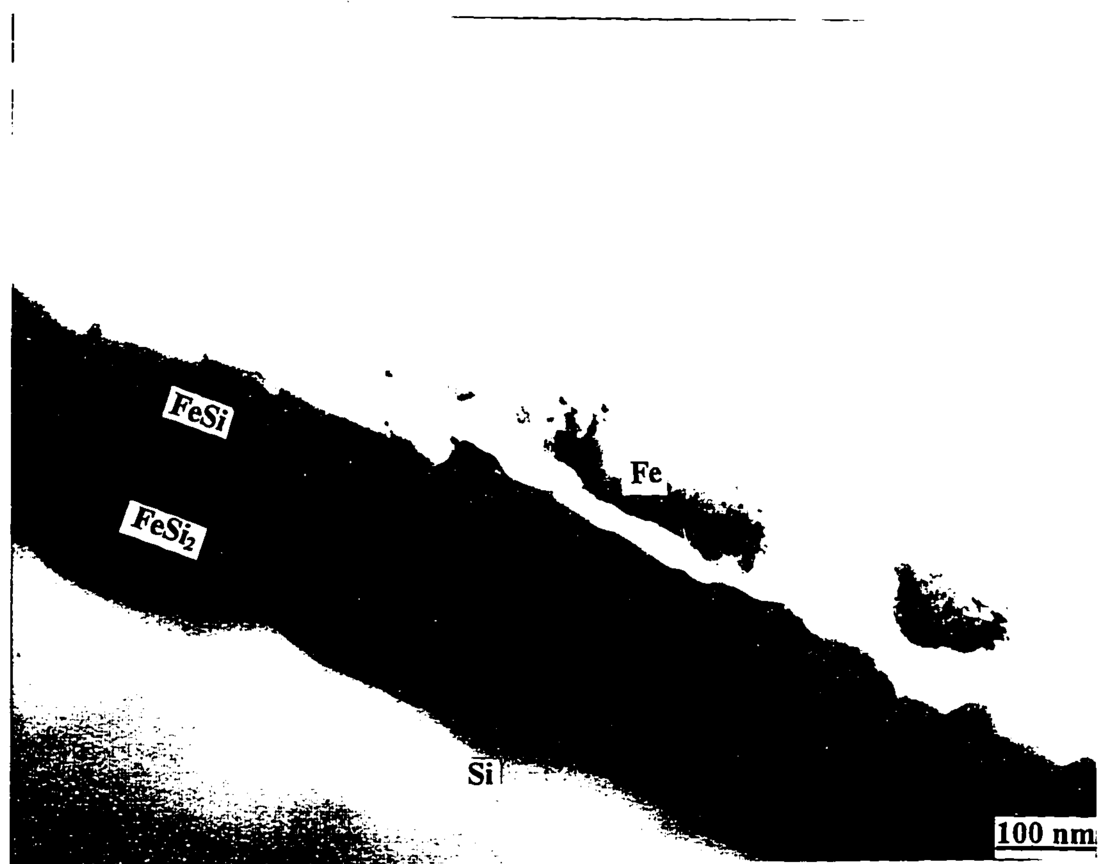

Fig. 4-11 TEM micrograph of a cross section from the thin film sample annealed at 600°C for 2 hrs.

Fig. 4-12 TEM micrograph of a plan view from the thin film sample annealed at 600°C for 75 min.

Fig. 4-13 TEM micrograph of a plan view from the thin film sample annealed at 700°C for 2min.

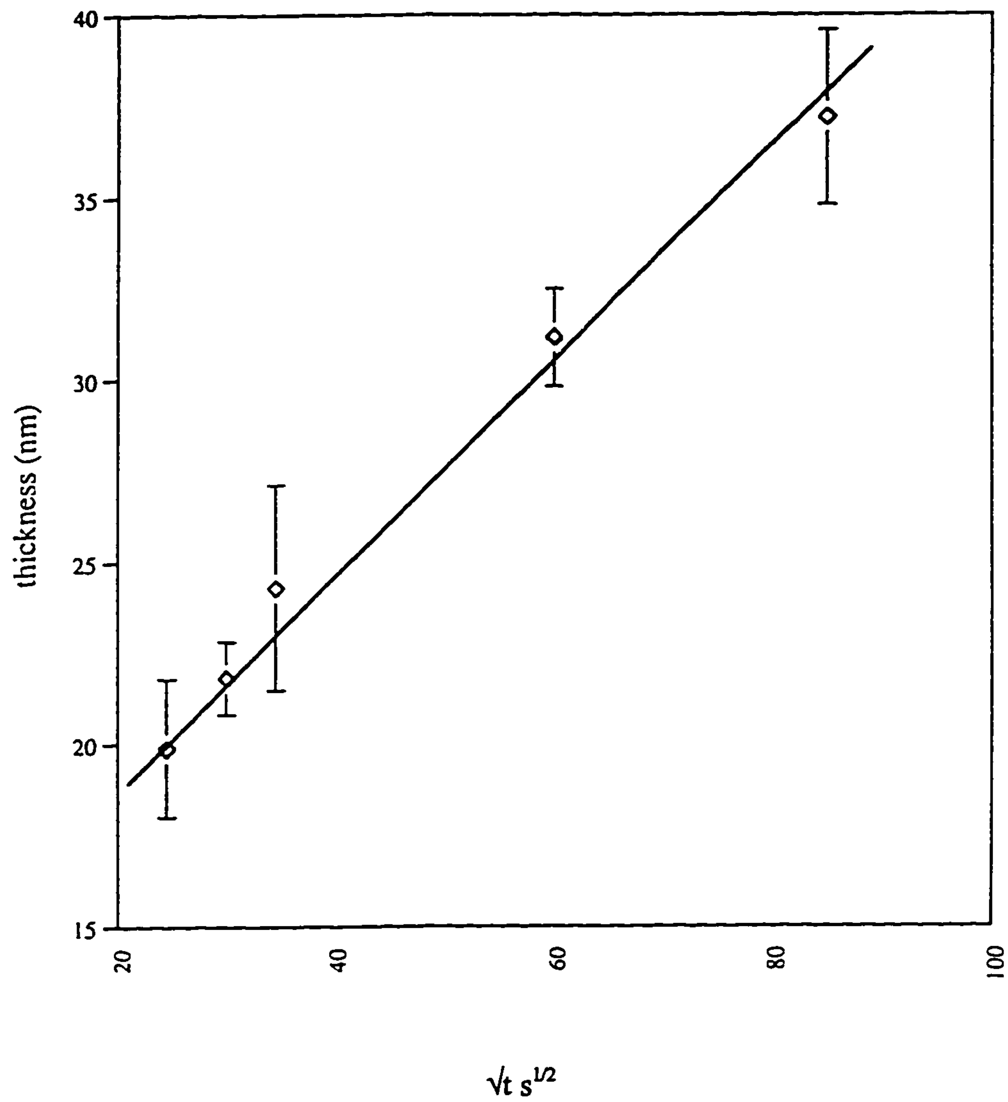

Fig. 4-14 β-FeSi2 thickness as a function of time at 700oC.Error bars represent one standard deviation (±) in the thickness measurments.

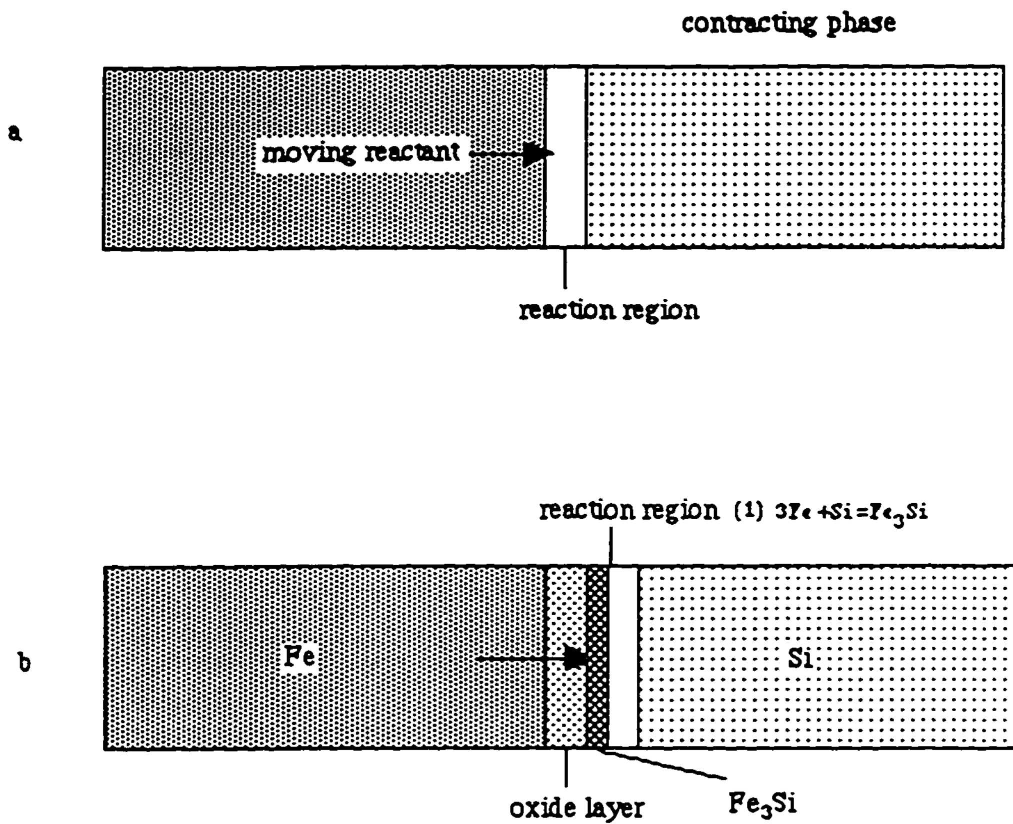

Fig.4-15 a) Schematic representing kinetic model for silicide formation. The interface region between the growing phase and the contracting phase is assumed to be the reaction region (not to scale).

b) Schematic of initial stages of silicide formation in Fe-Si thin film couples.

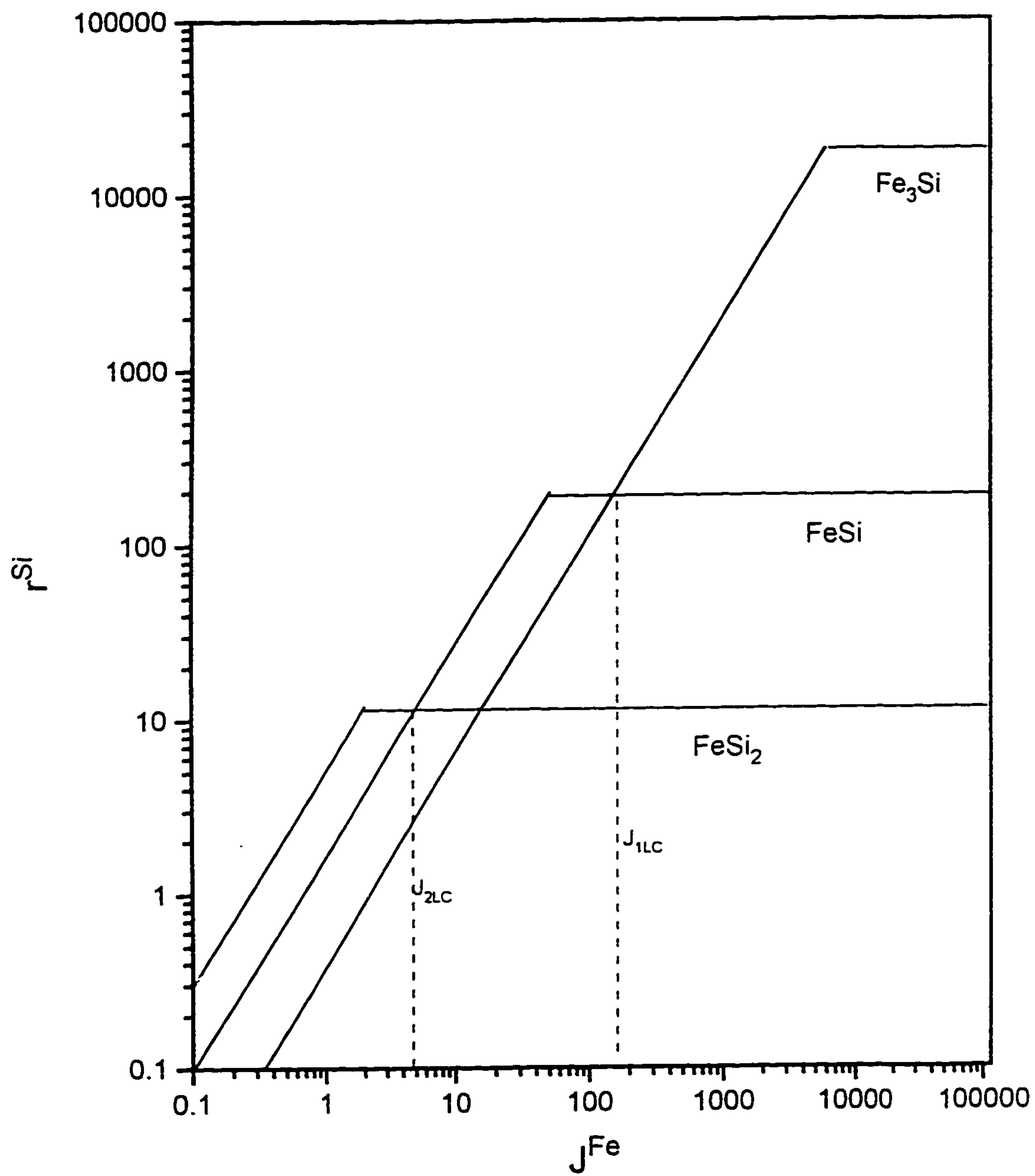

Fig. 4-16 Semiquantitive reaction process plot for Fe-Si system.

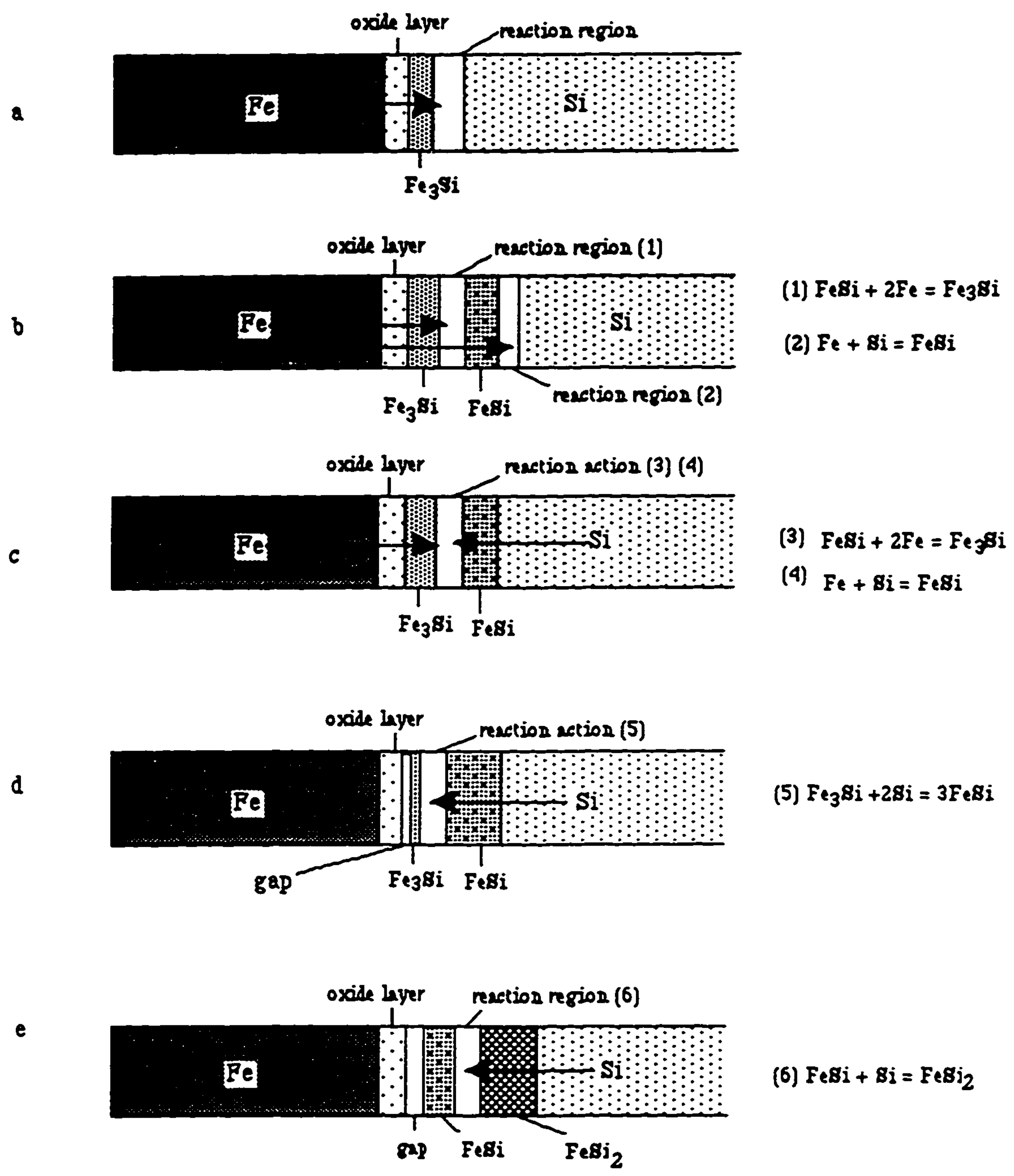

Fig. 4-17 Summary of silicide formation in Fe-Si thin films.

Chapter 5. Comparison of Thin Film and Bulk Couple Results

Overall, the thin film diffusion couple results are in good agreement with the results for the bulk diffusion couple work. The common results are listed as follows:

- The silicides appear in the following order: Fe_3Si is the first silicide to form, followed by FeSi and then β-$FeSi_2$.
- Fe is the major diffuser in Fe_3Si.
- Stoichiometric Fe_3Si is the most stable form of Fe_3Si.

The differences are as follows:

- In bulk diffusion couples, stoichiometric Fe_3Si was observed to form first, and in all couples studied, Fe_3Si was stoichiometric. In thin film couples, off-stoichiometric Fe_3Si formed first, but quickly transformed to stoichiometric Fe_3Si during annealing. One possibility is that there is indeed no difference between the two type of couples. In the bulk couples, off-stoichiometric Fe_3Si may have formed before 7 hrs and transformed to stoichiometric Fe_3Si. The transformation may have been missed. The other possibility is that many defects exist in the thin films and these defects may affect the silicide formation and growth.
- In bulk couples, iron silicides form more slowly than in the thin film couples. The silicide formation temperatures are lower for the thin films, i.e., $\leq 500°C$. FeSi forms after annealing for 5s in thin films, at 700°C; FeSi forms only after annealing for 23 hrs in bulk couples. The difference in reaction rates may be related to surface cleanliness. For the bulk couples, the surface of Fe and Si can be contaminated during polishing, i.e., oxides can form on the Fe and Si surfaces. The contamination may delay the rate of reaction. This is one reason iron silicides form more slowly in bulk couples than in thin films. The much smaller Fe grain size and high defect density in thin films than in bulk couples will markedly increase diffusion rates. The volume diffusion coefficients are really too slow to explain the very rapid growth of thin films and better agreement is observed with grain boundary diffusion coefficients [130]. A simple order of magnitute calculation can be used for illustration. The volume diffusion coefficient D_v can be expressed: $D_v = D_o \exp(-Q_v/RT)$. Q_v is a volume activation energy per molar unit, D_o is frequency factor, R is the gas constant, and T is the absolute temperature. According to Fig.2-5, the volume activation energy of Fe diffusion in Fe_3Si (19.22at%Si) can be calculated, and Q_v is $\approx$ 176

kJ/mol. If one assumes that activation energy for grain boundary diffusion $Q_{g.b}$ is ≈ $1/2Q_v$ (and D_o is the same as for volume diffusion), then the grain boundary diffusion coefficient for Fe diffusion in Fe_3Si (19.22at% Si) is ~ $4x10^4$ times higher than the volume diffusion coefficient for the same composition at 700°C. Therefore silicide growth in thin films would be expected to be much faster than in bulk couples.

- At 700°C, in bulk couples, Fe_3Si is the major silicide; in thin films, β- $FeSi_2$ is the major silicide. For long term high temperature annealing, Fe films peel away from the substrate due to the stresses induced during annealing. Once delamination happens, the Fe supply is cut off. Si becomes the major diffuser. Therefore, in thin films, β- $FeSi_2$ is the major silicide. On the other hand, in bulk couples, there is essentially an unlimited supply of Fe.

Chapter 6. Conclusions and Recommendations

Comparing bulk couple and thin film work, some conclusions can be obtained:

- Electron diffraction can be used efficiently to identify stoichiometric Fe_3Si and off-stoichiometric Fe_3Si, especially for polycrystalline, i.e. Fe_3Si in thin films.
- Silicides form in the same order in bulk couples and thin films, Fe_3Si forms first, then FeSi and β-$FeSi_2$.
- If Fe is sufficient, Fe_3Si is the major silicide and Fe_3Si, FeSi and β-$FeSi_2$ grow simultaneously. Three silicides are diffuse-controlled growth.
- If Fe is insufficient during annealing, Si becomes the major diffuser, Fe_3Si is consumed by FeSi and FeSi is consumed by β-$FeSi_2$. β-$FeSi_2$ is the major silicide.
- β-$FeSi_2$ forms above 600°C in thin films.
- Stoichiometric Fe_3Si is the most stable form of Fe_3Si.
- Silicide formation and growth are faster in thin films than in bulk couples.

Investigation of bulk couples has an important significance for studying of thin films. According to bulk couple results, we can predict silicide behavior in thin films. Although most work for Fe-Si system has been done, some questions are still needed further to be solved. Firstly, the major diffuser in FeSi and β-$FeSi_2$ for bulk couples is needed to be further investigated; more evidence needs to be found to check the interfaces on which FeSi and β-$FeSi_2$ form in bulk couples; secondly, how defects in thin films and pollution on Fe and Si surfaces in bulk couples affect the silicide formation and growth need to be known; thirdly, improving deposition methods to prevent Fe film from peeling off need to be done.

References:

1. S. P. Murarka, Silicides for VISL Application, Academic, New York, 1983.
2. Y. Dusauaoy, J. Pratas, R. Wandji and B. Roques, *Acta Crystallgr. B,* 27 (1971) 1209.
3. M.C. Bost and J.E. Mahan, *J. Appl. Phys.*, 58 (1985) 2696.
4. K. Lefki, P. Muret, N. Cherief and R. C. Cinti, *J. Appl. Phys.*, 69 (1991) 352.
5. A. Rizzi, H. Moritz and H. Lüth, *J. Vac. Sci. Technol.* A 9 (1991) 912.
6. J. M. Gallego and R. Miranda, J. Alvarez and R. Miranda, *Phys. Rev. B* 4 (1992) 13339
7. O. Kubaschewshi, *Iron-Binary Diagrams,* Springer-Verlag, New York, (1982) 1362.
8. A. C. Swintendick, *Solid State Commun.*, 19 (1976) 511.
9. H. Von. Kanel, K.A. Müder, E. Müller, N. Onda and H. Sirringhaus. *Phys. Rev. B,* No.23, 45 (1992) 13807.
10. U. Kafader, P. Wetzel, C. Pirri and G. Gewinner, *Appl. Surf. Sci.*, 70/71 (1993) 537.
11. Y. Ufuktepe and M. Orellion, *Solid State Commun.* No.2 76 (1990) 191.
12. M. De Crescenzi, G. Gaggiatti, N. Matta, F. Patella, A. Balzaratti and J. Derrien, *Appl. Phys. Rev. B* 42 (1990) 587.
13. H. Moritz, B. Rösen and S. Popvic, A. Rizzi and H. Lüth, *J. Vac. Sci. Technol.*, B10 (4) (1992) 1704.
14. E. R. Weber, *Appl. Phys.* A 30 (1983) 1.
15. S. S. Lau, J. S.Y. Feng, J. O. Olowolafe and M. A. Nicolet, *Thin solid films,* 25 (1975) 415.
16. H. C. Cheng, T. R. Yew and L. J. Chen, *J. Appl. Phys.*, 57 (1985) 12.
17. Q. G. Zhu, H. Iwaski, E.D. Williams and R. L. Park, *J. Appl. Phys.*, 60 (1986) 2629.
18. J. M. Gallego and R. Miranda, *J. Appl. Phys.* 69 3 (1991) 1377.
19. K. Radermacher, S. Mantl, Ch. Dieker and H. Lüth, C. Freiburg, *Thin Solid Films,* 215 (1992) 76.
20. C.A. Dimitriadis and H. Werner, *J. Appl. Phys.* 68 (1990) 93.
21. K. Konuma, J. Vrijmoeth, P. M. Zagawijin, E. Vlieg and J.F. Van der Veen, *Appl. Surf. Sci.*, 70/71 (1993) 564.
22. J. Alvarez, J.J. Hinarejos, E.G. Michel and R. Miranda, *Surf. Sci.*, 287/288 (1993) 490.

23. I. D. Khabelasvili, Y. Lebedinshkii and V. N. Nevolin, *Thin solid Films*, 247 (1994) 39.
24. M. Kasaya, S. Yamauchi, M. Hirai, M. kusaka, M. Iwami, H. Nakamura and H. Warabe, *Appl. Surf. Sci.*, 75 (1994) 10.
25. G. Y. Molnar, G. Peto, E. Zscodloes, Z. E. Horvath and N. Q. Khnah, *Mat. Res. Soc. Symp. Proc.*, 402 (1996) 337.
26. M. Fanciulli, C. Rosenbled, G. Weyer, H. Von kanel, N. Onda, V. Nevolin and A. Zwnkwvich, *Mat. Res. Soc. Symp. Proc.* 402 (1996) 319.
27 J. Kudrenorsky, N. E. Christensen, and O.K. Andersen, *Phys. Rev. B*, No.7, (1993) 5924.
28. H. Bakker, *Diffusion Crystalline Solides*, (1984) 213.
29. A. Himsel, W. Blau, G. Merz, W. Niederlag, V. Querin, J. Weisbach and K. Kleinstuck, *Phys. Stat. Sol., (b)* 100 (1980) 179.
30. D. T. Hawkins, ASM Metals Reference Book, Second Edition, (1983) 104.
31. W. Blau, S. Mager and E. Wieser, *Phys. Stat. Sol. (b),* 81 (1977) 535.
32. U. Birkdz and J. Schelm, *Phys. Stat. Sol. (b),* 27 (1968) 413.
33. M.C. Bost and J. E. Mahan, *J. Appl. Phys.*, 64 (1988) 2034.
34. C. Dimitriadis, J. H. Werner, S. Logothetidis, M. Stutzman, J. Weber and R. Nesper, *J. Appl. Phys.*, 68 (1990) 1726.
35. M. Powalla and K. Hertz, *Appl. Surf. Sci.*, 70-71 (1993) 593.
36. D. J. Oostra, C.W. Bulle-Lieuwma, D. E. W. Vandenhoudt, F. Felten. *J. Appl. Phys.*, 74 (1993) 4347.
37. T. D. Hunt, B.J. Sealy, K.J. Reeson, R. M. Gwilliam, K. R. Homewood, R. J. Sealy and G.R. Booker, *Nucl. Intrum. Meth., B.* 74 (1993) 60.
38. T. D. Hunt, K. J. Reeson, K. P. Homewood, S. W. Teon, R. M. Gwilliam and B.J. Seedy, *Nucl. Instrum. Meth. B*, 84 (1994) 168.
39. M. Pauli, M. Dücker, M. Düscher and J. Müler, *Mater. Sci Eng. B, Solid State Mater. Adv. Technol.*, 21 (1993) 270.
40. C. Giannini, S. Lagomarsino, F. Scarnici and P. Castrucci, *Phys. Rew. B*, 45 (1992) 8822.
41. N. Onda, J. Henz, E. Müller, H.Von Känel, C. Schwarz and R. E. Pixley, *Helv. Phys. Acta*, 64 (1991) 197.
42. N. Onda, J. Henz, E. Müler, K. A. Müder and H. Von Känel, *Appl. Surf. Sci.* 56-58 (1992) 421.
43. J. Chevrier, P. Stocher, L. Thanhvin, J. M. Gay and J. Derrien, *Europhys. Lett.*, 22(6), (1993) 449.

44. U. Kafader, C. Pirri, P. Wetzed and G. Gewinner, *Appl. Surf. Sci*. 64 (1993) 297.

45. W. Külker, R. Wagner, E., Nembach, *J. Phys. F: Met. Phy*. 18 (1988) 2513.

46. K. Hilfrich, W. Kälker, W. Petry, O. Schärpf, E. Nembach, *Scripta Metal. Mater*. 24 (1990) 39.

47. A. R. Bächner, Arch. Risenhüttenwes, 53 (1982) 189.

48. F. Lihl, E. Ebel, Arch. Risenbüttenwes. 32 (1961) 489.

49. K. Hilfrich, W. Külker, W. Petry, O. Schäepf and E. Nembach, *Z. Metallkde*, 84 (1993) 4.

50. M. B. Streams, *Phys. Rev*. 129 (1963) 1136.

51. M. B. Streams, *Phys. Rev*. 147 (1966) 439.

52. G. Inden and W. Pitsch, *Z. Metallkde*, 62 (1971) 627.

53. P. S. Rudman, *Acta. Met*. 8 (1960) 321.

54. R. Beeker, *Z. Metallkde*, 29 (1937).

55. G. Schiatte, G. Inden and W. Pitsch, *Z. Metallkde*, 65 (1974) 94.

56. V. V. Geichenkd, V. M. Danilenko and A. A. Smirnov, *Fiz. Met. Metalloved*, 13 (1962) 321.

57. V. V. Geichenko, V. M. Danilenlo and A. A. Smirnov, *Ukr. fiz. Zhum*. 8 (1963) 323.

58. V.V. Danilenko, D. R. Rizdvyanetskiy and A. A. Smirnov, *Fiz. Metal. Metalloved*, 16 (1963) 1.

59. T. Eguchi, C. Kinoshita, S. Kiyota and K. Yasutake, *Jap. Journ. Appl. Phys*. 5 (1966) 645.

60. V. A. Niculeescu, T. J. Burch, J. I. Budnick, *Journal of Magnetism and Magnetic Materials*, 39 (1983) 223

61. EJD. Garba and R. L. Jacobs, *J. Phys. F: Met. Phys.*, 16 (1986) 1485

62. A. Poletti and L. Passani, *Nuovo Cimento*, 32 (1964) 1449.

63. J. Moss and P.J. Brown, *J. Phys. F2,* (1972) 358.

64. W. A. Hines, A. H. Menotti, J. I. Budnick, T. J. Burch, T. Litrenta, V. Niculescu and K. Raj, *Phys.Rev. B,* 13 (1976) 4060.

65. T. J. Burch, T. Litrenta and J. I Budnick, *Phys. Rev. Lett.*, 33 (1974) 421.

66. S. Pickart, T. Litrenta, T. J. Burch and J. I. Budnick, *Phys. Lett.*, A53 (1975) 321.

67. C. Blaauw, G. R. Mackay and W. Leiper, *Solid State Commum.*, 18 (1975) 729.

68. J. I. Budnick, Zhengauan Tan and D. M. Pease, *Phys. B,* 158 (1989) 31.

69. H. Wever and G. Frohberg, *Z. Metallkde*, 65 (1974) 747

70. H. Bakker and J. P. A. Westerveld, *Phys. Stat. Sol. (b)*, 145 (1988) 405.

71. B. Sepiol and G. Vogl. *Phys. Rev. Lett.*, Vol. 71, 5 (1993) 731

72. E. Firzer, *Z. Metallkde*, 44 (1953) 462.

73. H. Bakker, *Diffusion in Solid and Alloys*, (1990) 265.

74. B. Million, *Czech. J. Phys. B*, 27 (1977) 928.

75. J. Derrien and F. Arnaud d' Avitaya, *J. Vac. Sci. Technol.*, A5 (1987) 2111.

76. N. Cherief, R. Cinti, M. De Crescenzi, J. Derrien, T.A. Nguyen Tan and J.Y. Veuillen, *Appl. Surf. Sci.* 42/21 (1989) 241.

77. J. Derrienn, J. Chevrier, V.Le. Thanh and J.E. Mahan, *Appl. Surf. Sci.*, 56-58 (11992) 382.

78. H. Von Känel, J. Henz, M. Ospelt, J. Hugi, E. Müller, N. Onda and A. Grulle, *Thin Solid Films*, 184 (1990) 295.

79. H. Von Känel, R. Stalder, H. Sirringhaus, N. Onda and J. Henz, *Appl. Surf. Sci.*, 53 (1991) 196.

80. R. Baptist, A. Pelissier and G. Chanvet, *Solid state Commun.*, 68 (1988) 555.

81. F. Arnud d'Avitaya, P.A. Badoz, M. Campidelli, J. A. Campidelli, J.A. Chrobocrek, J.Y. Duboz, A. Perio and J. Pierre, *Thin Solid Films*, 184 (1990) 283.

82. L. Pahun, Y. Campidelli, F. Arnaud d'Avitage and P.A. Badoz, *Appl. Phys. Lett.*, 60 (1992) 1166.

83. H. Lange, *Mat. Res. Soc. Symp. Proc.* 402 (1996) 307.

84. M.C. Bost and J.E. Maham, *J. Appl. Phys.*, 63 (1988) 839.

85. H. Lange, M. Giehler, W. Henrion, F. Fenske, I. Sieber and G. Oertel, *Phys. Stat. Sol. (b)*, 63 (1993) 171.

86. H. Lang, W. Henrion, F. Fenske, Th. Zettler, J. Schumann, and St. Teichert, *Phys. Stat. Sol.* 1 (1996) 195.

87. K. Radermacher, R. Carius and S. Mantal, *Nuclea. Instrum. Methods*, B 84 (1994) 163.

88. H. Lange, W. Henrion, B. Selle, G-U. Reinsperger, G. Oertel and H. Von Känel, *Appl. Surf. Sci.*, in the press.

89. Z. Yang. K.P. Homewood, M.S. Finney, M.A. Harry and K.J. Reeson, *J. Appl. Phys.*, 78 (1995) 1958.

90. L. Wang, L.Qin, Y. Zheng, W. Shen, X. Chen, X. Lin, C. Lin and S. Zou, *Appl. Phys. Lett.*,65 (1994) 3105.

91. C. B. Vining, in *proceeding of the 9th International Conference on Thermoelectrics*, (1991) 249.

92. R.G. Logan, M.C. Bost and J.E. Mahan, *Thin Solid Films*,162 (1988) 29.

93 L. Schellenberg and H.F. Braun, *J. Less-common Metals*, 144 (1988) 341.

94. H. Lange, W. Henrion, E. Jahne, M. Giehler and J. Schuman, *Mat. Res. Soc. Symp. Proc.*, 320 (1994) 479.

95. L.F. Mattheriss, *Phys Rev.*, *B* 43 (1991) 12549.

96. M.P.C.M. Krijn and R. Eppenga, *Phys. Rev.*, *B*. 44 (1991) 9042.

97. S.V. Halilov and E. T. Kulatov, *Semicond. Sci. Technol.*, 7 (1992) 368.

98. A. B. Filonov, I. Tralle, N. N. Dorozhkin, D.B. Migas, V. L. Shaposhnikov, G. V. Petrov, V.M. Anishechil and V. Boresenko, *Phys. Stat. Sol.*, *(b)* 186 (1994) 209.

99. S. Eisebitt, J.E. Rubensson, M. Nicodemus, T. Boske, S. Blugel, W. Eberhardt, K. Radermacher, S. Mantl and G. Bihlmayer, *Phys. Rev.*, *B* 50 (1994) 18330.

100. U. Birkholz and J. Schelm, *Phys. Status Solidi*, 27 (1968) 413; 34 (1969) k,77.

101. C.A. Dimitriadis, J.H. Werner, S. Logothetidis, M. Stutzmann, J. Weber and R. Nesper, *J. Appl. Phys.*, 68 (4) (1990) 1726.

102. K. Lefki, P. Muret, N. Cherif and R.C. Cinti, *J. Appl. Phys.*, 69 (1) (1991) 252.

103. M. Ozvold, V. Bohác, V. Gasparik, G. Leggíeris. S. Luby, A. Luches, E. Majková, P. Mrafko, *Thin Soild Films*, 263 (1995) 92.

104. D. H. Tassis, G.L. Mitass, T. T. Zorba, C. A. Dimitriadis, O. Valassiades, D.I. Siapkas, M. Argelakeris, P.Poulopoulos and N.K. Flevaris, *J. Appl. Phys.*, 80 (2) (1996) 962.

105. Z. Yang, K.P. Homewood, M. S. Finney, M. A. Harry and K. J. Reeson, *J. Appl. Phys.*, 78 (1995) 1958.

106. C. H. Olk, S. M. Yalisove and G. L. Doll, *Phys. Rev. B* 52 (1995)1692.

107. M. Libezny, J. Poortmans, T. Vermeulen, J. Nijis, P. H. Amesz, K. Herz, M. Powalla, G-U. Reinsperger, M. Schmidt, V. Hoffmann, and H. Lang, in *Proceedings 13th Eutopean Photovoltaic Solar Energy Conference*, 1995.

108. C. B. Vining, in *Space Nuclear Power Systems*, *AIP Conf. Pro.*, 246 (1992) 338.

109. J.C. Bean and J.M. Poate, *Appl. Phys. Lett.*, 37 (1980) 643.

110. K. Kim, G. Bai, M. Nicolet, J. Mahan and K. Geib, *Appl. Phys. Lett.*, 58 (1991) 1884.

111. D. J. Ostra, D.E.W. Vanderhoudt, C.W.T. Bullelieuwma and E.R. Naburgh, *Appl. Phys. Lett.*, 59 (1991) 1737.

112. K. Radermacher, S. Mantl, Ch. Dieker and H. Lüth, *Appl. Phys. Lett.*, 59 (1991) 2145.

113. T. D. Hunt, K. J. Reason, R. M. Gwilliam, K.P. Homewood, R. J. Wilson, R. S. Spraggs, B.J. Sealy, C.D. Meekison, G.R. Booker and P. Oberchachtsick, *Mat. Res. Soc. Conf. Pro.*, (1993).

114. Baoqi Li, Mingron Ji and Jianxin Wu, *J. Appl. Phys.*, 68 (3) (1990) 1099.99 H. Moritz, B. Rösen and S. Popvic, A. Rizzi and H. Lüth, *J. Vac. Sci. Technol.*, B10 (4) (1992) 1704.
115. C. A. Dimitriadis and J.H. Werner, *J. Appl. Phys.*,68 (1990) 93.
116. J. Derrien, J. Chevirier, V. Le Thanh, T.E. Crumbaker, J.Y. Natoli and I. Berbezier, *Appl. Surf. Sci.* 70/71 (1993) 546.
117. S. Kennou, N. Cherief, R. Cinti and T. A. Ngugen Tan, *Surf. Sci.* 211/212 (1989) 685.
118. N. Cherief, C.D' Anterroches, R. Cinti, T. A. Nguyen Tan and J. Derrien, *Appl. Phys. Lett.*, 55 (1989) 167.
119. J. Cherrier, V. Le Thanh, S. Nitsche and J. Derrien, *Appl. Surf. Sci.*, 56-58 (1992) 438.
120. V. Le Thanh, J. Chevirier and J. Derrien, *Phys. Rev. B* 46 (1992) 15946.
121. N. E. Christensen, *Phys. Rev. B* 42 (1990) 7148.
122. A. L. Vasquez de Parge, J. de la Figueiro, C. Ocal and R. Mirarda, *Europhys. Lett.*, 18 (1992) 595.
123. N. R. Baldwin, D.G. Ivey, *J. Mat. Sci.*, 31 (1996) 31.
124. H. S. Lee and G.J. Wolga, *J. Electronchem. Soc.*, 137 (1990) 2618.
125. M. Heintze, A. Catana, P. E. Schmid, F. Levy, P. Stadelmann and P. Weiss. *J. Phys. D: Appl. Phys.*, 23 (1990) 1076.
126. D. M. Scott and S. S. Lau, *Thin Solid Films,* 104 (1986) 227.
127. C.D. Lien, L. S. Wielunski, M. A. Nieolet and K. M. Stika, *Thin Solid Films,* 104 1983) 235.
128. C. Chemelli, D. D'Angelo, G. Girardi and S. Pizzini, *Appl. Surf. Sci.*, 68 (1993) 173.
129. H. C. Swart, G.L.P. Berning, *Appl. Surf. Sci.*, 78 (1994) 77.
130. P. Gas and F. D'Heurle, *Mat. Res. Symp. Proc.*, 402 (1996) 39.
131. K.N. Tu, G. Ottaviani, U. Gösele and H. Föu, *J. Appl. Phys.*, 54 (1983) 758.
132. K. N. Tu, *Advances in Electronic Materials*, (1984) 147.
133. U. Gösele and K. N. Tu, *J. Appl. Phys.*, 36 (1976) 3770.
134. J. Gulpen, *Thesis-Eindhoven Unicersity of Technology* (1995).
135. T. Barge, S. Poize, J. Bernardini and P. Gas, *Appl. Surf. Sci.* 53 (1991) 180.
136. C. H. Jan, C.P. Chen and Y,A. Chen, *J. Appl. Phys.* 73 (1993) 1168.
137. T. Bargfe, P. Gas and F. M. D'heurle, *J. Mater. Res.* 10 (1995) 1134.
138. L. Zhang and D.G. Ivey, *J. Appl. Phys.*, 71 (1992) 4314.
139. L. Zhang and D. G. Ivey, *Mas. Res. Soc. Symp. Pro.*, 260 (1992) 257.

140. L. Zhang and D. G. Ivey, *Mas. Res. Soc. Symp. Pro.*, 311 (1992) 299.

141. L. Zhang and D. G. Ivey, *Thin Solid Films*, 245 (1994) 234.

142. N. R.Baldwin, *M.Sc thesis of University of Alberta*. 1995.

143. K. Raviprasad and K.Chattopadhyay, *Acta. Metal. Mater*. No.2, 41(1993) 609.

144. N. R.Baldwin and D.G.Ivey, *J. of Phase Equilibria*. No.4 16 (1995) 300.

145. K. Szymañski, L.Dobrzyñoki and R.Burzyñska, *Hyperfine Interaction*, 59 (1990) 477.

146. K. Szymañski, S. Lefebvre and M. Bessiere, *Materials Science Forum*, 166-169 (1994) 433.

147. R. Kikuchi and H. Sato, *Phys. Rev. B*, 28 (1983) 648.

148. D. Snell and D. G. Ivey, *J. Mater. Sci. Mater. in Electr.*, 40 (1993) 47.

149. D. G. Ivey, R Bruce and G.R. Piercy, *J. Electron. Mat.*, 17 (1988) 373.

150. D. G. Ivey and G. R.Piercy, *J. Elect. Microsc. Tech.*, 8 (1988) 233.

151. P. Jian, *M.Sc. Thesis, University of Alberta*, (1993).

152. L. Zhang and D. G. Ivey, *J. Mater. Res.*, Vol.6 7 (1991) 1518.

153. L. Zhang., *Ph.D. Thesis, University of Alberta*, (1993).

154. B. J. Lee, S.K. Lee and D.N. Lee, *CALPHAD*, vol. 11 2 (1987) 253.

155. F. M. d'Heurle, *J. Vac. Sci. Technol.* A7 (1989)1467.